



Heavy Molecular and Metallic Ions in the Magnetosphere

M. Yamauchi · S. Christon · I. Dandouras · S. Haaland · D. Kastinen · L.M. Kistler et al.
[full author details at the end of the article]

Received: 22 March 2024 / Accepted: 4 October 2024
© The Author(s) 2024

Abstract

Observations and present knowledge of heavy ions with mass ≥ 27 in the magnetosphere are reviewed. There are four ultimate sources of these heavy ions: the solar wind (mainly high charge-state atomic ions), the ionosphere (mainly molecular ions), the atmospheric metal layers that originate ultimately from ablation of meteoroids and possibly space debris (low charge-state metallic ions and metal-rich molecular ions), and lunar surface and exosphere (low charge-state metallic and molecular ions). The upstream heavy ions (solar wind origin and lunar origin) give independent information on the ion entry routes to the magnetosphere from proton (H^+) and alpha particles (He^{++}): with similar mass-per-charge (m/q) values, or gyroradius, for the solar wind origin, and much larger gyroradius for the lunar origin. The lunar origin ions also give independent insights from laboratory observations on the sputtering processes. The atmospheric origin molecular and metallic ions are essential in understanding energization, ionization altitudes, and upward transport in the ionosphere during various ionospheric and magnetospheric conditions. These ions are also important when considering the evolution of the Earth's atmosphere on the geological timescale. Only a few terrestrial missions have been equipped with instrumentation dedicated to separate these molecular and metallic ions, within only a limited energy range (cold ions of < 50 eV and energetic ions of ~ 100 keV or more) and a limited mass range (mainly ≤ 40 amu). This is far too limited to make any quantitative discussion on the very heavy ions in the magnetosphere. For example, the existing data are far from sufficient for determining the dominant contributor from the four possible sources, or even to rule out any of the possible sources as a substantial contributor. Under this circumstance, it is worth to re-examine, using available tools, the existing data from the past and on-going missions, including those not designed for the required mass separation, to search for these ions. The purpose of this review is to summarize the availability of these datasets and tools. This review also shows some examples of combinations of different datasets that provide important indications of the sources of these heavy ions and their amounts that have been overlooked to date. Finally, we note the possible future contamination of specific masses (mainly aluminum (Al), but also lithium (Li), iron (Fe), nickel (Ni), copper (Cu), titanium (Ti) and germanium (Ge)) by the ablation of re-entering human-made objects in space (debris and alive satellites) in the coming decades. This possibility argues the need for dedicated observations of magnetospheric and ionospheric metallic ions before these metallic ions of space debris origin start to dominate over the natural contribution. The required observations can be performed with the available designs of space instrumentation and available ground-based instruments.

Abbreviations

au	astronomical unit
CIR	co-rotating interaction region
CME	coronal mass ejection
ESA	electrostatic analyzer
ESA	European Space Agency
FOV	field of view
GSE	geocentric solar ecliptic coordinate system
IMF	interplanetary magnetic field
IS radar	incoherent scatter radar
LEO	low-Earth orbit
lidar	light detection and ranging (now is accepted as normal noun, though)
Mlat	magnetic latitude
MLT	magnetic local time
MCP	microchannelplate
PHA	pulse height analysis
QL	quick look plot
RPA	retarding potential analyser
SSD	solid-state detector
TOF	time of flight

Space missions and instruments

on board ACE	Advanced Composition Explorer
/ULEIS	Ultra-Low-Energy Isotope Spectrometer
/SWICS	Solar Wind Ion Composition Spectrometer
AE-C and AE-D	Atmosphere Explorer C and D
Akebono/SMS	Suprathermal ion Mass Spectrometer on board Akebono
AMPTE	Active Magnetospheric Particle Tracer Explorers
AMPTE/CHEM	Charge-Energy-Mass Spectrometer on board AMPTE Charge Composition Explorer (AMPTE-CCE)
AMPTE/SULEICA	SUprathermaL Energy Ionic Charge Analyzer on board AMPTE Ion Release Module (AMPTE-IRM)
on board Arase	
/MEPI	Medium Energy Particle experiments Ion mass analyzer
/LEPI	Ledium Energy Particle experiments Ion mass analyzer
ARGOS/ISAAC	Ionospheric Spectroscopy and Atmospheric Chemistry instrument on board the United States Air Force's Advanced Research and Global Observing Satellite
ARTEMIS	Acceleration, Reconnection, Turbulence and Electrodynamics of the Moon's Interaction with the Sun
Cassini/MIMI-CHEMS	Charge-Energy-Mass Spectrometer of Magnetosphere IMAGING Instrument on board Cassini
Chandrayaan-1/SARA	Sub-keV Atom Reflecting Analyser on board Chandrayaan-1
Chang'e-4/ASAN	Advanced Small Analyzer for Neutrals on board Chang'e-4
on board Cluster	
/CODIF	COMposition DIstribution Function of Cluster Ion Spectrometry (CIS)

/RAPID	Research with Adaptive Particle Imaging Detectors
CRRES	Combined Release and Radiation Effects Satellite
on board DE-1	Dynamics Explorer 1
/RIMS	Retarding Ion Mass Spectrometer
/EICS	Energetic Ion Composition Spectrometer
on board Envisat	
/GOMOS	Global Ozone Measurement by Occultation of Stars
/SCIAMACHY	SCanning Imaging Absorption spectroMeter for Atmospheric Cartography
e-POP/IRM	Imaging and Rapid-scanning ion Mass spectrometer on board Enhanced Polar Outflow Probe
on board Geotail	
/STICS	Supra-Thermal Ion Composition Spectrometer
/LEP	Low Energy Particle experiment
ISEE-3	International Sun-Earth Explorer 3
ISIS	International Satellites for Ionospheric Studies
on board JUICE	Jupiter ICy moons Explorer
/PEP/JDC	Jovian Dynamics and Composition of Particle Environment Package on board (PEP)
/PEP/NIM	Neutral gas and Ion Mass spectrometer of PEP
on board LADEE	The Lunar Atmosphere and Dust Environment Explorer
/NMS	Neutral Mass Spectrometer
/LDEX	Lunar Dust EXperiment
/UVS	Ultraviolet-Visible Spectrometer
on board Kaguya	(pre-launch name: SElenological and ENgineering Explorer (SELENE))
/IMA	Ion Mass Analyzer of MAgnetic field and Plasma experiment - Plasma energy Angle and Composition Experiment (MAP-PACE)
MAVEN/STATIC	SupraThermal And Thermal Ion Composition on board Mars Atmosphere and Volatile Evolution mission
on board Mio	(pre-launch name: BepiColombo Mercury Magnetospheric Orbiter (MMO))
/MSA	Mass Spectrum Analyser of Mercury Plasma Particle Experiment (MPPE)
MMS/HPCA	Hot Plasma Composition Analyzer on board Magnetospheric MultiScale mission
Odin/OSIRIS	Optical Spectrograph and Infra-Red Imager System spectrometer on board Odin
OGO	Orbiting Geophysical Observatory satellite
on board Polar	
/TIMAS	Toroidal Imaging Mass-Angle Spectrograph
/TIDE	Thermal Ion Dynamics Experiment
STEREO/PLASTIC	Plasma and Suprathermal Ion Composition on board Solar Terrestrial Relations Observatory
SOHO/CELIAS	Charge, Element, and Isotope Analysis System on board SOLAR and Heliospheric Observatory
VAP	Van Allen Probes
Wind/STICS	Supra-Thermal Ion Composition Spectrometer on board Wind

Models

CABMOD	Chemical Ablation Model
LEGEND	LEO-to-GEO Environment Debris model
MASTER	Meteoroid and Space Debris Terrestrial Environment.
ORSAT	Object Reentry Survival Analysis Tool
SAMI	Southern Appalachian Mountains Initiative
SCARAB	SpaceCraft Atmospheric Re-entry and Aerothermal Break-up
WACCM	Whole Atmosphere Community Climate Model
WACCM-X	WACCM with thermosphere and ionosphere eXtension

1 Introduction

Heavy ions have been found in the magnetosphere since the early 1970s (Shelley et al. 1972; Hoffman et al. 1974). Subsequently, magnetospheric ion dynamics has been studied with four major components (H^+ , He^{++} , He^+ , and O^+). Both helium and oxygen have been used as markers for plasma coming from the solar wind (He^{++}), plasmasphere (He^+), and ionosphere (O^+), respectively, while we cannot distinguish the origin of H^+ . The minor components thus give important information regarding the source and transport.

This also applies to less-abundant minor ions such as molecular ions and metallic ions. The molecular N_2^+ , NO^+ , or O_2^+ ions, compared to the atomic O^+ ions (without separating from N^+), carry certain important information on the internal processes in the ionosphere as well as the ion outflow processes above the ionosphere. The metallic ions give information on the deposition of metals through the ablation of cosmic dust in the upper mesosphere or lower thermosphere, mesosphere-thermosphere coupling, transport process in the ionosphere, as well as on the lunar-origin ions and their entry routes to the magnetosphere.

Such information is not obtained from the four major ion species (H^+ , He^{++} , He^+ , and O^+). For example, the lunar origin ions of four major species are completely masked by those of solar wind origin. Similarly, H^+ , He^+ , and O^+ originating from the lower part of the ionosphere and mesosphere are masked by those that originated in the upper ionosphere. Thus, the heavy molecular and metallic ions provide unique information that is not obtained from the four major ion species, and contributes to understanding many aspects of the geospace environment: the ion escape process from the ionosphere, related ionospheric and even mesospheric processes, deposition of near-Earth small bodies at different altitudes, solar wind-magnetosphere interaction, and even the dynamics of the Moon-origin ions.

The molecular and metallic ions were already detected a long time ago by the ISIS-2 and DE-1 satellites (Hoffman et al. 1974; Chappell et al. 1982; Craven et al. 1985). Despite this, the roles of such heavy ions (mass ≥ 27) and their composition in the terrestrial magnetosphere have received little attention, and the observations of heavy ions and molecular ions in the magnetosphere are sparse. The limited numbers of existing magnetospheric observations are often the byproducts from missions with other prime objectives.

1.1 Four Possible Sources

For heavy molecular ions, the majority is of ionospheric origin mostly coming from the polar ionosphere (e.g., see review by Lin and Ilie 2022), but there may be contributions from other sources and via other routes. For the metallic ions with energies greater than 100 keV/q (energy range of Supra-Thermal Ion Composition Spectrometer (STICS) instruments on board the Geotail and Wind spacecraft), the majority are high charge-state solar wind ions

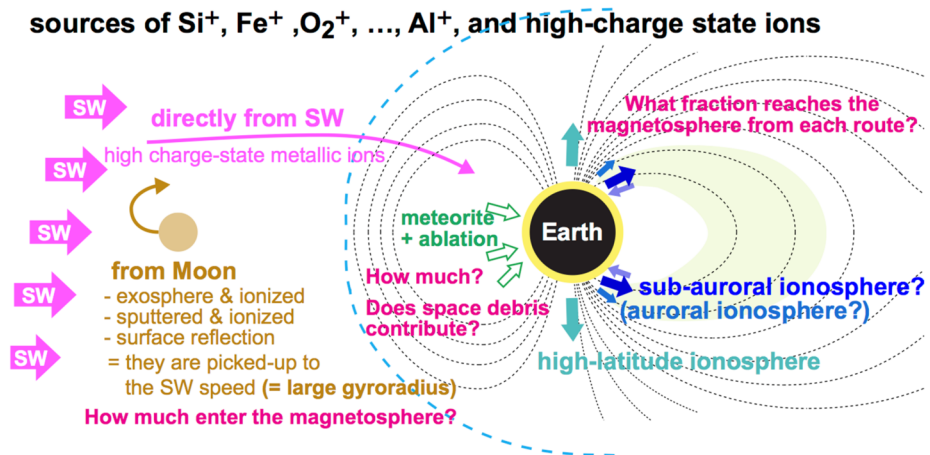


Fig. 1 Illustration of possible sources of heavy molecular ions and metallic/silicate ions (simply “metallic ions” hereafter) in the magnetosphere. The solid arrows show possible pathways of these ions: (1) solar wind for high charge-state metallic ions, (2a) dayside polar ionosphere (cusp and its vicinity) for low charge-state heavy ions (both metallic and molecular ions), (2b) night-to-morning auroral and sub-auroral ionosphere for molecular ions, (3) mesospheric layers of heavy elements, which are ultimately provided by meteoric ablation, for metallic ions, and (4) the Moon surface and exosphere for low charge-state heavy ions. Note that the outflow mechanism from the mesospheric layer means the atoms or ions must receive the same electromagnetic energization mechanisms as ionospheric ions

such as Fe^{12+} , while some ions are low charge-state such as Fe^+ and K^+ (e.g., Christon et al. 2017). Unlike molecular ions, low charge-state metallic ions with similar mass are nearly absent in the upper ionosphere, and hence their upward flux leaving the ionosphere should be extremely low. In addition, the high mass-per-charge (m/q) ratios of these ions require large energies for them to reach the magnetosphere against the escape energy, compared to that for the atomic O^+ . Therefore, the supply of metallic ions from the ionosphere to the magnetosphere is expected to be very small. This makes it difficult to understand how these low charge-state metallic ions are provided to the magnetosphere and where they come from.

As illustrated in Fig. 1, there are four major sources of heavy ions in the Earth’s magnetosphere with mass > 27 amu (here, we limit our discussions to mass < 100 amu, i.e., molecules, metallic atoms and their ionized forms). These sources are: (1) The solar wind; (2) The ionosphere (and thermosphere); (3) The mesospheric layer of heavy elements (hereafter, “metal layers”) for which the metallic species have been detected by sounding rockets and lidar (for Ca^+) since 1970; and (4) The surface and exosphere of the Moon. Here, the upper atmospheric sources are further divided into: (2a) the dayside polar ionosphere (cusp and its vicinity) low charge-state heavy ions, and (2b) night-to-morning auroral and sub-auroral ionosphere molecular ions. Unlike the molecular ions (N_2^+ , NO^+ and O_2^+) that can be produced in the upper part of the ionosphere, metallic ions come from (3) mesospheric metal layers because of the low concentration of metallic atoms in the atmosphere otherwise.

The mesospheric metal layers are produced by the ablation of cosmic dust particles (meteoroids), but a possible contribution from the ablation of space debris may increase in the near future because of the rapid increase of spent rocket motors and defunct satellites. The ablation of these human-made objects during their atmospheric re-entry from space (in this paper termed as “ablation of space debris/waste”) results in the deposition of human-made metallic atoms to the mesosphere. Some common metals in spacecraft such as aluminum

(Al) and lithium (Li) are very rare in the natural meteoroids, and may substantially contribute to the metallic layers (e.g., Murphy et al. 2023), which in the end contribute to the magnetospheric metallic ions.

While the high charge-state ions and the majority of the molecular ions come from (1) the solar wind and (2) the high-latitude ionosphere, respectively, the sources of the low charge-state metallic ions (including Si^+ ; we simply refer to them as “metallic ions” hereafter) have not been identified. Two theoretically possible candidates for the ultimate sources are (3) the mesospheric metal layer (through the high-latitude ionosphere) and (4) the Moon. However, the expected magnetospheric fluxes for these sources are very low, such that even the upstream solar wind cannot be dismissed as a source compared to (1)-(4). So far, not a single satellite observation has confirmed (or even indicated) any of these sources or the conditions required for their entry into the magnetosphere.

Here, we cannot dismiss the Moon as a source of metallic and molecular ions (Hilchenbach et al. 1993; Mall et al. 1998), as the result of sputtering at the surface (Saito et al. 2010) or photoionization in the thin exosphere (Halekas et al. 2015). When the Moon is upstream of the Earth (near the new Moon), these sputtered and photoionized ions are picked up by the solar wind plasma and gain up to twice the solar wind velocity (tens keV to hundred keV), with sufficiently large gyroradii to penetrate the magnetosphere. The problem is their flux. The initial result from Apollo did not show the upper lunar atmosphere containing metallic species, and only upper limits have been derived from ground-based observations (Stern 1999). Although Kaguya found a signature of metallic ions at 100 km altitude around the Moon by in-situ measurement (Saito et al. 2010), and the Lunar Atmosphere and Dust Environment Explorer (LADEE) confirmed the thin exosphere with heavy species (Poppe et al. 2016b), the Moon-origin ion flux in the Earth’s magnetosphere must be nearly impossible to detect after spreading over the large volume of the magnetosphere.

The very low ion flux also applies to the mesospheric source. Although the upward ion convection below the exobase is common and the escape energy is similar (about 20 eV for mass 30) between the metallic atoms (or ions) and molecules (or molecular ions), we expect the metallic ion flux at the exobase to be much lower than that of the molecular ions. The heavy mass (high escape energy) also makes it difficult for metallic ions to reach the ion energization region above the exobase where ions are accelerated to more than the escape energy. In the best case when any metallic ions are upflowing from the exobase, it must be in the polar region where the magnetic field points nearly vertical and upflowing molecular ions with similar masses are observed (Yau et al. 1993). Note that this energization works for ions but not for neutrals. Since the density ratio of ion to neutral is small at the lower part of the ionosphere, drag of neutrals by the ions is not very effective to gain the escape energy at exobase, and therefore, we hereafter focus on ions but not neutrals.

These possible sources for low charge-state metallic ions may, in the best case, only account for a very low flux in the magnetosphere. On the other hand, because of the low flux that makes it difficult to detect these ions, these ions may work as a good marker of how these ions are transported from the source. Considering the completely different energy and energy/charge from the light ions or high charge-state ions (large gyroradius and high energy), the distribution and amount of these metallic ions give independent information on the entry of ions from the solar wind and from the ionosphere. Thus, these very minor ions work as good tracers.

1.2 Science Related to Each Source

The source mechanisms of metallic or heavy molecular ions (producing them and bringing them into the magnetosphere) are different between the different sources. This opens

Table 1 Possible scientific contributions from heavy ion measurements

Ion source	Relevant science topics
(1) Solar wind (metallic ions)	Solar wind - magnetosphere interaction for different masses (with similar E/q) Ion entry into the magnetosphere
(2) Ionosphere (molecular ions)	Magnetosphere-Ionosphere coupling Energization processes at low altitude Ionospheric chemistry and dynamics for both dayside and nightside Atmospheric evolution (high latitude source only)
(3) Mesosphere and lower thermosphere (metallic ions)	Thermospheric dynamics Expansion of mesosphere and mesosphere-thermosphere-ionosphere coupling Ionospheric dynamics on both dayside and nightside Flux and ablation altitude of meteoroids Ablation and deposition of space debris with lower velocity than meteoroids On-orbit space debris fragmentation
(4) Moon surface and exosphere (low charge-state ions)	Solar wind - surface interaction for different mass (with similar E/q) Micrometeorite-surface interaction Solar wind-magnetosphere interaction for pick-up heavy ions with different masses (with different E/q)

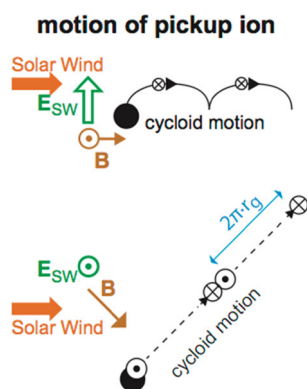
up a possibility of classifying these ions in the magnetosphere in terms of dependency on the source condition (which also depends on the geomagnetic and solar wind conditions). Together with the fact that they are very minor in the magnetosphere, quantitative measurements of these ions in the magnetosphere through each source at various places and various condition help to reveal the source mechanisms of various sources, and thus contribute to many science topics, as summarized in Table 1.

First, metallic (and heavy molecular) ions coming from the ionosphere carry essential information of the particle transport (by electromagnetic and electrostatic fields) in a collision-free frame from the exobase, particle transport in the ionosphere (and even in the mesosphere), ionization and chemistry in the ionosphere, and dynamics of the metal layers in the mesosphere and ionosphere. Here, ablation of the cosmic dust and near-Earth small bodies is considered as the source of the metal layers, and hence metallic ions of mesospheric and thermospheric origin are largely attributed to meteoroids.

In addition, the amount of escaping molecular ions gives extra information on the evolution of the Earth's atmosphere, although the main evolution is caused by the surface interaction including biological activity. Here, the evolution is not limited to the change in the total amount of oxygen, but also includes the oxidation rate (low CO_2/O_2 ratio and low N_2/O_2 ratio compared to Mars and Venus) and its fluctuation (a 5% change in on a 0.1 million years scale happens rather often). The observed O^+ escape ratio suggests that the ion escape might have substantially contributed to the past fluctuation of the oxidation rate (Yamauchi 2019; Dandouras et al. 2018, 2016).

The low charge-state metallic ions in the magnetosphere can also be a possible indicator of space debris because, in the near future, we expect a substantial increase of human-made heavy atoms/ions (e.g., lithium (Li) with mass 7, aluminum (Al) with mass 27, silicon (Si)

Fig. 2 Illustration of cycloid motion and resultant ExB drift direction of the pickup ions in the solar wind under general IMF direction. With an initial velocity nearly zero, ions can reach twice the gyroradius (r_g in the figure) for the solar wind speed (cf. Table 3), traversing a distance of $2\pi \cdot r_g$ in the drift direction. Because of the finite IMF B_X component along the solar wind, the drift direction is generally oblique to the solar wind direction



with mass 28, titanium (Ti) with mass 48, iron (Fe) with mass 56, nickel (Ni) with mass 59, copper (Cu) with mass 64, and germanium (Ge) with mass 73) deposited to the mesosphere during the ablation of space debris/waste as mentioned above (Schulz and Glassmeier 2021). Among them, those relatively rare in the natural meteoroids may become detectable. These amounts, although they are small, might exceed the natural heavy ions in the near future if no new countermeasures against space debris are taken before the Kessler syndrome (Kessler and Cour-Palais 1978) starts over a wide altitude range (which might have already started over a limited altitude around 500–800 km in the worst-case estimate).

Finally, the lunar origin low charge-state metallic ions give information on how the ions with very large gyroradii are picked up and enter the magnetosphere (through the bow shock, magnetosheath, and magnetopause). The entry processes and routes must be quite different from those of the high charge-state metallic ions originating from the solar wind and the solar energetic particles. To investigate them, we need to monitor the lunar origin ions near the Moon, which also allows us to further understand the sputter process on the lunar surface and striving process of the lunar exosphere (e.g., charge exchange and sputtering) by the solar wind (e.g., Saito et al. 2010; Colaprete et al. 2016) for different solar wind conditions including its composition.

These pickup ions of lunar origin may reach any part of the dayside depending on the interplanetary magnetic field (IMF) direction, as illustrated in Fig. 2. The finite gyroradius (r_g), as summarized in Table 3, also contributes the spread of impact area of pickup ions on the magnetosphere. In Table 3, we used enhanced values of the solar wind speed and the IMF strength for estimating the gyroradius, because a high ion flux of lunar origin is expected when the solar wind impact on the Moon is enhanced such as during CMEs and CIRs. Considering the Earth-Moon distance of 60 Earth radius (R_E), the CME condition might make the metallic ions with mass-per-charge (m/q) more than 40 not completing one gyration before reaching the magnetopause.

In this review, we do not consider any loss mechanisms such as charge exchange, pitch-angle scattering or magnetopause shadowing (e.g., Yamauchi 2019). The observed flux, actually observed counts, of metallic ions is too low to discuss anything meaningful (even qualitative) about the loss process. We cannot even distinguish the flow directions of the metallic ions whether they are simply traversing the magnetosphere in their anti-sunward motion (majority of O^+ ions outflowing from dayside and polar cap flow in this way (Slapak et al. 2017a, 2017b) or they are temporarily trapped in the magnetosphere. The observed flux for heavy molecular ions is also low, and any discussion based on the reported observa-

Table 2 Overview of heavy ion observations in the terrestrial magnetosphere

Species	Mass resolution and Energy range	Dedicated instrument or not	Examples (Earth/Moon missions)
C^+ , N^+ , or O^+ ($m/q = 14-16$)	C^+ , N^+ , O^+ as a group (not resolved, all energy range) N^+ and O^+ are separately resolved (<50 eV) C^+ , N^+ , O^+ are resolved (>100 keV)	dedicated ¹ non-dedicated ² non-dedicated	Cluster, VAP, MMS, etc DE-1, Akebono AMPTE, Geotail
N_2^+ , NO^+ , or O_2^+ ($m/q = 28-32$)	N^{++} , NO^+ , O^{++} as a group (<50 eV) Group (10–100 keV) Group (>100 keV) N^{++} , NO^+ , O^{++} are resolved (<50 eV) Group (0.05–30 keV) Resolved (30–100 keV) Resolved (>100 keV)	dedicated dedicated dedicated non-dedicated non-dedicated non-dedicated non-dedicated	e-POP, ISIS-2 Arase CRRES, Polar DE-1, Akebono Cluster, Arase, MMS, etc AMPTE AMPTE, Geotail
High charge-state heavy	Resolved (>100 keV)	dedicated	Geotail, Wind, AMPTE, etc
Low charge-state metallic	Resolved (>100 keV) Resolved (cold) Resolved (0.01–30 keV)	dedicated dedicated@moon dedicated@moon	Geotail, Wind LADEE Kaguya, LADEE

¹Designed for routine separation. ²No routine separation was designed.

Table 3 Gyroradius (in R_E) of different ions exposed to the solar wind with certain velocities (km/s) and magnetic fields (nT)

m/q (*1)	400 km/s	600 km/s	600 km/s	800 km/s	1000 km/s
	3 nT	3 nT	10 nT	10 nT	10 nT
1 (H^+)	0.2 R_E	0.3 R_E	0.10 R_E	0.13 R_E	0.16 R_E
2 (He^{++})	0.4 R_E	0.7 R_E	0.2 R_E	0.3 R_E	0.3 R_E
4 (He^+)	0.9 R_E	1.3 R_E	0.4 R_E	0.5 R_E	0.7 R_E
16 (O^+)	3.5 R_E	5.2 R_E	1.6 R_E	2.1 R_E	2.6 R_E
23 (Na^+)	5.0 R_E	7.5 R_E	2.2 R_E	3.0 R_E	3.7 R_E
39 (K^+)	8.5 R_E	12.7 R_E	3.8 R_E	5.1 R_E	6.4 R_E
56 (Fe^+)	12.1 R_E	18.2 R_E	5.5 R_E	7.3 R_E	9.1 R_E

m/q: mass per charge ratio

tions may be misleading (we cannot discuss beyond what we already know for O^+ ions that enter the magnetotail through the high latitudes).

1.3 Lack of Observations

Unfortunately, these heavy ions and atoms are largely unexplored in near-Earth space, and no terrestrial mission has had a dedicated instrument for the mass range covering up to the metallic ions at energy less than 100 keV, as summarized in Table 2. Past and recent works in detecting these molecular and metallic ions were carried out with non-dedicated instruments, such as plasma instruments designed to separate only four major species H^+ , He^+ , He^{++} , and O^+ . Thus, the current understanding is at a preliminary level, and in the best case, only qualitative (even for the major four possible sources in Fig. 1).

Due to such difficulties in extracting the heavy molecular and metallic ions from the data, past works on these very heavy ions in the magnetosphere are very sparse, spanning many years by different missions. Furthermore, it is difficult to have event studies between different spacecraft, because the observation of metallic ions requires a long integration time (to accumulate adequate counting statistics for these low-abundant species), and active observations of wide mass ranges between different missions do not normally overlap within the same time period. For these reasons, an obvious question remains as to whether any source is dominant over other sources, and if so, under what conditions. At the present, even the relative importance of the ion sources for each species between the lunar origin and terrestrial origin is not known.

Any quantitative (statistically significant) measurements in the future will give important information on the transport of these very heavy ions in the magnetosphere: e.g., on the entry route, acceleration, and dependence on external conditions. On the other hand, during the best conditions such as large geomagnetic storms, some of the existing instruments on-board the past and current spacecraft listed in Table 2 actually separated N^+ , O^+ , N_2^+ , NO^+ in observations, and even metallic ions (Fe^{n+}) after sufficient integration of the data over time. In other words, using existing data from past and on-going missions, we are able to detecting these ions, although the result is largely qualitative. Thus, it is very useful to make a list of all possible instruments that can potentially detect heavy molecular and atomic ions. Of course the limitation is severe. Even tracing the source of the observed metallic ions is often not possible from the available data except for some obvious cases such as near the interaction region with the solar wind.

In the list, we should include the Moon and solar wind missions that actually observed the Earth's magnetosphere, if the mission included a mass spectrometer better suited for these investigations than those onboard magnetospheric missions. One example is the Kaguya Moon mission that was inside the magnetotail or upstream of the magnetosphere for substantial time periods (Saito et al. 2010). Another example is the WIND mission that traversed the magnetotail for many hours. Non-mass resolved ion spectrometers with a wide energy range might also detect heavy ions when ions are picked up and are flowing with the solar wind velocity, such as the observation of Venus downstream at the Sun-Earth Lagrange point (Grünwaldt et al. 1997). Ideally, Earth-flybys of planetary missions should also be included because they normally carry mass spectrometers with much better mass resolution at energies of 0.01–100 keV than those on magnetospheric missions, but it is not very practical to include them because very limited data was taken by only Cassini and STEREO.

Since the molecular and low charge-state metallic ions were not the prime observation objective of all the past and current magnetospheric missions listed in Table 2, software tools and methodology to extract information about these heavy ions are normally not well documented or maintained. Thus, there is a risk of losing the relevant data (including the case that data become unreadable with modern computer systems) even for data that are used as examples of the reported metallic or heavy molecular ions. Therefore, collection of the capable missions and instruments requires information of software availability. This is very difficult, if not impossible, for terminated missions.

It would be also useful to combine different types of observations, e.g., solar wind monitor, Moon data, satellite data in both the magnetosphere and ionosphere, and ground-based (lidar) data. We present several examples that could update the present knowledge about heavy ion entry into the magnetosphere.

Finally, we discuss a possible “ideal” and “compromised” suite of observations, including feasible improvements of the instruments (including software). Such a suite helps planning the future observation by many capable missions (such as onboard the Space Safety/Earth Observation/Lunar Exploration missions) as well as a dedicated mission. Here, we aim to answer fundamental questions that arise for different conditions, such as:

- What is the relative importance of the terrestrial (ionosphere or mesosphere) source and the lunar source for the low charge-state heavy ions in the magnetosphere?
- How much of the observed heavy ions emanate from the aurora/sub-auroral ionosphere compared to the cusp and its vicinity?
- Is it possible to quantitatively evaluate the present and future contamination by space debris?

2 The Scientific Importance of Molecular and Metallic Ions

Figure 3 shows Geotail/STICS statistics of the count distributions over 20 years, ordered by mass (m) and mass-per-charge (m/q) in four different regions (Christon et al. 2017). In the magnetosphere (Fig. 3c: SPHERE), low charge-state metallic ions (Fe^+) are seen as (marked as 1 at the top of the panel) isolated from high charge-state Fe ions, in addition to heavy molecular ions (MI) at around $m/q \sim 30$.

2.1 Importance and Present Knowledge of the Solar Wind Source (High Charge-State Metallic Ions)

The solar wind is the obvious source of high charge-state metallic ions in the terrestrial magnetosphere because the high temperature of the solar corona provides for multiple high

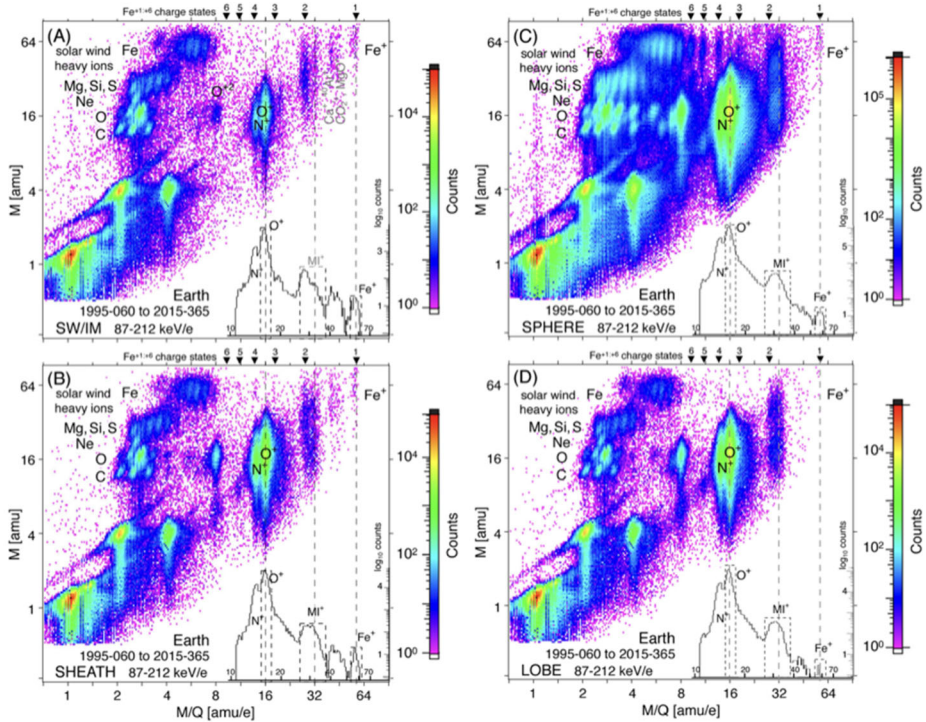


Fig. 3 Average 100–200 keV/e ion composition in and near Earth's Magnetosphere. Mass - mass-per-charge ($m - m/q$) diagrams are shown for 4 different regions (see Christon et al. 2017 for definition): (a) the upstream region (SW/IM), (b) the magnetosheath (SHEATH), (c) the magnetosphere (SPHERE), and (d) lobe, respectively. The counts found in the upper left half of each panel correspond to high charge-state ion of the solar wind origin. At lower right part of each panel, histogram for m/q is also shown for low charge-state heavy ions. Here, m/q is obtained from the combination of electrostatic analysis (giving energy-per-charge E/q) and time-of-flight TOF (giving velocity), and m is obtained from the combination of pulse height analysis PHAs (giving total energy E) and TOF. The measurement accuracy is the best for E/q and the worst for E , resulting in more spread in the m direction than in the m/q direction. Image reproduced with permission from Christon et al. (2017), copyright by AGU.

charge-state ionizations of all elements. During the travel or even at the corona, ions are often energized to more than 1 MeV, forming the solar energetic particles (SEPs), and these ions have sufficiently high energy to be detected by mass spectrometers of energetic particles, as shown in Fig. 3. Note that the term “solar wind” does not necessarily mean that all these elements are flowing with the solar wind proton flow. Some solar flare origin energetic ions take different path such as along the IMF, while some are accelerated at the interplanetary shock to reach the energy detectable by the Geotail/STICS instrument (Fig. 3). Even atoms and of interstellar origin, including galactic cosmic rays, are also present in the solar wind, although in much smaller abundances than those of solar origin.

Figure 3 also shows existence of Fe^+ and Fe^{++} , isolated from high charge-state Fe ions, indicating upstream sources of atomic metals, i.e., other than the solar corona. The obvious candidate is the Moon when it is upstream (to be discussed in Sect. 2.4). These low charge-state metallic ions, which are picked up by the solar wind (i.e., to the similar velocity as the solar wind), have quite different gyroradii from the solar wind protons as summarized in Table 3. Consequently, these metallic ions can be used as the tracers as mentioned in Sect. 1.1.

For example, one can gain a clue about the pathway of these ions to the Earth by knowing the distribution and amount of these metallic ions, and by comparing with those of light ions. Furthermore, the distribution of low charge-state metallic ions provides information about the energization mechanisms across the bow shock and magnetospheric boundaries, and even the entry mechanisms to the magnetosphere because any electrostatic acceleration (e.g., at the bow shock) gives different acceleration efficiency compared to light ions even for the same mass per charge (m/q).

A major challenge is that, compared to good-quality observations and datasets in the solar wind for both the solar wind energy (generally < 100 keV and < 2 keV/ q) and the SEP energy (up to 100 MeV), magnetospheric observations are sparse and are typically limited to high energy for high charge-state ions.

2.1.1 Observations in the Solar Wind

The observations of heavy ions in the solar wind date back to the first space missions, such as the Vela missions (e.g., Hundhausen et al. 1967) and the Apollo Moon missions in the 1960s. The satellites in Vela series were equipped with energy per charge instruments from which composition could be derived. Heavy ions, in the form of high charge-state oxygen, were reported by Bame et al. (1968a, 1968b) using observations from the Vela 3 satellite. Subsequent versions of the Vela satellites carried more advanced instruments, and even heavier ions like silicon (Si) and iron (Fe) and possibly sulfur (S) of various charge states were reported by Bame et al. (1970).

The composition of the solar wind has also been inferred from depositions in the aluminium foils deployed on the Moon surface by astronauts of the Apollo 11–16 missions (Geiss et al. 2004) and from analysis of sample returns for updated information (e.g., Reisenfeld et al. 2007; Jurewicz et al. 2007; Heber et al. 2021)

In the late 1980s and early 1990s, space missions fitted for solar wind observation such as ISEE-3, Ulysses, SOHO, ACE, and WIND, measured the solar wind composition (e.g., Gloeckler et al. 1992; Geiss et al. 1995; von Steiger et al. 2000; von Steiger and Zurbuchen 2002; Reisenfeld et al. 2007). The new generation of instrumentation, particularly particle spectrometers with electrostatic deflectors and time-of-flight analyzers, enabled a more comprehensive mapping of the solar wind composition. For example, SOHO CELIAS/MTOF instrument (Hovestadt et al. 1995) identified and classified elements where no coronal spectroscopic measurements are possible (Wurz 2005).

Figure 4 shows a mass spectrum observed by SOHO/CELIAS with its MTOF sensor. The figure shows the variety of atomic constituents in the solar wind over a wide energy range. Table 4 shows an overview of metallic (atomic number $Z \geq 10$) ion species detected in the solar wind, and their abundance relative to that of oxygen (oxygen itself constitutes about 0.05–0.15% of all ions in the solar wind (e.g., Bame et al. 1975; von Steiger et al. 2010)). The table even includes the solar surface data obtained by optical methods. Because many processes in the solar atmosphere, chromosphere, and corona, and the eventual formation of the solar wind depend on m/q , the composition of the photosphere and the solar wind differ by factors of 2 to 4, depending on slow and fast solar wind conditions.

2.1.2 Observations in the Magnetosphere

Observations of metallic ions in the magnetosphere are very sparse because of their high mass (long TOF and large gyroradius compared to H^+) and extremely low flux. This applies to ions of both the solar wind origin (high charge-state) and the Earth/Moon origin (low

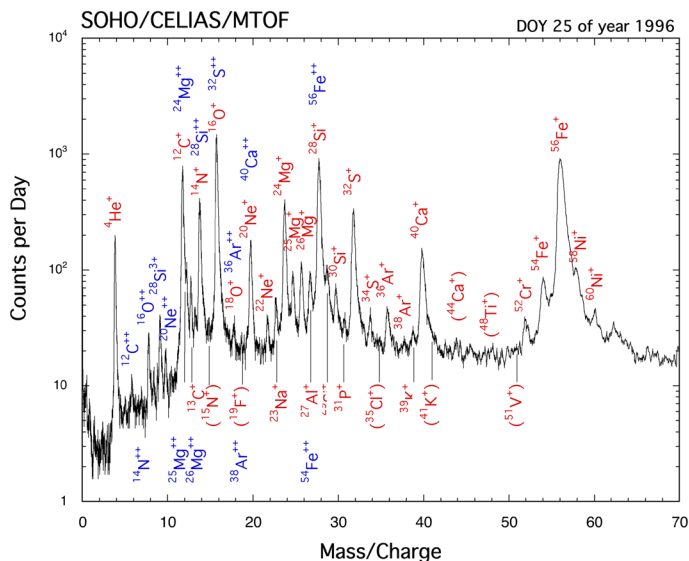


Fig. 4 SOHO CELIAS/MTOF data of mass spectrum of solar wind heavy ions. The charge state given in the labels refers to the charge inside the MTOF instrument (it not referring to the charge state in the solar wind), and so is the horizontal axis “Mass/Charge”. Up to two main ion contributors are indicated at each peak. Labels in parenthesis indicate that the identification of that ion is highly uncertain. Image reproduced with permission from (Wurz 2005), copyright by ESA

charge-state). Except planetary missions, only energetic particle detectors (> 100 keV that give short enough time-of-flight to obtain the velocity) are capable of detecting the metallic ions, such as STICS instruments on board Geotail and Wind. Past ion mass spectrometers for lower energies that were capable of identifying molecular ions (e.g., DE-1/EICS, Akebono/SMS) did not routinely sample the full mass range. Even for instruments on board the ongoing missions (Arase/LEPI, MMS/HPCA) that have the ability of detecting molecular ions of < 20 keV, it is not possible to separate metallic ions from the other heavy ions. One notable exception for the magnetospheric observation was the Kaguya Moon mission that could detect metallic ions, although the detection of the metallic ions was limited to those from the Moon surface, but not from the near-Earth region.

For the solar wind source, its contribution to metallic ions in the magnetosphere varies with the solar activity and with the solar cycle (e.g., Mitchell et al. 1983; Reames 1995; von Steiger et al. 1997; Zurbuchen et al. 2002; Gilbert et al. 2012; Zurbuchen et al. 2016; Wurz 2005), as well as connectivity to the Sun, e.g., slow or fast solar wind (e.g., Feldman et al. 2005). Nevertheless, traces of these heavy ions are almost always present in the magnetosphere.

Using AMPTE/CHEM data, Gloeckler et al. (1985) and Gloeckler and Hamilton (1987) reported that the relative abundances of the solar wind species in the magnetosphere, including high charge-state Fe ions, were very similar to the corresponding solar wind abundances, indicating that the solar wind enters the magnetosphere without significant mass discrimination. Allen et al. (2017) undertook similar analyses by comparing O^+ and O^{6+} in the magnetosphere. The mass – mass per charge ($m - m/q$) diagram shown in Fig. 3c (Christon et al. 1994, 2017) clearly show that high charge-state solar wind ions of Fe, Mg, Si, C, N, and O exist in the magnetosphere. Examining the iron charge states close to geosynchronous

Table 4 Relative abundance compared to Oxygen element

Element	Photosphere (*1)	Meteoritic (*1)	SW: Inter-stream (*2)	SW: Coronal-hole (*2)	SEP-derived Corona (*3)
H	1500	-	1900	820	-
Li	<0.001	<0.001	-	-	-
O	1	(*4)	1	1	1
Na	0.003	0.003	-	-	0.012
Mg	0.056	0.056	0.16	0.083	0.192
Al	0.004	0.005	-	-	0.015
Si	0.052	0.054	0.18	0.054	0.176
P	<0.001	<0.001	-	-	0.001
S	0.032	0.023	-	-	0.043
Cl	<0.001	<0.001	-	-	<0.001
K	<0.001	<0.001	-	-	0.001
Ca	0.003	0.003	-	-	0.014
Ti	<0.001	<0.001	-	-	0.001
Cr	0.001	0.001	-	-	0.003
Mn	<0.001	<0.001	-	-	0.001
Fe	0.047	0.047	0.12 - 0.19	0.057	0.224
Ni	0.003	0.003	-	-	0.008
Cu	<0.001	<0.001	-	-	<0.001
Zn	<0.001	<0.001	-	-	<0.001

(*1) Photospheric and meteoritic abundances are from a compilation by Anders and Grevesse (1989) and Grevesse and Sauval (1998)

(*2) Solar wind abundances (SOHO/CELIAS) are taken from von Steiger (1995)

(*3) SEP-derived coronal abundances (SOHO/CELIAS) are taken from Breneman (1985)

(*4) Assumed as the same as photosphere

orbit measured by CRRES, Grande et al. (1996) showed a dramatic change of the dominant charge state from +9 to +16 during a large magnetic storm, again suggesting that the charge states measured in the outer magnetosphere reflect the changes of the charge state in the solar wind. A comparison of the iron charge states measured by ACE/SWICS in the solar wind and by Polar in the cusp/cleft region (Perry et al. 2000) showed that the solar wind material direct enters during southward IMF time periods. Haaland et al. (2020, 2021) identified Fe using the RAPID instrument on board Cluster (which does not measure charge state), as shown in Fig. 5. They find that the abundance varies with solar activity, again indicating a solar wind source. Thus, the charge state measurements clearly showed that the solar wind is the dominant source of energetic iron in the magnetosphere.

On the other hand, Geotail/STICS observation includes low charge-state metallic ions of $m/q > 35$, such as Fe^+ , as shown in Fig. 3. Possible sources of metals and low charge-state metallic ions are the Earth's upper atmosphere, the Moon, and meteoroids, as illustrated in Fig. 1. This is a completely unexplored field because of the lack of suitable instruments, even considering the very marginal capability for these measurements. Therefore, when considering the magnetospheric heavy ions, we need to know the charge state information even for metallic ions, although almost all signals are of high charge-state of the solar wind origin.

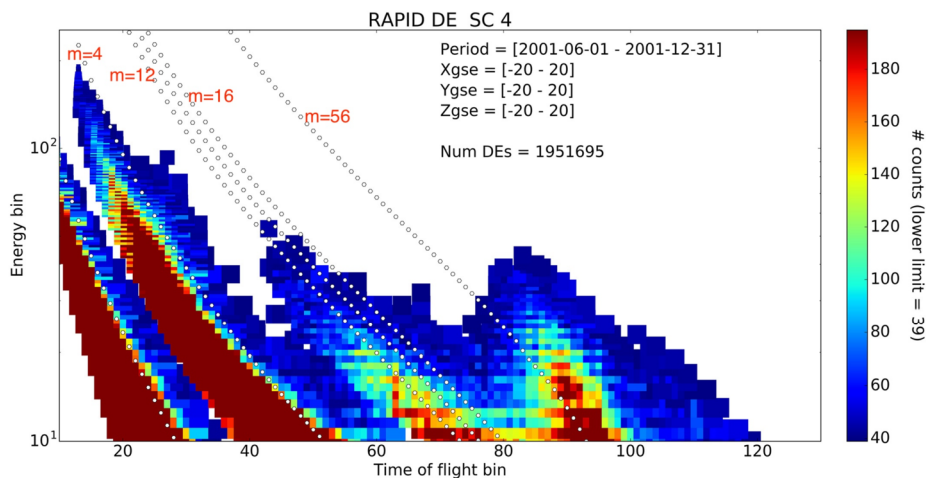


Fig. 5 Composition measurement by Cluster/RAPID over 18 years. The light gray dotted lines indicate theoretical energy versus time-of-flight (TOF) for atomic mass of, from right to left, $m = 56$ (Fe), 16 (O), 14 (N), 12 (C), 4 (He) and 1 (H). Energy for Fe channel (no distinction of charge state) is > 400 keV, which covers higher energies than Fig. 1 for Fe^+ , as well as the same energy range as solar wind $\text{F}^{m \geq +7}$. Image reproduced with permission from Haaland et al. (2020), copyright by the author(s)

2.2 Importance and Present Knowledge of Ionospheric Source (Molecular Ions)

Molecular ions such as N_2^+ , NO^+ , and O_2^+ were found together with O^+ ions in the top-side ionosphere in the 1970s (Hoffman et al. 1974) and at high altitude (above $2 R_E$ altitude) in 1980s (e.g., Chappell et al. 1982; Craven et al. 1985). Unlike the many atomic ion species in the magnetosphere (H, He, N, and O), which are partly supplied from the solar wind, molecular ions cannot be of solar wind origin. In fact, Akebono Suprathermal ion Mass Spectrometer (SMS) found upflowing molecular ions. One peculiar feature is that the fluxes of molecular ions (N_2^+ , NO^+ , and O_2^+) in the magnetosphere, for both the upflowing ions coming from the ionosphere and trapped one in the inner magnetosphere, increase more drastically than atomic ions (O^+) during strong geomagnetic storms (Yau et al. 1993; Craven et al. 1985; Klecker et al. 1986; Hamilton et al. 1988). The correlation between the magnetospheric activity (measured by geomagnetic indices) and the ion flux of ionospheric origin in the outer magnetosphere had been recognized already in the 1970s (Geiss et al. 1978).

The drastic increase of molecular ion flux during strong magnetic storms in the inner magnetosphere ($L = 2-8$) is seen over a wide energy range by the Arase satellite (Seki et al. 2019; Takada et al. 2021), with the MEPI and LEPI instruments, by the velocity filter effect which are capable of quantitatively separating heavy molecular ions (in the mass group of 28–32) from atomic ions (Yokota et al. 2017; Asamura et al. 2018). Therefore, these low-energy O^+ and O_2^+ ions in the outer magnetosphere must be, together with low energy He^+ , considered to originate from the ionosphere (Young et al. 1977; Geiss et al. 1978).

Since geomagnetic storms increase the energy deposition (in both forms of electromagnetic energy flux and particle precipitation) from space to the ionosphere and to the coupled magnetosphere-ionosphere system, such a stormy condition will enhance upward transport in the ionosphere (ionospheric dynamics), ion production in the ionosphere (ionospheric chemistry), and/or pre-energization before reaching the main energization region (particle

dynamics above the ionosphere) in the ionosphere. The actual processes are summarized in Sects. 2.2.1, 2.2.2, 2.2.3, respectively. These effects are more drastic for molecular ions than atomic ions because the threshold input energy required for molecular ions outflowing is higher than that for the atomic ions. In Sect. 2.2.4, we describe the expected consequence in geological time scale: such enhancement of the molecular ion outflow may even influence the evolution of the life more than atomic ions influences.

Although these heavy molecular ions are of ionospheric origin (lunar source is negligibly small, see Sect. 2.4), the source location is not completely understood, partly because of the lower fluxes compared with atomic ions and partly because of the difference in the ionospheric processes between the molecular ions and atomic ions, as described in Sect. 2.2.3. For heavy atomic ions (O^+), there are two major outflow regions: one is the dayside polar region (cusp and its downstream region) and the other is auroral region where auroral acceleration is taking place (Moore et al. 1999b; Peterson et al. 2008). On the other hand, the Akebono satellite at more than $2 R_E$ geocentric distance found intense fluxes of upflowing heavy molecular ion predominantly on the dayside (Yau et al. 1993), while much less flux or zero flux of the molecular ions were detected in the nightside at auroral latitudes in the observation where the O^+ upflow are observed.

Note that this $O^+ - O_2^+$ difference can still be attributed to the orbit and data sampling coverage because we expect an equatorward shift of heavier species with respect to light species in the nightside, where the magnetospheric convection is predominantly equatorward during geomagnetic storm conditions, the condition when the molecular ion upflow from the ionosphere is enhanced. Under any convection, heavier ions with the same energy as the lighter ions are carried further downstream by the magnetospheric convection compared with the lighter ions (this effect is called as velocity filter). Such mass dependence is actually observed by Freja as the difference between the H^+ injection and O^+ injection in the opposite hemisphere (Hultqvist 2002; Yamauchi et al. 2005), with O^+ injections found equatorward of H^+ injections. Thus, we expect that the upflowing molecular ions reach lower latitudes (e.g., the outer radiation belt) than atomic ions during the upflow process, such that they travel beyond the latitude range of SMS operations at Akebono altitude.

The coverage problem is not limited to Akebono observation because the ion instruments on board the magnetospheric satellites are often turned off at the sub-auroral latitudes to avoid the damage from the radiation belts, potentially missing the molecular ions flowing in such low latitudes. Since the energization is expected to be quite different between different latitudes, the outflowing path and/or the pre-energization process may be different between the molecular ions and atomic ions.

It is yet unknown how much and in what condition the ionospheric molecular ions in the nightside auroral or sub-auroral region outflow from the topside ionosphere (or exobase), and what fraction do they populate the magnetosphere. These questions apply even to the dayside high-latitude route. By comparing these results, we can gain more information on the ionospheric processes as well as the energization processes above the ionosphere.

Molecular ions of ionospheric origin can possibly be observed deep in the magnetotail ($> 50 R_E$). Although no mass spectrometer for the magnetotail observation is capable of separating O_2^+ ions from O^+ ions at energy less than 100 keV (Kaguya Moon mission with a capable instrument did not looking at the magnetotail flow), an ion energy spectrometer with large geometric factor may in principle detect it at higher energy than atomic ions (O^+) because we expect the same velocity for all species. However, in reality the energy spread of O^+ is wide and O^+ energy can even be 30 times as the H^+ energy. For example, the Acceleration, Reconnection, Turbulence, and Electrodynamics of the Moon's Interaction with the Sun (ARTEMIS) spacecraft detected a high anti-sunward ion flux at about the

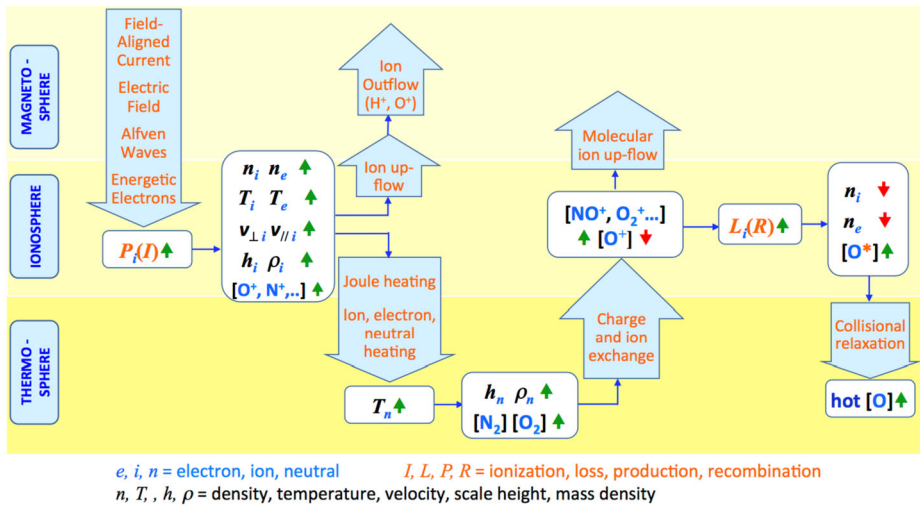


Fig. 6 A schematic illustration of the underlying physical processes of ion upflow and their importance in ionosphere-thermosphere dynamics, including (a) the energy deposition in the auroral ionosphere due to field-aligned currents, convection electric fields, Alfvén waves, and auroral electron precipitation; (b) increase in ion production P_i by electron impact ionization I , increases in ion and electron densities and temperatures (n_i, n_e, T_i, T_e), ion convection and parallel velocities ($v_{i\perp}, v_{i\parallel}$), plasma scale height and mass density (h_i, ρ_i), and O^+, N_2^+ , and N^+ ion composition; (c) ion upflows, Joule heating, and neutral heating; (d) resulting increase in the neutral scale height and mass density, N_2 and O densities, and the N_2/O density ratio; (e) increased production of molecular N_2^+, O_2^+ , and NO^+ ions in the F-region and above, due to increase in auroral electron impact ionization of N_2 and O_2 and in their charge-exchange and ion-exchange with the dominant O^+ ion

concurrent proton velocity, i.e., at nearly 25 times the energy as the main anti-sunward flux at the lunar distance in the magnetotail during geomagnetically disturbed times (Poppe et al. 2016a), which was initially interpreted as potentially containing molecular species (N_2^+, NO^+ , and O_2^+ , approximately masses m/q 28–32), but majority of this high-energy flux must be atomic ions (O^+), if not all, for this event.

2.2.1 The Importance of the Ionospheric and Thermospheric Dynamics and Energization (Upflow) for the Molecular Ions in the Magnetosphere

Figure 6 illustrates schematically the underlying physical processes of ion upflow and their importance in the ionosphere-thermosphere dynamics in the context of magnetosphere-ionosphere-thermosphere coupling, including the energy deposition in the auroral ionosphere associated with field-aligned currents, convection electric fields, Alfvén waves, and auroral electron precipitation (both energetic and soft electrons). Such energy deposition causes an increase in ion production P_i due to electron impact ionization I , and subsequently increases in ion and electron densities and temperatures (n_i, n_e, T_i, T_e), ion convection and parallel velocities ($v_{i\perp}, v_{i\parallel}$), plasma scale height and density (h_i, ρ_i), and changes in the O^+, N_2^+ and N^+ ion composition.

The resulting plasma pressure gradients and ion convection velocities give rise to ion upflows and Joule heating, respectively, as well as neutral heating due to ion-neutral collisions. The latter in turn gives rise to an increase in the neutral scale height and mass density, and a corresponding increase in both N_2 and O densities at a given altitude, with the N_2 density

increasing at a faster rate relative to O with increasing altitude, so that the increase in the N₂/O density ratio is also largest at the highest altitude.

This in turn leads to an increased production of molecular N₂⁺, O₂⁺, and NO⁺ ions in the ionospheric F-region and above, due to the combination of (a) auroral electron impact ionization of N₂ and O₂, both at increased densities, (b) charge-exchange of both N₂ and O₂ with the dominant O⁺ ion, giving rise to N₂⁺ and O₂⁺, respectively, and (c) ion-exchange reaction between N₂ and O⁺, giving rise to NO⁺. While contributing to the significant enhancement of ion upflow, these molecular ions contribute to the reduction of the overall electron density due to their rapid dissociative recombination rate in the F-region, as explained in detail below (see also Sydorenko et al. 2016), and also contribute the production of hot oxygen and nitrogen atoms in the thermosphere (see e.g., Richards et al. 1994).

2.2.2 The Importance on the Ionospheric Chemistry (Source and Re-Combination During Upflow)

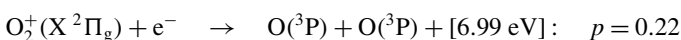
In terms of their influence on the ion composition in the Earth's ionosphere, the two most important types of chemical processes are ion-neutral charge exchange and recombination reactions. The lower thermosphere is dominated by molecular oxygen (O₂) and nitrogen (N₂), and the upper thermosphere is dominated by atomic oxygen (O) below the H-O crossover height and by atomic hydrogen (H) above, respectively. Correspondingly, the E-region ionosphere is dominated by molecular NO⁺ and O₂⁺ ions (Del Pozo et al. 1997; Grebowsky and Bilitza 2000), while the F-region and the upper ionosphere up to the crossover height is dominated by atomic oxygen ions. Above the crossover height, the topside ionosphere and beyond is dominated by atomic hydrogen ions (proton, H⁺), although the hydrogen exosphere still extends to more than 10 R_E (e.g., Kameda et al. 2017) in the proto-dominated region.

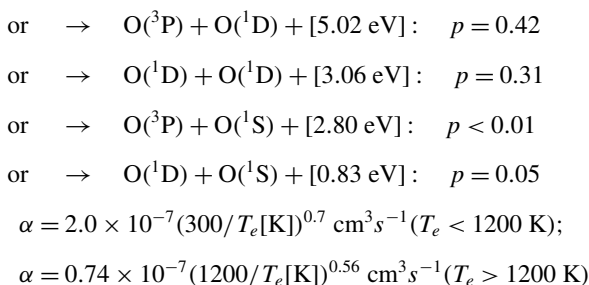
The charge exchange reactions of highest importance to the F-region and topside ionosphere are therefore those involving O⁺ and H⁺ ions, respectively, such as:



where k denotes the best accepted value of the room-temperature rate coefficient in the literature in each case.

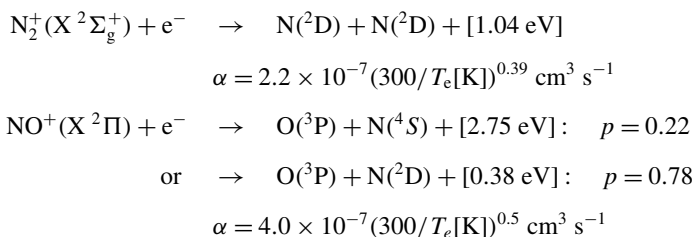
Dissociative recombination processes often dominate the ion composition (abundance) of a planetary ionosphere. In the Earth's ionosphere, the dissociative recombination of the molecular O₂⁺, N₂⁺, and NO⁺ ions is particularly important. While this reaction produces oxygen atoms and/or nitrogen atoms, some of the produced atoms are meta-stable excited electronic states, which ultimately lead to the formation of airglow and the aurora, and some atoms are 'hot atoms' in the ground electronic state with excess kinetic energy that ultimately contribute to heating of the thermosphere via their collisional relaxation with the ambient oxygen atoms. In the case of the O₂⁺, the dissociative recombination process can proceed in as many as 5 branches:





where the parameter p denotes the branching ratio, i.e., the fraction going to each branch, the value listed in the square bracket is the excess kinetic energy, and α is the dissociative recombination rate coefficient.

Similarly, in the case of molecular nitrogen (N_2^+) and nitric oxide (NO^+) ions:



where the rate coefficient of dissociative recombination α decreases slowly with increasing temperature. In the case of atomic ions, recombination with electrons has to occur via photon emission, and is quite inefficient. For example, the radiation recombination rate coefficient for the radiative recombination of Fe^+ with an electron is $8 \times 10^{-12} \cdot (300/T)^{0.51} \text{ cm}^3 \text{ s}^{-1}$ (Nahar et al. 1997), which is about 5 orders of magnitude slower than for the typical dissociative recombination reaction of a molecular ion.

In the auroral ionosphere, the dominant ion production process for atomic O^+ ion is the collisional ionization of neutral atomic oxygen (O) by precipitating auroral electrons, followed by the dissociative ionization of molecular oxygen (O_2). For atomic N^+ , the dominant ion production process is the corresponding dissociative ionization of molecular nitrogen (N_2). Likewise, the dominant ion production process for molecular oxygen and nitrogen ions (O_2^+ and N_2^+) is the electron impact ionization of molecular O_2 and N_2 , respectively. Following the treatment of Jones (1974, equation 4.2) the ion production ratio γ between N^+ and O^+ may be written semi-empirically as (see also Yau and Whalen 1992):

$$\gamma = \frac{P_N}{P_O} = \frac{[\text{N}_2]}{2.46[\text{O}] + 1.46[\text{N}_2]} \quad (2.1)$$

where P_N and P_O are the N^+ and O^+ ion production rates, respectively, and $[\text{X}]$ denotes the density of neutral species X .

Thus, in the F-region (above $\sim 150 \text{ km}$), where $[\text{O}_2] \ll [\text{O}]$, the production rate ratio γ is directly proportional to the local neutral molecular nitrogen to atomic oxygen density ratio $[\text{N}_2]/[\text{O}]$. During a large magnetic storm and an extended period of auroral substorms, the neutral N_2 density at auroral latitudes substantially increases (i.e., atmospheric scale height increases) due to the thermospheric heating. For example, based on the MSIS model, γ typically increases by a factor of 2–5 from its quiet-time value (A_p index < 5) in the 300–500 km altitude region during disturbed times ($A_p \sim 100$).

Table 5 Escape velocity (km/s) and energy (eV) for different species from certain height h and minimum energy to reach height h from 500 km altitude (inside parenthesis)

Height (h)	escape velocity	O	N ₂	Fe
500 km	10.8 km/s	9.7 eV (0 eV)	17.0 eV (0 eV)	34 eV (0 eV)
1360 km (e-Pop)	10.2 km/s	8.6 eV (1.1 eV)	15.1 eV (1.9 eV)	30 eV (3.8 eV)
1500 km	10.1 km/s	8.5 eV (1.2 eV)	14.8 eV (2.2 eV)	30 eV (4.3 eV)
1700 km (Freja)	9.9 km/s	8.2 eV (1.5 eV)	14.4 eV (2.5 eV)	29 eV (5.0 eV)
2000 km	9.8 km/s	8.0 eV (1.7 eV)	13.9 eV (3.0 eV)	28 eV (6.1 eV)
2500 km	9.5 km/s	7.5 eV (2.2 eV)	13.1 eV (3.8 eV)	26 eV (7.6 eV)
3000 km	9.2 km/s	7.1 eV (2.6 eV)	12.4 eV (4.5 eV)	25 eV (9.0 eV)
4000 km	8.8 km/s	6.4 eV (3.3 eV)	11.2 eV (5.7 eV)	22 eV (11.4 eV)
9000 km	7.2 km/s	4.3 eV (5.4 eV)	7.6 eV (9.4 eV)	15.2 eV (19 eV)
3 R _E	6.5 km/s	3.5 eV (6.2 eV)	6.1 eV (10.9 eV)	12.2 eV (22 eV)
4 R _E	5.6 km/s	2.6 eV (7.1 eV)	4.6 eV (12.4 eV)	9.1 eV (25 eV)
Venus 500 km	9.9 km/s	8.2 eV	14 eV	28 eV
Mars 500 km	4.7 km/s	1.8 eV	3.2 eV	6.4 eV

All these reactions imply that the combination of (a) auroral electron impact ionization and dissociative ionization) of molecular N₂ and O₂ and (b) the chemistry of ion-neutral charge-exchange and of dissociative recombination results in a significant increase in the N₂ to O density ratio in the F-region and topside auroral ionosphere during the geomagnetic storms and extended periods of the auroral substorms. Consequently, the molecular ion density increases in such geomagnetic conditions, resulting in the upflow of the molecular ions and the reduction in overall plasma density in the topside ionosphere.

2.2.3 Importance of the Transport Above Exobase (Above About 500 km)

Except for H⁺ and to a lesser extent He⁺, all ions need extra energies to reach the magnetosphere from the ionosphere. For heavy atomic ions such as O⁺ and N⁺, a substantial portion of the upward moving ions is bounded by gravitation and returns to the ionosphere (Yamauchi 2019, and references therein; Dandouras 2021) before acquiring sufficient additional energy in the main energization region at higher altitudes to overcome gravity and reach the distant magnetosphere (Delcourt et al. 1993; Yau and André 1997; Nilsson et al. 2008; Gronoff et al. 2020).

Table 5 summarizes the escape energies for various ions (i.e., energy required to escape Earth's gravity) from various altitudes (h), and the energy required to reach height h along a vertically oriented geomagnetic field from 500 km altitude (the exobase near solar maximum), respectively, with the latter value given inside the parenthesis. For example, O₂⁺ ions at 500 km altitude upflowing vertically need a minimum of 3.4 eV to reach 2000 km altitude and a minimum of 5.2 eV to reach 3000 km altitude (the actual required energy depends on the fraction of energy in the perpendicular direction), while half the energy is required for the O⁺ atomic ions (1.7 eV for reaching 2000 km altitude and 2.6 eV for 3000 km altitude). For comparison, the last two rows in Table 5 show the escape velocity and the corresponding energy values in Mars and Venus, respectively.

The main energization includes both electromagnetic wave acceleration (including mirror acceleration) (Gorney et al. 1982; Yau et al. 1983; Lundin and Guglielmi 2006) and electrostatic acceleration (including centrifugal acceleration) (Cladis 1986), and these main

energization regions vary with time and with locations (latitudes and MLT), with the lowest altitude of the region about 2000–4000 km altitudes.

It is not trivial for the ions leaving the exobase to acquire such “pre-energization” because the electric field (both DC and AC) available to energize the ions near the exobase is normally very small. In fact, even upflowing atomic O^+ ions often return to the ionosphere (Loranc et al. 1991; Yamauchi et al. 2005). There are several mechanisms for the required pre-energization to overcome gravity above the exobase, but predominantly through wave-particle interactions. No matter what the mechanism is, the energization is often marginally sufficient such that a small difference in m/q (by just a factor of two) may prevent a heavier mass species from reaching the main energization region while a lighter species can do so. If the pre-energization just below 2500 km altitude is only 3–4 eV while the main energization altitudes are different between the dayside and the nightside, the absence of O_2^+ outflow in the nightside can easily be explained. Thus, it is quite possible that such acceleration is sufficient only for atomic ions such as O^+ (and He^+) but not for heavy molecular ions.

Due to the velocity filter effect mentioned above, we expect upflowing molecular O_2^+ to be deflected more equatorward than upflowing atomic O^+ in the nightside auroral region before reaching the main energization region, particularly during geomagnetic storm conditions. Since the wave activity at lower latitude in the nightside sub-auroral region is lower than in the auroral region where O^+ upflow is observed (e.g., Hirahara et al. 1998; Moore et al. 1999a; Keika et al. 2013), pre-energization by the wave activity can also be smaller at O_2^+ upflow latitudes than at O^+ upflow latitudes.

In addition to the velocity filter effect inside the ionosphere, ionospheric chemistry, ionosphere-thermosphere coupling (see Sects. 2.2.1 and 2.2.2), and upward convection also play a role in determining the distribution of molecular and atomic ions at the topside ionosphere near and above the exobase. These lead to significant differences for molecular ion distributions between the cusp region and auroral region, possibly allowing molecular ions to leave the ionosphere only from the dayside. Therefore, to understand the magnetospheric molecular ions, we need to know the composition and dynamics of molecular ions at the topside of the ionosphere, too.

In this respect, it is useful to compare heavy atomic ions (O^+) and heavy molecular ions (N_2^+ , NO^+ , and O_2^+) in terms of total flux only. At high altitude (such as the altitudes of Akebono and Polar satellites) above the main energization region, heavy atomic ions (O^+) are found over a wide latitudinal range. These upflowing O^+ ions, both from the high-latitude ionosphere (cusp and its surroundings) and from lower latitude ionosphere (nightside auroral and sub-auroral regions), were found to enter the magnetosphere through various routes (e.g., Yamauchi 2019 for review). By contrast, the cusp source dominates the heavy molecular ion population in the magnetosphere in both occurrence and ion flux at the Akebono altitude (Yau et al. 1993).

If energy-time profiles for molecular ions can be obtained in observations, they will provide information about the main energization mechanisms (electrostatic (DC) and electromagnetic (AC)) because they have different mass-per-charge dependences of the energy gain (ΔE), from no dependence on the mass for the electrostatic acceleration to complicated mass dependency (due to requirement on resonance) for the electromagnetic wave energization. With knowledge about the altitude dependence of the flux ratio between different masses and energies, one can estimate the relative importance of different mechanisms at different altitudes, although the feasibility of such measurements is not evident. While the electrostatic (DC) acceleration is normally strong enough to give sufficient energy for all ions (independently of their mass) to reach high-altitude, such DC acceleration does not start below 2000 km altitude, and hence, heavy ions with only a few eV at the exobase often return to the ionosphere before experiencing such a DC acceleration (see Table 5).

The detection of heavy ions also gives clues on the altitude where the electromagnetic (AC) acceleration starts. Here, the AC acceleration might start from much lower altitudes during magnetic storms or other conditions, but details are unknown. If AC acceleration is strong enough and starts at low enough altitudes, even metallic ions may reach the DC acceleration region. Therefore, quantification of heavy ions in the magnetosphere provides information on the strength and altitudes of the AC acceleration.

2.2.4 How Much of the Change in Atmospheric Composition (e.g., N₂/O₂ Ratio) on Geological Time Scales Is Caused by Ion Escape?

Evolution of the Earth's atmosphere is another science theme that benefits from our knowledge of magnetospheric molecular ions (N₂⁺, NO⁺, and O₂⁺), in addition to atomic heavy ions N⁺ and O⁺ (e.g., Yamauchi 2019). The present atmospheric composition is quite different from that of the other planets (Mars and Venus) after 4.5 billion years of evolution although the initial atmospheric compositions of Mars and Venus are believed to be similar to that of the Earth (Lammer et al. (2008). The difference in the atmospheric evolution must have influenced the habitability of these three planets: very limited habitability in the best case for Mars (possible underground habitats where water exists) and Venus (cloud layer where temperature is in the habitable range) compared to the full habitability for all known forms of life on the Earth.

From the viewpoint of evolution of life, a very small change in atmospheric composition is important. A change of only a few percent in the atmospheric O₂/N₂ ratio or in the water pH, or a temperature change of a few degrees of the atmosphere and/or ocean may significantly affect the biochemical reactions and hence metabolism and photosynthesis (e.g., Loesche 1969; Hill 1976; Servaites 1977; Ku et al. 1977; Harrison et al. 2010). A change of a few percent in the atmospheric N/O ratio corresponds to a change of about 10% in the nitrogen inventory in the present-day biosphere ((4–5) × 10¹⁸ kg). This amount of loss is achieved within 600 million years (= 2 × 10¹⁶ sec) by an average nitrogen loss rate of 10²⁷ s⁻¹ (about 20 kg/s). The same level of change (15% fluctuation in O₂ content) has actually occurred over 100 million years in the past according to the geological record (Berner 2006). These durations and amounts are short enough compared to the history of life and large enough in quantity, respectively, to affect bacteria through change in the N/O ratio in the atmosphere.

In addition, the simultaneous presence of significant amounts of N₂ and O₂ in an atmosphere is chemically incompatible over geological timescales, and hence, the present N₂/O₂ ratio must have resulted from biological activity (Lammer et al. 2019; Stüeken et al. 2020; Dandouras et al. 2020), constituting a bio-signature.

The question is then what causes such changes and fluctuations of the atmospheric composition. There are six main channels that determine the evolution of the atmosphere: (a) net escape to space after removing the return flow; (b) net influx from space (e.g., meteors); (c) biospheric reactions (e.g., O₂ from photosynthesis); (d) sub-surface sink through ocean bottom; (e) emission from sub-surface through both non-organic (e.g., volcanic) and organic activities (bacterial denitrification) (Berner 1999; Canfield 2005; Barabash et al. 2007; Johnson and Goldblatt 2015); and (f) geochemistry (e.g. CO₂ chemical capture through limestone formation) (Stüeken et al. 2020).

Among these, the net contributions of the biosphere (c) and from the Earth's interior (d and e), respectively, diminish once photosynthesis and mantle convection are stabilized because these contributions mainly recycle elements rather than causing net changes. Also, the net influx of biological elements (N, O, C) from space (b) is much smaller than that of escape to space. On the other hand, (a) the escape to space causes net changes, and therefore

its relative importance compared to the sub-surface migration is large on the geological time scale. The question is: how much?

The nitrogen escape rate to space of 10^{27} s^{-1} mentioned above is not unrealistic during the ancient time of about 4 billion years ago, because the composition and amount (flux) should depend strongly on the solar UV, solar wind, and geomagnetic activity conditions, all of which are known to be much higher in the ancient time on the geological time scale than at present (Yamauchi 2019; references therein). This means that we can assume frequent occurrence of extremely severe geomagnetic storms that correspond to Kp more than 9 at that time (Krauss et al. 2012). Considering the ion escape rate to be exponentially proportional to Kp (Slapak et al. 2017a), increased frequency of high Kp activity allows us to assume $Kp \sim 10$ in estimating the average ion escape rate in the ancient time on the geological time scale, rather than a summation of short-lived events of “massive escape” for lower Kp as in the present days. Assuming the escape rate to decrease linearly with time, Slapak et al. (2017a) estimated the total loss of heavy atomic ions (O^+ and N^+) over 4 billion years at about $5 \times 10^{17} \text{ kg}$, which corresponds to 40% of today’s total oxygen mass in the atmosphere.

For such a condition, i.e., during an enhanced outflow rate, energization of the ionosphere is also enhanced, allowing even molecular ions (N_2^+ , NO^+ , and O_2^+) to gain sufficient initial velocity to enter the outflow process (few-tens of eV) within their relatively short dissociative recombination lifetime. Therefore, during “massive escape” events, flux enhancement of the ion outflow becomes more drastic for molecular ions than for atomic ions (and for atomic ions, the N^+ outflow is more enhanced than the O^+ outflow). These factors cause a higher N/O ratio of the atmospheric loss during enhanced outflow rate, and hence in the ancient time in the geological time scale.

The high N/O ratio of escaping elements is consistent with what has been observed in the very sparse observations that simultaneously detected the molecular ions (Yau et al. 1993; Hamilton et al. 1988). However, no quantitative value for N/O ratio or even the molecular/atomic ratio for ion outflow flux (or upflow flux at low altitude) is available in the published literature to date, to our knowledge, due to a lack of dedicated instruments on magnetospheric missions covering a wide variety of escape routes and energy ranges. From the detection capability viewpoint, although quantitative separation of N^+ and O^+ requires much higher $m/\Delta m$ capability than separating molecular ions (N_2^+ , NO^+ , or O_2^+) from atomic ions (N^+ or O^+), capable instruments have already been flown on board planetary missions such as Cassini, Kaguya, MAVEN, BepiColombo, and JUICE.

2.3 Importance and Present Knowledge of the Mesospheric Sources (Metallic Ions)

Figure 3 demonstrates the existence of accelerated ($> 100 \text{ keV}$) low charge-state metallic ions (such as Fe^+) in the magnetosphere, although their flux is much lower than the flux of the solar wind metallic ions entering the magnetosphere. This also indicates that some ions with $m/q \approx 30$ can also be Si^+ . The low charge-state indicates that they must come from either from the Moon (see Sect. 2.4) or the atmosphere. Although metallic species are a very minor component of the atmosphere, there are several layers of metallic species in the upper mesosphere and lower thermosphere, mainly from the ablation of cosmic dust entering the Earth’s atmosphere, as illustrated in Fig. 7.

2.3.1 Meteoroids and the Metal Layers

Every day the Earth’s atmosphere is bombarded by billions of micrometer-sized dust particles and larger pieces of material from space. The primary sources of these cosmic dust

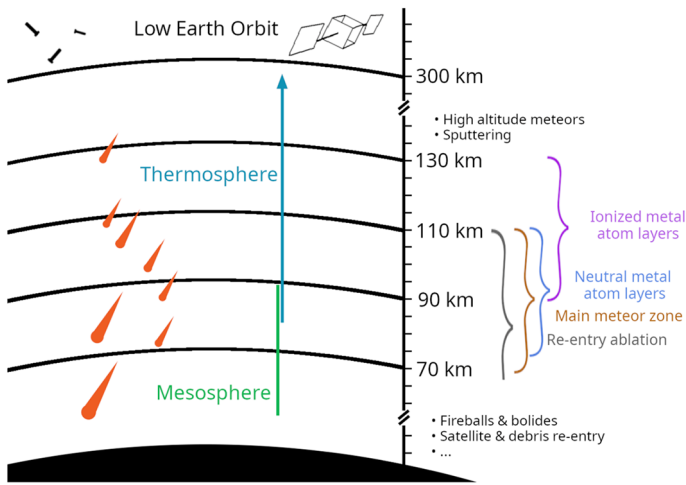
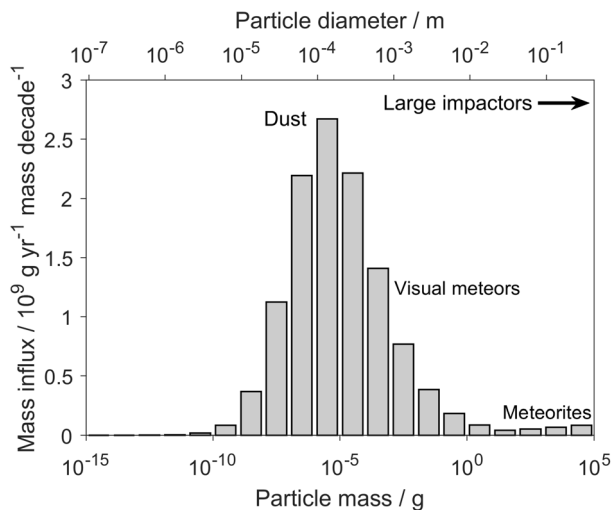


Fig. 7 Illustration of the ablation of material entering the atmosphere, showing relevant altitude ranges

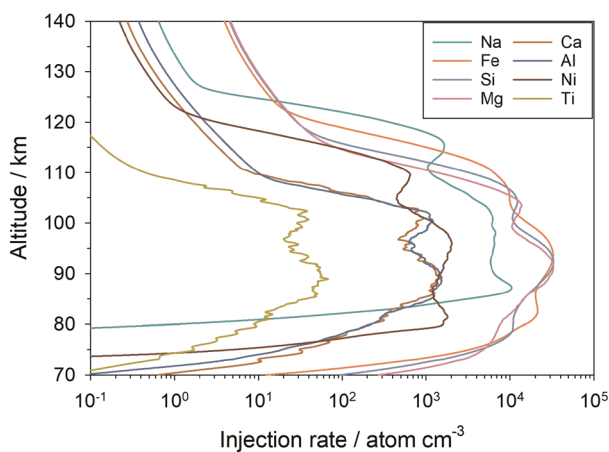
Fig. 8 The annual meteoroid mass influx (expressed per decade of mass) plotted against particle mass, adapted from Plane et al. (2018) and Schulz and Glassmeier (2021)



particles are the sublimation of volatile species in comets as they are heated by the Sun, which release dust particles that are then ejected by drag forces, and collisions between asteroids in the main asteroid belt between Mars and Jupiter (Plane et al. 2018). These particles are collectively termed meteoroids. Because the particles range in size by more than 12 orders of magnitude as shown in Fig. 8 (Murad and Williams 2002), estimating the total input of cosmic dust into the atmosphere is very challenging, with estimates ranging from roughly 5–300 t d⁻¹ (tonnes per day) (Plane 2012).

The most likely value currently is thought to be around 30 t d⁻¹, based on measurements of the vertical fluxes of Na and Fe atoms which ablate from dust in the lower thermosphere and upper mesosphere, and the accumulation of cosmic spherules (dust particles that melt but do not completely evaporate) at the South Pole (Carrillo-Sánchez et al. 2020). This input rate is corroborated by the optical extinction of meteoric smoke particles (which form from

Fig. 9 Global average ablation rates as a function of altitude for the main metal constituents in cosmic dust (Carrillo-Sánchez et al. 2020)



the polymerization of metallic compounds produced from ablated metal atoms) in the lower mesosphere (Hervig et al. 2021), and the accumulation of unmelted micrometeorites in a large collection from Concordia in Antarctica (Rojas et al. 2021) as well as earlier estimates considering their respective biases (Schulz and Glassmeier 2021, and references therein).

As meteoroids enter the atmosphere, they undergo heating by inelastic collisions with molecules of the atmosphere. If the meteoroids reach the melting point (~ 1800 K), then ablation (i.e., evaporation) of the constituents becomes rapid. Initially the relatively volatile elements (Na and K) ablate, followed by the main constituents (Fe, Mg and Si) around 2000 K. Finally, the refractory elements (Ca, Al and Ti) ablate if the particle reaches a temperature over 2400 K (Vondrak et al. 2008). Figure 9 shows the ablation rates of the individual elements as a function of altitude, illustrating that most ablation occurs between 70 and 110 km (Carrillo-Sánchez et al. 2020). This injection is the source of the layers of neutral metal atoms that occur globally between about 75 and 110 km, and the layers of ionized metal atoms between about 90 and 130 km (Plane 2003; Plane et al. 2015)

Metallic atoms have comparatively low ionization energies. Since they are initially travelling at the same speed as their parent meteoroid, they can undergo collisional ionization with air molecules. The meteoroid energy velocity ranges from 11 km s^{-1} to 72 km s^{-1} , and the ionization probability strongly depends on the velocity (see Fig. 3 in Janches et al. 2017). The resulting dense plasma, together with optical emissions from atoms and molecules in excited electronic states, is termed the meteor, which moves together with the ablating meteoroid (Ceplecha et al. 1998). If the meteoroid survives the ablation process and reaches the ground, it is termed a meteorite. Note that the analysis of meteorites and observations of meteor spectra provide conclusive evidence that the meteoroid population contains metallic elements roughly in same abundance as the photosphere (Asplund et al. 2009; Lodders et al. 2009; Kero et al. 2019).

There have also been rare observations of the meteor phenomena at altitudes up to 200 km. For optical observations these events have been mainly explained by sputtering (non-thermal ablation) (Popova et al. 2007). With sufficient meteoroid size and velocity, sputtering can create enough photons to be detected by optical systems (Koten et al. 2006). The majority of published optical observations of high-altitude meteors originate from the Leonid meteor shower due to its very high velocity (about 70 km s^{-1}). These events are also characterized by the sputtering-dominated part of the meteor event with a brightness that is several orders of magnitude fainter than the thermal ablation part, indicating that a much

smaller part of the meteoroid mass is lost at these altitudes (Vondrak et al. 2008). High altitude meteors have also been observed with radars. However, the very high-altitude cases (> 150 km) are still an open question due to possible ambiguities in the observation techniques (Brosch et al. 2013; Vierinen et al. 2014; Gao and Mathews 2015). Radar observations of high-altitude meteors up to 142 km have been validated with respect to such ambiguities (Kastinen and Kero 2022) and may be explained by thermal ablation, particle disruption, and/or the pyrolysis of refractory organics within the dust particles (Bones et al. 2022).

To determine the altitude and element distribution of mass deposition in the atmosphere, the meteoroid atmospheric entry needs to be modelled. For an overview of modelling the atmospheric entry of meteoroids, see Ryabova et al. (2019, and references therein). These models have been widely used for determining the physical properties of meteoroids from observations (e.g., Gritsevich 2009; Campbell-Brown et al. 2013), and for estimating the injection flux of metals into planetary atmospheres as input when modelling the atmospheric chemistry and dynamics in the mesosphere and lower thermosphere (Plane et al. 2015). In recent years, chemical ablation models have been tested using different types of laboratory meteoric ablation simulators (Gomez Martín et al. 2017; Thomas et al. 2017) to constrain chemical ablation models, such as the CABMOD model which now includes separate metal silicate and Fe-Ni-S phases (Bones et al. 2019).

Hulfeld et al. (2021) simulated the break-up of dustball meteoroids using a fluid dynamics model of the meteoroid's atmospheric entry flow, including both thermal and mechanical break-up mechanisms. A Draconid meteoroid was simulated starting with compression by the aerodynamic forces to approximately half its size at the beginning of the simulation (200 km altitude), and then mechanically disintegrated at 120 km altitude due to aerodynamic-induced meteoroid rotation. In contrast, camera and radar observations of Draconids show a lower break-up altitude of about 100–110 km (Borovička et al. 2007, 2014; Kero et al. 2012). These studies indicate that there may be an additional influx of meteoroid material that disperses (i.e., ablates) at higher altitudes than regular thermal ablation of a single solid body allows.

2.3.2 Observations of Metallic Ions in the Thermosphere and Ionosphere

Metallic ions in the lower thermosphere (lower ionosphere) have long been detected and observed by both in-situ observation (rockets and satellites) and remote observation (ground and satellites), although the spatial and temporal resolution at higher altitude is insufficient to reveal the vertical transport.

(a) Spaceborne observations

For in-situ sampling, the mass spectrometer on board Atmosphere Explorer C (AE-C) satellite detected patches of Fe^+ between 220 and 320 km that seemed to be associated with regions of upward plasma transport Grebowsky and Brinton 1978. Moreover, the retarding potential analyser (RPA) on board OGO-6 satellite occasionally observed Fe^+ at much higher altitudes between 600 and 950 km (Hanson and Sanatani 1971; Hanson et al. 1972). Measurements of metallic ions up to around 130 km have been made using ion mass spectrometers on sub-orbital rockets, mostly at mid- and high-latitude locations. This type of experiment provides vertical profiles with typically 2 km height resolution of all ions with masses below ~ 100 amu and concentrations larger than $\sim 10 \text{ cm}^{-3}$, but not at middle and upper ionosphere. These measurements were mostly made in the 1970s and 1980s (for review, Kopp 1997; and Grebowsky and Aikin 2002).

Metallic species such as Mg^+ and Fe^+ have also been observed by resonant scattering of sunlight, for example by the Space Shuttle (Gardner et al. 1995, 1998). An optical spectrometer, Ionospheric Spectroscopy and Atmospheric Chemistry instrument (ISAAC) on board

the United States Air Force's Advanced Research and Global Observing Satellite (ARGOS), detected clear Fe⁺ emission in the 100–340 km altitude region (Dymond et al. 2003). In the last 15 years, spaceborne limb-scanning optical spectrometers have been used to determine the vertical profiles of metal atoms and ions: the OSIRIS spectrometer on board Odin satellite for Na (Hedin and Gumbel 2011) and K (Dawkins et al. 2014); and the SCIAMACHY spectrometer for Mg and Mg⁺ (Langowski et al. 2015) and the GOMOS spectrometer for Na (Fussen et al. 2010), both on the Envisat satellite.

(b) Resonance lidars

The first measurements of metal atom densities (Na, K, Fe and Ca⁺) in the upper mesosphere were made in the 1950s using ground-based twilight photometry, where resonance fluorescence from spectroscopic transitions of metal atoms excited by solar radiation was measured during twilight (Hunten 1967). These measurements were superseded in the 1970s when the development of tunable lasers led to the resonance lidar technique (Plane 1991). Lidar has been used to observe Na, K, Li, Ca, Ca⁺ and Fe (Plane 1991), and recently Ni (Gerding et al. 2019). Most of these observations have focused on the main metal layers between 75 and 110 km.

One important development in the past 15 years has been the use of high performance lidar observations even to the thermosphere: observations of Fe (Gao and Mathews 2015) and Na (Liu et al. 2016) are extended to above 150 km, K and Ca up to 130 km (Höffner and Friedman 2004, 2005; Friedman et al. 2013), and Ca⁺ up to 180 km (Raizada et al. 2020). Even diurnal observations have become possible (Plane 2003). Thus, it has long been known that these metallic species exist at detectable levels in the lower thermosphere and ionosphere.

2.3.3 Transport to the Exobase

In the thermosphere, metals exist almost entirely as metallic ions after their efficient ionization either by charge exchange with ambient NO⁺ and O₂⁺ ions, or by photoionization (Plane et al. 2015). Unlike the molecular ions such as NO⁺ which undergo rapid dissociative recombination with electrons, metallic ions can only undergo dielectronic or radiative recombination with electrons, a process about 10⁶ times longer lifetime (Plane et al. 2015). Thus, the metallic ions have lifetimes of days in the thermosphere.

Furthermore, some metallic ions like Na⁺ ($m = 22$), Mg⁺ ($m = 24$), Al⁺ ($m = 27$), Si⁺ ($m = 28$), P⁺ ($m = 31$), and S⁺ ($m = 32$) have similar or even smaller m/q compared to heavy molecular ions, allowing them to be lifted upward longer distances than heavy molecular ions with the same uplifting forces (e.g., electric field and electromagnetic waves). Such long upward distances even apply to the other relatively abundant heavy metallic ions, such as K⁺ ($m = 39$), Ca⁺ ($m = 40$), SiO⁺ ($m = 44$), Fe⁺ ($m = 56$), Ni⁺ ($m = 59$) and Cu⁺ ($m = 64$), because their m/q are within a factor of two of the heavy molecular ions listed in Table 6 (here, we note that mass 44 in the magnetosphere is not necessarily CO₂⁺, but could also be SiO⁺ of lunar origin).

Since molecular ions must be transported from the lower ionosphere to reach the exobase within the dissociation timescale, the same “strong” upward ion convection in the ionosphere may also transfer metallic ions against gravity (particular those lighter than O₂⁺) from the lower ionosphere. Inversely, the detection of the heavy molecular ions ($m/q \approx 30$) above the ionosphere by e-POP suggests that metallic ions may also access the topside ionosphere (exobase). If one can measure the ratio of metallic ions to molecular ions of similar masses for the outflowing ions above the ionosphere, the variation of this ratio would indicate change in convection and/or the effect of chemical reactions.

Table 6 Metallic elements and their mass

ions	mass	molecular ions with same mass	space debris
Na ⁺	m = 23		
Mg ⁺	m = 24		
Al ⁺	m = 27	HCN ⁺	yes
Si ⁺	m = 28	N ₂ ⁺ , CO ⁺	yes
P ⁺	m = 31	¹⁵ N ¹⁶ O ⁺ or ¹⁴ N ¹⁷ O ⁺	
S ⁺	m = 32	O ₂ ⁺	
K ⁺	m = 39		
Ca ⁺	m = 40		
SiO ⁺	m = 44	CO ₂ ⁺	
Ti ⁺	m = 48		yes
Fe ⁺	m = 56		yes
Ni ⁺	m = 59		yes
Cu ⁺	m = 64		yes
Ge ⁺	m = 73		yes

Unfortunately, no dedicated instrument or mission (as suggested in Sect. 5) exists in a terrestrial orbit to monitor such ions leaving the ionosphere or arriving at the topside ionosphere from lower altitudes. Even estimating orders of magnitude of the expected flux is extremely difficult. Meanwhile, modeling efforts have advanced to include the metallic ions and atoms, as described in Sect. 4.3.3.

2.3.4 Possible Human-Made Contribution by Atmospheric Re-Entry of Space Debris

Out-of-service satellites, rocket bodies, and subsequent fragmented parts, together constitute space debris. Their re-entering into Earth's atmosphere causes the same ablation process as the entry of meteoroids although with much smaller entry velocities (~ 8 km/s), shallower entry angles and different composition, resulting in the deposition of metallic atoms and ions into the upper atmosphere (Schulz and Glassmeier 2021). Returning spacecraft with astronauts and goods may experience the same process, but the degree of ablation is much smaller than that of space debris for which re-entry is designed to result in complete ablation, and therefore this is included in the category of "ablation of space debris" or a wider terminology of "ablation of space waste".

Currently, the mass injected into the atmosphere by re-entering space debris is only a fraction (about 3% in 2019) of what is injected by meteoroids (Schulz and Glassmeier 2021). However, metallic species are present in much higher fraction in space debris than in meteoroids, resulting in the atmospheric re-entry flux of some metallic species (mainly Al and Li, but also Ni, Cu, Ti, and Ge) from space debris surpassing the entering flux of the same species from meteoroids. For these species, the annual mass input to the whole atmosphere will exceed or has already exceeded the natural input considering the strong increase in launch activity every year. The details of such future increase and its implications are discussed in Sect. 4.3.2. All this poses the question how much the input of re-entering space debris contaminates the natural origin metallic atoms and ions in the mesospheric metal layers. To answer the question, knowledge about the ablation characteristics of entering space debris and the subsequent chemical processes are vital.

For re-entering space debris, ablation starts as high as 110 km (Fritsche et al. 2000; Klinkrad 2005; Rafano Carná and Bevilacqua 2019) which is ~ 20 km lower than for meteoroids. For larger spacecraft (few 100 kg or more), the main part of mass loss takes place at altitudes below 80 km depending on the spacecraft velocity, entry angle, mass, and composition (Reynolds et al. 2001; Lips et al. 2005; Battie et al. 2013; Buttsworth et al. 2013; Jenniskens et al. 2016 and Park et al. 2021). For example, debris on a very elliptic orbit (high-apogee) enters the atmosphere with higher velocity and angle than low-Earth orbit (LEO) debris. Note that Buttsworth et al. (2013) and Jenniskens et al. (2016) considered non-typical re-entries (very high apogee orbits, thus a very high entry velocity and angle compared to LEO spacecraft), allowing the spacecraft to survive to lower altitudes with long-lasting ablation.

Metallic atoms that ablate below 80 km will quickly be oxidized to metal oxides, hydroxides and carbonates (Grebowsky et al. 2017). For instance, an Fe atom that ablates at around 64 km will be oxidized to FeO by O_3 in about 2 s (Grebowsky et al. 2017), and Al will be oxidized by reaction with O_2 much more rapidly (Plane et al. 2021). Oxidized metallic species that form below 80 km as a result of the ablation of space debris will rapidly polymerize with themselves or the background population of nanometer-sized meteoric smoke particles that are produced from meteoric ablation (Plane et al. 2021). These tiny particles will then be transported down to the Earth's surface by the residual atmospheric circulation. An increase in the number and size of these particles as a result of space debris may have some effect on the stratospheric ozone layer (e.g. freezing polar stratospheric clouds droplets (James et al. 2018) or removing the main chlorine reservoir HCl (Plane 2003)). However, the particles are very unlikely to be transported above 90 km and provide a source of thermospheric metallic ions after decomposing.

In contrast, for metals that ablate from space debris above 80 km, the high background concentrations of atomic O and H in the upper mesosphere (Plane 2003) will maintain a high level of metal atoms (or AlO in the case of Al) because they reduce metal oxides and other compounds. These metals may then be transported to the lower thermosphere, analogously to the transport of atoms from the natural metal layers, and ionized.

2.4 Importance of the Moon as Source and Present Knowledge (Sputtering and Pickup Process)

The Moon is a source of heavy ions. These ions are generated on the lunar surface either directly sputtered from the lunar surface by impact of solar wind plasma or magnetospheric plasma (Yokota et al. 2009; Wieser et al. 2010), or by the photoionization (solar UV and EUV) of the neutral exosphere (Stern 1999). These exospheric neutrals are originally generated by (1) micro-meteorite impact vaporization, (2) solar photon stimulated desorption, (3) sputtering by the solar wind and magnetospheric ions, and (4) thermal desorption (Colaprete et al. 2016; Wurz et al. 2022).

Since these Moon-origin ions are typically high mass but singly charged, m/q values are much higher than those of the solar wind ions (all species have similar m/q within a factor of 2). Therefore, the gyroradius of the Moon-origin ions after gaining the solar wind speed due to the pick-up process is quite different from those of the solar wind. This uniqueness of the lunar metallic species makes even a tiny amount of the ion as a tracer to give extra information in the ion dynamics at the magnetospheric boundary.

2.4.1 Formation of the Exosphere and Ion Pickup

The lunar exosphere, although very thin according to Apollo observations (Stern 1999), has been observed by Ultraviolet-Visible Spectrometer (UVS) on board LADEE (Mahaffy et al.

2015; Halekas et al. 2015). The column densities of alkali elements (K and Na) on the Moon observed by LADEE increased during the meteor shower events by a factor of 2–3 during its mission from November 2013 to April 2014 (Colaprete et al. 2016). For the Leonid meteor shower (November) and Geminid meteor shower (December), response was sharper for K than Na, whereas for Quadrantid meteor shower (January) the response was small and nearly the same for both elements. These meteor showers are more important than CIRs or CMEs (no big change is seen during the observed period) and slightly more important than the Moon phase (factor of 2 increase when the moon is at the Earth's magnetotail) for the production of the exospheric neutrals (Colaprete et al. 2016).

As for the composition, the Neutral Mass Spectrometer (NMS) on board LADEE observed lunar exospheric ions (at low energies < 25 eV) in the lunar orbit when the Moon was in the solar wind. Using the dedicated ion mode (Mahaffy et al. 2015), ions of expected species of the lunar exosphere were recorded at masses 2 (H_2^+), 4 (He^+), 16 (O^+), 20 (Ne^+), 23 (Na^+), 39 (K^+), and 40 (Ar^+) amu, but also of unexpected ions including $^{12}\text{C}^+$, $^{14}\text{N}^+$ and at mass 28, which could be Si^+ , N_2^+ or CO^+ (the presence of ^{12}C (Halekas et al. 2015) suggests that it is most likely CO^+). These observed ions originate from the exosphere, rather than directly from the surface (Mahaffy et al. 2015).

The Lunar Dust Experiment (LDEX) on board LADEE showed that the electric current, which is most likely monitoring the lunar pickup ions, is linearly correlated with the solar wind flux (Poppe et al. 2016b, Fig. 3). The reported ion fluxes are best fit by total exospheric ion production rates of about $6 \times 10^3 \text{ m}^{-3} \text{ s}^{-1}$. Since LDEX does not have a means to identify the mass of the recorded ions, the ion composition was inferred based on modelling with dominant contributions from Al^+ , CO^+ , and Ar^+ .

2.4.2 Sputtering from the Lunar Surface

Sputtering from the lunar surface is theoretically expected (Yokota and Saito 2005; Futaana et al. 2006; Wurz et al. 2007) and actually observed by Kaguya (pre-launch name: SELENOlogical and ENgineering Explorer (SELENE)) and Chandrayaan-1 lunar orbiters. Kaguya Ion Mass Analyzer (IMA) detected the sputtered ions of many species together with the ionized exospheric neutrals and the reflected solar wind ions (Yokota et al. 2009; Tanaka et al. 2009). Chandrayaan-1 Sub-keV Atom Reflecting Analyser (SARA) detected sputtered neutral hydrogen and heavy atoms of oxygen mass group (Wieser et al. 2010; Vorburget et al. 2014).

The sputter yields from most surfaces are energy dependent, and the yield approaches zero for lower energies because the energy deposited in the surface by the impacting ion is not sufficient to overcome the binding energy of atoms at the surface. The sputter yield also approaches zero for very high energies because high-energy ions penetrate deeper into the solid without depositing significant energy at or near the surface to cause the release of particles. The maximum sputter yield is expected at an energy around 1 keV/nuc of the impacting ions for the lunar case (Wurz 2012; Wurz et al. 2022), which compatible with ions with the solar wind velocity (for all species) and with the thermal magnetospheric plasma (light ions).

This means that we expect effective sputtering from the lunar surface when the Moon is exposed to the solar wind. Particularly, we expect drastic increases in the surface sputtering by CMEs (Leblanc et al. 2022) because a CME is accompanied by drastic flux enhancements of the heavy ion component: the degree of flux increase is much greater than that for H^+ (Wurz et al. 2001, 2003; Wimmer-Schweingruber et al. 2006). The effective sputtering is even expected in the magnetospheric plasma lobe or magnetosheath. On the other hand,

contribution by EUV (ionization of exospheric heavy atoms by EUV) should not cause such drastic change compared to the sputtering contribution because the solar flare that is very short-lived.

Elphic et al. (1991) conducted a laboratory study of the ion emission caused by ion impact on materials (sputtering) with solar wind-like ion and material analogue to the lunar surface. Using H^+ and He^{++} primary ions, they found that these ions produce significant fluxes of sputtered ions (so-called secondary ions) of lunar surface material, including Na^+ , Mg^+ , Al^+ , Si^+ , K^+ , Ca^+ , Ti^+ , Mn^+ , and Fe^+ , although H^+ and He^{++} are not efficient sputterers. The predicted secondary ion fluxes from the lunar surfaces is between ~ 10 and 10^4 ions $cm^{-2} s^{-1}$, depending on the species. Thus, the range of relative ion yields covers four digits of variation depending on sputtered ion species. Similar studies were performed on Apollo soils (soil number 10084 and soil number 62231) and on a synthetic Corning glass lunar simulant (Dukes and Baragiola 2015). X-ray photoelectron spectroscopy was correlated with the spectra of secondary ions ejected from these soils by 4 keV He ions. The ejected secondary ion species from the Apollo soils by 4 keV He include the atomic ions: Na^+ , Mg^+ , Al^+ , Si^+ , Ca^+ , Ca^{++} , Ti^+ , Fe^+ , and molecular the ions: NaO^+ , MgO^+ and SiO^+ .

Yokota and Saito (2005) modelled the ion production near the Moon, at 100 km above the surface, including photoionization of the lunar exospheric atoms, photon-stimulated ion desorption, and ion sputtering. They proposed that an intense flux of picked-up lunar ions (10^4 $cm^{-2} s^{-1}$) exists at an altitude of 100 km, for nearly a quarter of the orbit, with the main contributions from Na^+ , Mg^+ , Al^+ , Si^+ , K^+ , Ca^+ , Ti^+ , Mn^+ , and Fe^+ ions. In another model by Sarantos et al. (2012), ion species of Ti^+ , Fe^+ , Mg^+ , and especially Ca^+ are mainly ejected from the surface, and ionization of the exospheric constituents produces and ejects the other species, leading to the estimated fluxes that significantly exceed the ion production rate at the surface. These sputtering yields also depend on the lunar geographical areas (Futaana et al. 2006) as confirmed by Chandrayaan-1 (Wieser et al. 2010).

2.4.3 Amount and Composition of Ions Leaving the Moon: Kaguya Observation

Kaguya/IMA made the first in-situ detection of the heavy ions originating from the lunar surface and exosphere in a polar orbit with an altitude of 100 km, 50 km, and in an elliptical orbit with perigee altitude as low as 10 km (Saito et al. 2010). Kaguya/IMA is capable of detecting Moon-origin ions (both sputtering ions directly from the surface and pickup ions in the terminator region) for energy up to 12 keV/q. In their observation at 100 km altitude, Kaguya/IMA detected heavy ions including C^+ , O^+ , Na^+ , K^+ , and Ar^+ originating from the lunar surface or its exosphere (Yokota et al. 2009; Lee et al. 2024) when the Moon was located in the solar wind.

The Kaguya/IMA observation confirms that the sputtered ions have energies of about a few hundred eV in most cases, in agreement with the above expectation (Yokota et al. 2009, 2020; Tanaka et al. 2009). Figure 10a shows an example of such Kaguya observation. However, when a CIR (Corotating Interaction Region) passed the Moon carrying enhanced IMF and solar wind speed (which causes also an enhanced convection electric field), the energy of the sputtered heavy ions can become even higher than the incident solar wind proton energy, as shown in Fig. 10b. More importantly, the ion flux of heavy ions drastically increased during the CIR passage, as shown in Fig. 11 (same events as Fig. 10). Note that the CIR contains H^+ , He^{++} , He^+ , C^+ , O^+ , Na^+/Mg^+ , Al^+/Si^+ , P^+/S^+ , K^+/Ar^+ , Mn^+/Fe^+ . Existence of the high-energy low charge-state metallic heavy ions associated with CIRs indicates that the contribution of the solar wind sputtering becomes important when the solar wind pressure is high.

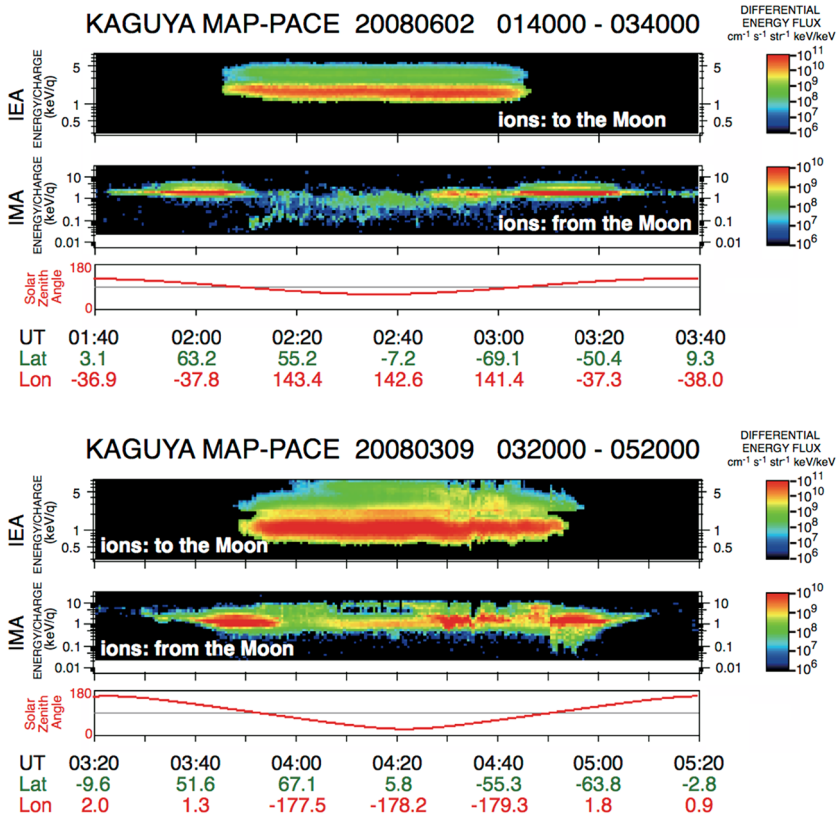


Fig. 10 Energy-time spectrogram of ions observed by MAP-PACE on Kaguya during (a) normal solar wind condition on 2 June 2008, and (b) CIR on 9 March 2008. Moon is located upstream of the bow shock in the subsolar region. Ions measured by IEA (without mass separation) looking above the spacecraft (injection to the Moon surface) and Ions measured by IMA (with mass separation) looking downward the spacecraft (emission from the Moon surface) are shown

The Moon-origin ions were also detected even when the Moon stayed in the Earth's magnetosphere lobes (Tanaka et al. 2009), where the direct impact of the solar wind is less pronounced. These ions were observed on the dayside of the Moon, especially when the solar zenith angle was below 40 degrees. IMA detected peaks of flux for the heavy ions including C^+ , O^+ , Na^+ , K^+ , and Ar^+ . These ions were mostly accelerated by the convection electric field in the Earth's magnetotail. The ions originating from the lunar surface and the exosphere showed characteristic variation of the flux intensity that presumably related to the lunar surface structure or composition.

When the Moon stayed in the Earth's magnetosphere, during a high geomagnetic activity period, the IMA instrument detected both lunar O^+ ions, originating from the Moon surface, and energetic O^+ ions originating from the Earth's ionosphere and streaming downtail (Teraida et al. 2017). These two O^+ populations are clearly distinguished from their distribution functions and their energy spectra, the terrestrial O^+ ions streaming downtail with energies of the order of few keV whereas the lunar O^+ ions have energies of the order of ~ 10 eV.

With the ion electrostatic analyzer on board ARTEMIS, lunar pickup ions were observed when the Moon was within the terrestrial magnetotail lobe (Halekas et al. 2012; Poppe et al.

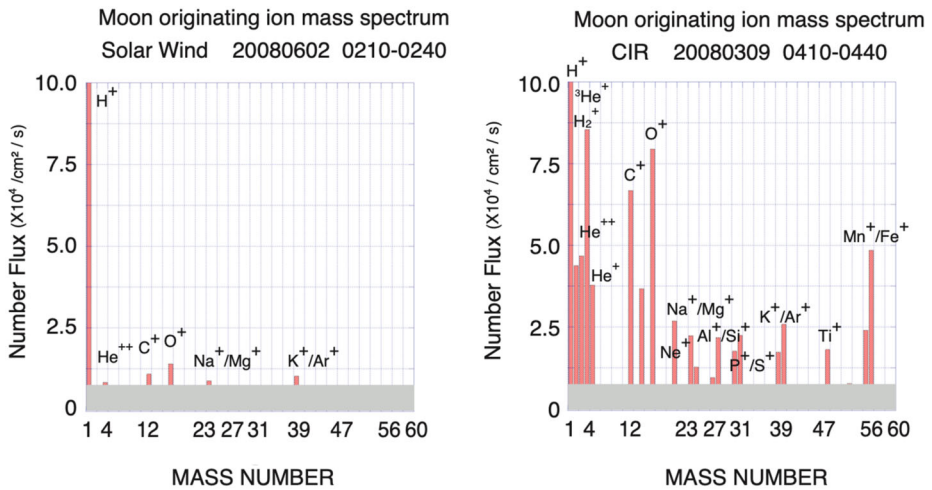


Fig. 11 Number fluxes of ions coming from the lunar surface for the same days as Fig. 10. Left: during a normal solar wind condition (2 June 2008, Fig. 10a). Right: during a CIR (9 March 2008, Fig. 10b). Low charge-state indicates that they are sputtered ions from the lunar surface rather than reflected solar wind. In both cases Kaguya was located upstream of the bow shock

2012). Although ARTEMIS does not have any instrument that can separate the mass, it is possible to infer the existence of heavy ions if accurate ion and electron densities can be obtained. Assuming that the density calculation is accurate, Zhou et al. (2013) compared electron density and ion density when ARTEMIS detected similar energy-time profiles as Kaguya (lower energy from the solar wind or lobe plasma and the thermal component does not exist) during high flux periods, and found that the calculated ion density (assuming protons) is 5 times higher than the electron density most of the time. This suggests that a significant fraction of the ions can possibly be heavy ions.

2.4.4 Magnetospheric Observation of Possible Moon-Origin Ions

Thus, the very heavy ions of the lunar origin (sputtered ions and neutrals from the surface or ionized exospheric neutrals) constantly exist in the “lunar ion wake” (downstream plasma region of the Moon where pickup heavy ions may reach, and is wider than the lunar wake in the flow dynamical meaning due to the finite gyroradius of heavy ions). The generated heavy ions are accelerated by the solar wind convection electric field and are finally picked up, with their flux varying depending on the solar wind conditions. The question is then how much these ions contribute to the metallic ions in the magnetosphere, such as those detected by Geotail/STICS (see Fig. 3). Here, we dismiss the case when the Moon is located in the Earth’s magnetotail because we do not expect the Moon-origin ions to return to the Earth against the strong anti-sunward plasma flow at the Moon location, as is confirmed by Geotail/STICS (Christon et al. 2020).

Therefore, we consider the case when the Moon is located upstream of the Earth, or more precisely, when the magnetosphere is within the “lunar ion wake” (downstream plasma region of the Moon where pickup heavy ions may reach, and is wider than the lunar wake in the flow dynamical meaning due to the finite gyroradius of heavy ions). Then, the $\sim 60 R_E$ distance from the Earth is enough for these pickup ions to gain the solar wind speed even for Fe⁺ with its large gyroradius as summarized in Table 3, reaching to nearly 100 keV (for

600 km/s speed) for Fe^+ . Considering further energization in the bow shock and magnetosheath, the other metallic ions with less mass may also reach the energy detectable by the Geotail/STICS and Wind/STICS instruments.

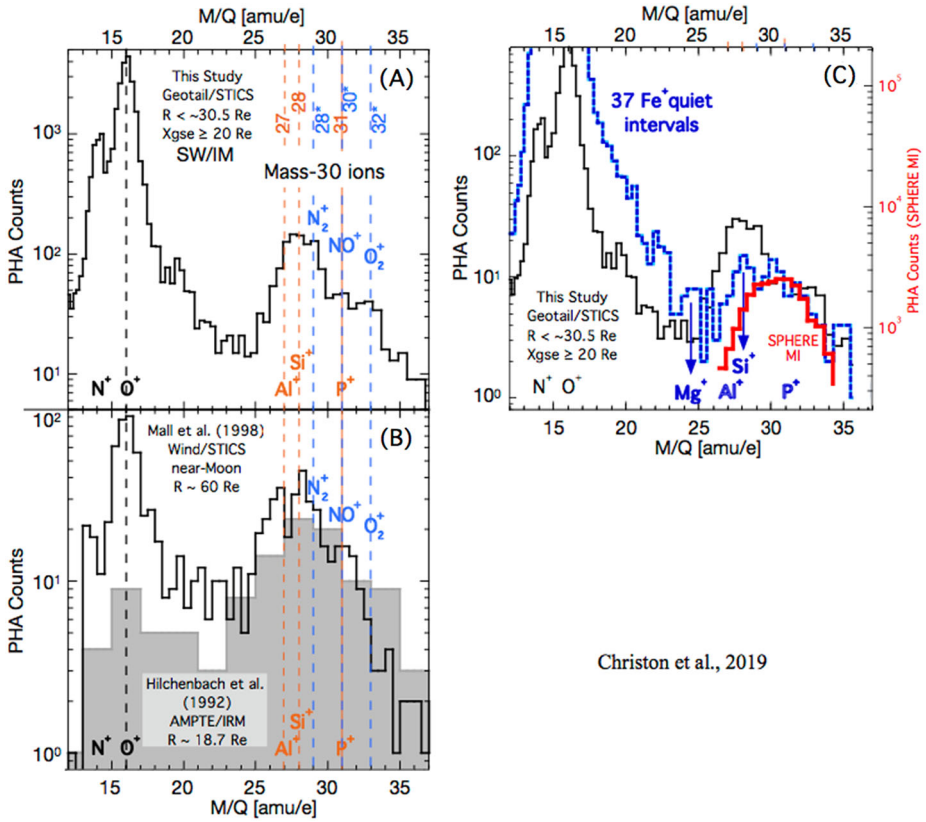
Metallic ions that are consistent with the Moon-origin ions (also consistent with Earth's origin from the metal layer) are actually detected upstream of the Earth. With the STICS instrument on the WIND spacecraft, low charge-state heavy metallic ions were observed during flybys on the earthwards side of the Moon as close as 17 lunar radii well in front of the Earth's bow shock (Mall et al. 1998). The ion composition measurements in the energy range of 20–200 keV/q show O^+ , Al^+ , and Si^+ ions and heavier ions. The Active Magnetospheric Particle Tracer Explorers (AMPTE) SULEICA instrument detected ions in the m/q range of 23–37 were observed in the solar wind upstream of the Earth's bow shock (Hilchenbach et al. 1993), with ion fluxes of at least $0.3 \text{ cm}^{-2} \text{ sec}^{-1} \text{ sr}^{-1} \text{ keV}^{-1}$ in the energy range of 5 keV/q to 230 keV/q.

Figure 12 summarizes these upstream observations (by Wind/STICS and AMPTE/SULEICA) and compared with the Geotail/STICS observation. Although the Geotail/STICS count rate of these low charge-state metallic ions is, including all sources, normally 0–1 count/day, the operating lifespan of more than 20 years and its $\sim 9 R_E \times \sim 30 R_E$ orbit allowed statistical studies of near-Earth heavy ions in the magnetosphere, the magnetosheath, and the solar wind sunward of Earth. In Fig. 12 (see Christon et al. 2020), the peak mass around $m/q \approx 30$ is substantially different between the upstream data (black trace in (C), around mass 27–28: Al^+ and Si^+) and magnetospheric data (red trace in (C), around mass 30–32: NO^+ and O_2^+). Unlike the magnetospheric peak that is dominated by the molecular ions (N_2^+ , NO^+ , O_2^+), the upstream peak is centered at Al^+ and Si^+ (slightly lower mass than molecular ions) in good agreement with mass spectra observed by Kaguya and LADEE (Saito et al. 2010; Halekas et al. 2015) as described in Sect. 2.4.

However, the existence of low charge-state heavy ions does not necessarily mean that the excess part of upstream counts beyond the magnetospheric profile ($m/q = 22$ –30) is of lunar origin because of the following reasons. (1) In addition to N_2^+ and CO^+ ($m/q = 28$), metallic ions at this mass range ($m/q = 22$ –30) exist in the Earth's upper atmosphere (Na^+ (23), Mg^+ (24), Al^+ (27), and Si^+ (28)) through the ablation of meteoroids (Plane et al. 2015) that form the mesospheric and thermospheric metal layer, as described in Sect. 2.3. (2) Their large gyroradii makes it possible to access the far upstream region by the foreshock (Kronberg et al. 2011) once they reach the space, although lifting these very species to the exobase is extremely difficult (Schunk and Nagy 2009). (3) The solar wind may also contain low charge-state heavy ions through the solar wind interaction with cometary microscopic dust. Thus, the mass profiles cannot be used to select the lunar ions detected even in the solar wind upstream of Earth (Christon et al. 2020). We come back this problem in §4.1.

3 List of Satellite Datasets and Models for Molecular and Metallic Ions

As summarized in Sect. 2, observations of molecular and metallic ions and modelling of their transport are important from many inter-disciplinary aspects. However, these very minor ions are vastly unexplored in the near-Earth space. This is because only a few terrestrial missions have been equipped with dedicated instrumentation capable of separating these molecular and metallic ions, and because even these few dedicated instruments were capable of detecting a limited energy range (cold ions of $< 50 \text{ eV}$ and energetic ions of $\sim 100 \text{ keV}$)



Christon et al., 2019

Fig. 12 Histograms of ion pulse height analysis (PHAs) events ordered by m/q with the ion species N^+ , O^+ , and ions around mass 30. (A) Geotail/STICS data ($\sim 87\text{--}212$ keV/q) at farthest upstream ($X_{GSE} = 20\text{--}30.5 R_E$). (B) Solid line: Wind/STICS data ($\sim 20\text{--}200$ keV/q) near the Moon at > 17 lunar radii when Wind is at sunward of the Earth (Mall et al. 1998), and shaded area: AMPTE-IRM data ($80\text{--}226$ keV/q) upstream of the bow shock at $18.7 R_E$ from (Hilchenbach et al. 1993). Vertical orange dashed lines, which pass through the peaks of solid lines (both Geotail and Wind data), correspond to the masses for light metallic ions of lunar origin: 27 (Al^+) and/or 28 (Si^+), and 31 (P^+) and/or 32 (S^+). As reference, mass lines for molecular ions ($N_2^+ = 28$, $NO^+ = 30$, $O_2^+ = 32$) are shown by vertical blue dashed lines and mass line for O^+ is shown with black dashed line. Geotail data were obtained over approximately 2 full solar cycles, Wind data were obtained during tail traversals over 1995–1997 (solar minimum), and AMPTE data were obtained over 3 months in late-1985 (solar minimum). (C) Geotail/STICS data at, black line: farthest upstream (the same as (A)); red line: the overall magnetosphere data (SPHERE in Fig. 1) which is dominated by molecular ions; and blue line: the average of 37 orbits (data over 24 hr covering all regions) during low to moderate solar/geomagnetic condition. The data are translated vertically to match values at $\geq 30 - 32$ amu/e. Image reproduced with permission from Christon et al. (2020), copyright by AGU

and a limited mass range (≤ 40 amu). Nevertheless, existing data from the past and on-going missions, including those not designed for the required mass separation, are sometimes capable of detecting some of these molecular (very limited for metallic) ions with available tools, although severe limitations exist (sensitivity and energy range, in addition to mass resolution and mass range). In this section, we list these datasets.

3.1 Satellite Datasets

Table 7 summarizes the available datasets from the magnetospheric and Moon missions by which the heavy molecular or metallic ions are actually observed and reported. As a reference, we also list the capability of planetary missions with the Earth flyby data in Table 8. The table includes the measurement methods because they determine the approximate resolution, sensitivity, and mass-energy ranges. There are roughly three different methods of mass separation for particle instruments: magnetic method, time-of-flight (TOF) method in various formats, and retarding potential analyzer (RPA) method. By combining with the electrostatic analyzer for energy per charge (E/q) selection at the entry of the instrument (by using a perpendicular electric field, only ions with specific energy per charge can follow the curved entry), the magnetic method and the TOF method give m/q and E/q , respectively.

The TOF method has many variants: foil-type for energetic particles (e.g. Wilken et al. 2001), combination of an electrostatic analyzer with a foil-type TOF unit (e.g. Rème et al. 2001), combination of an electrostatic analyzer with a linear electric field embedded TOF, so called LEF-reflectron unit (e.g. Delcourt et al. 2016; Föhn et al. 2021), combination of an electrostatic analyser with a grazing incidence microchannelplate (MCP) TOF (e.g. Devoto et al. 2008), combination of an electrostatic analyser with a gated TOF unit (e.g. Keller et al. 1999), combination of an electrostatic analyser with a reflecting surface TOF unit (Wittmann 2022), and straight start-end pair for a simple TOF. For hot plasma observations in the 0.05–10 keV energy range, the LEF-reflectron used in the MSA instrument onboard BepiColombo Mio (pre-launch name Mercury Magnetospheric Orbiter (MMO)) (Delcourt et al. 2016) so far provided the highest mass resolution $m/\Delta m$ up to > 40 for < 13 keV, with successful result by Kaguya/IMA ($m/\Delta m \sim 15$) as shown in Fig. 11. Further details about different measurement methods can be found in a review paper (Wüest et al. 2007). As a general problem with the TOF method using a start foil or a start surface, some molecular ions are dissociated into atomic ions and atoms there, causing the TOF spill out toward longer TOF from the molecular ion peak. This is why the Kaguya data do not include molecular ions. Nevertheless, the TOF technique is recognized as the most reliable method to separate different species.

Separation of species within the same mass group (between C, N, and O; between N_2 , CO, NO, and O_2) is another important challenge (particularly separation of N and O), because it requires about $m/\Delta m > 50$ (we call instruments with such capability as mass spectrometer), apart from the dissociation problem mentioned below. The same or even better mass resolution is required for the detection of metallic ions because of the much lower flux compared to the molecular ions.

As summarized in Table 1, there is a clear lack of mass spectrometers covering molecular and metallic ions for < 10 keV for near-Earth missions. However, mass spectrometers are regularly included in many deep-space missions, the Moon missions, and solar wind monitoring spacecrafts (like ACE: advanced composition explorer). Among them, Earth-flyby data exist for some mission such as STEREO. The Earth-flyby itself occurred for more missions such as BepiColombo (MPO and Mio), Solar Orbiter, MAVEN, and Rosetta, but heavy ion data were not taken or not useful.

Although excluded from Table 7, heavy molecular ions (O_2^+) might be able to be separated from the atomic ions (O^+) by a simple electrostatic analyzer when ions are streaming with a group velocity, such as the far downstream of the Earth. In such cases, different masses correspond to different kinetic energies, and hence the different ion species appear as different groups in an energy-time spectrogram. SOHO/CELIAS (in the Venus magnetotail at 0.3 au) detected heavy ions of Venus tail origin, and well separated C^+ and O^+

Table 7 Terrestrial missions that reported heavy molecular or metallic ions since 1980s

mission/instrument (duration) @ where	method	Specification ^(*)	what was actually observed	reference (spec + obs m>26)
Cluster/CIS (2001-) @magnetosphere (almost everywhere)	TOF (for > 28 eV) RPA (for low-energy)	0.7 eV/q – 40 keV/q m/q: 1–16 (H ⁺ , He ⁺⁺ , He ⁺ O ⁺)	1 – 40 amu/q (~50 lower statistics) m/Δm ~ 5–7	Rème et al. 2001. Kistler et al. 2013.
Cluster/RAPID (2001-) @magnetosphere (almost everywhere)	SSD TOF	> 400 keV H, He, and O (C, N, O are not separated)	m > 16 up to more than 60	Wilken et al. 2001. Haaland et al. 2020, 2021.
e-POP/IRMS (2013–2021) @325–1500 km altitude	TOF	< 70 eV/q m/q: 1–64	N ⁺ and O ⁺ are separated but not between N ₂ ⁺ , NO ⁺ , and O ₂ ⁺	Yau and James 2015, Yau and Howarth 2016.
Arase/LEPI (2017–present) @Inner magnetosphere	TOF	0.01–25 keV/q m/q: 1–40	H ⁺ , He ⁺⁺ , He ⁺ , O ⁺⁺ , O ⁺ , O ₂ ⁺ (no separation between N and O) m/Δm ~ 2–4	Asamura et al. 2018. Seki et al. 2019. (statistics)
Arase/MEPI (2017–present) @Inner magnetosphere	SSD TOF	7–87 keV/q m/q: 1–48	H ⁺ , He ⁺⁺ , He ⁺ , O ⁺⁺ , O ⁺ , O ₂ ⁺ (no separation between N and O) Observed m/Δm ~ 3~5	Yokota et al. 2017. Seki et al. 2019. (statistics)
Kaguya/MAP-PACE/IMA (2008–2010) @Moon	LEF-reflectron	10 eV/q – 28 keV/q m/q: 1 – ~60 m/Δm ~ 5 (m/Δm ~ 15 for < 12 keVq)	Separated Na ⁺ , Ca ⁺ , K ⁺ , C ⁺ , Si ⁺ , O ⁺ no molecular ions (due to start foil breaks molecules)	Saito et al. 2010 Yokota et al. 2009.
Geotail/STICS (1992–2022) @magnetosphere	SSD TOF	energy > 200 keV/q for m = 30 m: < 1 up to ~60–70 amu m/q: < 1 up to ~95 amu	Separated Fe ⁺ but ≪ 10 ⁻² counts/hr	Christon et al. 2017.
Wind/STICS (1994-) @magnetotail	SSD TOF	6–230 keV/q otherwise, the same design as Geotail.	Separated O ⁺ from Al ⁺ , Si ⁺	Mall et al. 1998.

Table 7 (Continued)

mission/instrument (duration) @ where	method	Specification ^(*)	what was actually observed	reference (spec + obs m>26)
Polar/TIDE (1996–2008) @below 8 RE	TOF	0.1–500 eV/q 1–40 amu/q m/Δm = 4	“Significant component of molecular ions in polar wind flux in response to CME”	Moore et al. 1995.
Polar/TIMAS (1996–2008) @below 8 RE	Magnet (double focusing)	15 eV/q – 33 keV/q m: 1 – >32 amu/q m/Δm = 2–5	Separated O ₂ ⁺ from O ⁺ (but not between N ₂ ⁺ , NO ⁺ , and O ₂ ⁺)	Shelley et al. 1995. Lennartsson et al. 2000.
Akebono/SMS (1989–2002) @up to 10000 km	RPA	< 50 eV/q m/q: 1–40	Mostly <20 eV Sometimes separate among N ₂ ⁺ , NO ⁺ , and O ₂ ⁺	Whalen et al. 1990. Yau et al. 1993; Yau et al. 1998.
AMPTE/CHEM (1984–1989) @Inner magnetosphere	TOF	1–300 keV/q m: <1 up to 90 m/q: <1, 74	Can separate N ₂ ⁺ , NO ⁺ , and O ₂ ⁺	Gloeckler and Hamilton 1987.
AMPTE/SULEICA (1984–1986) @Inner magnetosphere	TOF		Detected metallic ions (SW charge state)	Stern 1999. Hilchenbach 2004.
DE-1/RIMS (1981–1984) @568 km × 4.6 RE	RPA	< 50 eV/q m/q: 1– more than 32	Can separate N ₂ ⁺ , NO ⁺ , and O ₂ ⁺	Chappell et al. 1981. Craven et al. 1985.
DE-1/EICS (1981–1991) @568 km × 4.6 RE	Magnet	10 eV/q – 17 keV/q m/q = 1–150 m/Δm ~10	O ₂ ⁺ , NO ⁺ , N ₂ ⁺ separated (in ‘drum mode’)	Shelley et al. 1981.
MMS/HPCA (2015–present) @Magnetosphere	TOF	1 eV – 40 keV m/q: 1 – > 16 ^(*) m/Δm = 4~8	Fe ⁶⁺⁷⁺ by chance but not by search Routinely sample up to m/q = 1–~50 ^(*)	Young et al. 2016. Gomez et al. 2019. Bingham et al. 2021.

(*)Energy is with respect to spacecraft potential

(**)Although the TOF is capable of covering up to m/q ~50, the analyses is so far limited to m/q ≤16

Table 8 Planetary missions capable of separating metallic ions and molecular ions of < 100 keV

mission/instrument with Earth flyby data	metallic ions	molecular ions from atomic ions	Earth flyby?	reference
STEREO/PLASTIC	TOF	0.2–80 keV up to Fe	molecular @ Tail 200–300 R _E (2007)	Galvin et al. 2008. Kistler et al. 2010a.
Cassini/MIMI-CHEMS	TOF	~10–220 keV m: 1–80	only ring current ions @ ring current (1999)	Christon et al. 2017.
JUICE/JDC (Launched 2023)	TOF	1 eV – 35 keV m: 1–70 m/Δm = 30	Planned: 1 Moon (< 300 km) + 3 Earth (< 10,000 km) flybys	Wittmann 2022.
JUICE/NIM (Launched 2023)	LEF-reflection	< 10 eV (both neutrals + ions) m: 1–1000 m/Δm = 800	same as above	Föhn et al. 2021.

(Grünwaldt et al. 1997) by carbon-foil time-of-flight (C-TOF). This kind of rough mass separation has been tried for the ion instrument onboard ARTEMIS in the lunar orbit, when the Moon is within the terrestrial magnetotail and detects downstream ions of terrestrial origin. It allowed the separation of H^+ from heavy ions (Poppe et al. 2016a). However, the possible O_2^+ signature was not separated from the O^+ signature. To separate them, all ion species must be downstreaming with exactly the same velocity, but this hypothesis breaks down at large distances since heavy ions tend to reach higher flow velocities than protons (Seki et al. 1998).

3.2 Analyses Tools to Extract Molecular and Metallic Ions in the Space Missions

Table 9 summarizes the analyses tools of these data to extract the molecular and metallic ions. Note that some analyses tools might not be working with modern computer environments.

3.3 Mesospheric and Ionospheric Dataset Including Sounding Rocket

As the source region's information, datasets for the metal layers and ionospheric molecular ions are useful. Since they can be observed from the ground and sounding rocket in addition to some spaceborne observations (e.g., limb scanning), there are many databases, as summarized in Sect. 2.3.2. Table 10 summarizes observation methods with some examples. We just show examples for the databases because most of them are not publicly available or the database is not organized worldwide (no international database exists such as the networks for magnetometers and ionospheric HF radars).

3.4 Modelling of Contribution from Meteor and Space Debris Through Deposition to the Metal Layer

Table 11 summarizes models relevant to upflow of molecular and metallic ions reaching the exobase. The table also includes models of space debris as these could contribute to the mesospheric metal layer if their ablation altitudes are high enough. These models provide the distribution of the modeled species beyond what the empirical International Reference Ionosphere (IRI) model provides.

For the ionospheric and mesospheric heavy ions to be lifted, a common model of the neutral convection and electromagnetic fields to estimate the dynamics of the atomic ions can be used for both the molecular and metallic ions. Note that the available models still underestimate the upward convection in the polar region (see Shinagawa and Oyama 2006). Even the solar flare effect, i.e., the heating of the ionosphere by the flare-related radiation, cannot reproduce the extremely high convection that is observed (Yamauchi et al. 2020). Nevertheless, the existing models are a good start to estimate the upper limit and lower limit of the flux of metallic ions into the magnetosphere.

Since the ionospheric metal layer is most likely formed by the ablation of meteoroids, a current update to the ablation modeling is relevant. Then, we need a global circulation model with electrodynamic ion transport for lifting (expanding) metallic ions to high ionospheric altitudes (up to > 400 km) such that an ionospheric/thermospheric model of upflow can be applied. Finally, we note that it is difficult to model once the molecular and metallic ions reach the exobase, because wave activity is required to lift them to the region where sufficient energization is expected.

Table 9 Access method of relevant dataset and software with note on availability missions

mission /instrument	@where	database	notes on the software (basically request-basis)
Cluster/CIS	Magnetosphere	ESA Cluster Science Archive (ASCII) for routine product: https://csa.esac.esa.int/csa-web/ A separate telemetry product ("selected TOF events") for TOF.	IFSI TOF software (IDL source code): Reads level-1 binary files (selected TOF events).
Cluster/Rapid	Magnetosphere	ESA Cluster Science Archive (ASCII) for near-raw product: https://csa.esac.esa.int/csa-web/	Direct event (TOF) Reduced TOF
e-POP/IRM	325–1500 km altitude	ePOP-data.phys.ucalgary.ca	(software for general-user access under development)
Arase/LEPI	@ring current and inward	ERG science center (CDF file): https://ergsc.isee.nagoya-u.ac.jp/data_info/erg_shtml.en	(1) IDL SPEDAS for main data products, omcluding TOF histograms. (2) IDL code for MEPI to look at raw PHA data
Arase/MEPI			(1) C code by Y. Saito (read binary data) (2) IDL code Y. Harada
Kaguya/MAP- PACE IMA	Moon	SELENE data archive	
Wind/STICS	Magnetotail	NASA cdaweb (web interface) and pdf (CDF file) https://spdf.gsfc.nasa.gov/pub/data/wind/sms/l2/	
Polar/TIDE	Magnetosphere below 8 R _E	Level-Zero Telemetry Files hosted by the GSFC https://spdf.gsfc.nasa.gov/pub/data/polar/ https://pwgdata.gsfc.nasa.gov/pub/compressed/po/tid/	
Polar/TIMAS	Magnetosphere below 8 R _E	TIMAS H1 and H2 high resolution data: https://lasp.colorado.edu/timas/info/h12-data/h12-data.html Summary data: https://lasp.colorado.edu/timas/data/summary/	https://lasp.colorado.edu/timas/info/h12-data/make_h2.pro https://lasp.colorado.edu/timas/info/h12-data/make_h2_cdf.pro code developed by S. Nylund and S. Christon
Geotail/STICS	Outer magnetosphere	Summary plots available at http://sd-www.jhuapl.edu/Geotail/Years_dir.html	
Akebono/SMS	Magnetosphere below 10000 km	JAXA/ISAS Data Archives and Transmission System (DARTS): https://darts.isas.jaxa.jp/stp/akebono/SMS.html	under conversion to public database

Table 9 (Continued)

mission /instrument	@where	database	notes on the software (basically request-basis)
AMPTE/CHEM	Inner magnetosphere	<p>APL AMPTE site: http://sd-www.jhuapl.edu/AMPTE/chem/index.html</p> <p>NASA spdf site: https://spdf.gsfc.nasa.gov/pub/data/amppte/cc/</p>	<p>(1) Python code at UNH reading the CHEM FITS files</p> <p>(2) PHAFLUX fortran code calculates fluxes from PHA events</p>
AMPTE/SULEICA	Inner magnetosphere	Data is not easy to access	summary spectra
DE-1/RIMS	Inner magnetosphere	NASA spdf site: https://spdf.gsfc.nasa.gov/pub/data/de/1/plasma_rims/	https://spdf.gsfc.nasa.gov/pub/data/de/1/plasma_rims/de1_rims_summary-spectrograms_nasa-tm-19950009193.pdf
DE-1/EICS	Inner magnetosphere	NASA spdf site: https://spdf.gsfc.nasa.gov/pub/data/de/1/particles_eics/	
MMS/HPCA	equatorial magnetosphere	NASA cdfweb and spdf site: https://spdf.gsfc.nasa.gov/pub/data/mms/mms1/hpca/srvy/l2/tof-counts/ https://spdf.gsfc.nasa.gov/pub/data/mms/mms2/hpca/srvy/l2/tof-counts/ so on	TOF at NASA cdfweb https://cdaweb.gsfc.nasa.gov/cgi-bin/eval1.cgi

Table 10 Available method of monitoring the uplift of the molecular and metallic ions in the ionosphere and mesosphere

method	where	examples	species	data availability
Resonance-Scattering Lidar	Mainly mesosphere–80 km sometimes up to 200 km (only sometimes Na)	ALOMAR ^{*1} Tromsø for Na ^{*2}	Fe, Na, Ni, K, Ca, Ca ⁺ (Mg cannot be observed at 285 nm because of the stratospheric ozone layer) Na from 2010–2019 at Tromsø	Plane et al. 2015. CEDAW database (http://cedar.openmadrigal.org/) has list but no “open” data site. Data (Na) at Tromsø upon request
ion mass spectrometer (sounding rocket)	Mainly E-layer below 120 km	total < 10 for metallic ions ^{*3}	All major ions, but relatively few sounding rocket measurements compared to lidar	Kopp (1997). Grebowsky and Aikin (2002).
ion/neutral mass spectrometer (satellite)	< 30° lat and < 400 km alt	Ogo 6, AE-C, AE-D,	Molecular results are already included in standard model	
Satellite: limb optical	< 400 km alt	Odin, Envisat	Mg ⁺ , Mg, Na and K	On request to University of Leeds (W. Feng).

^{*1}<https://www.iap-kborn.de/en/research/departement-optical-soundings-and-sounding-rockets/instruments-and-models/metal-lidar-kuehlungsborn/>

^{*2}<https://www.isee.nagoya-u.ac.jp/~nozawa/indexlidarata.html>

^{*3}One example from molecular detection, one example from metallic detection, and example of obtaining extra information from Lidar observation of > 130 km

Table 11 Models relevant to upflow of molecular and metallic ions reaching the exobase

Name	Description	Citation/availability
SAMI-3	Predict metallic ion in the ionosphere (Huba's model includes transport to 600 km)	Feng et al. 2013; Wu et al. 2021.
WACCM	Metallic ions in the ionosphere.	Bones et al. 2019; Vondrak et al. 2008; Carrillo-Sánchez et al. 2020.
CABMOD	Examine differential ablation of meteoroids and deposition as a function of altitude and orbital position	Data available on request ^{*1} .
WACCM-X	Numerical model spanning the range of altitude from the Earth's surface to the upper thermosphere.	Wu et al. 2021. www2.hao.ucar.edu/modeling/waccm-x
ORSAT	Predict the re-entry survivability of satellite and launch vehicle upper stage components.	Dobarco-Otero et al. 2005. orbitaldebris.jsc.nasa.gov/reentry/orsat.html
SCARAB	Simulate the re-entry of a satellite in detail.	Koppenwallner et al. 2005. www.htg-gmbh.com/en/htg-gmbh/software/scarab/
MASTER	Assess the debris or meteoroid flux imparted on a spacecraft on an arbitrary earth orbit.	Flegel et al. 2009. sdup.esoc.esa.int/
LEGEND	Three-dimensional debris evolutionary model for long-term debris environment projection.	Liou et al. 2004. orbitaldebris.jsc.nasa.gov/modeling/legend.html
-	A dynamical model of the sporadic meteoroid complex.	Wiegert et al. 2009.
-	Fluid model (simulation) in the ionosphere	Shinagawa and Oyama 2006.
-	Polar wind outflow model for < 300 km up to > 8000 km	Gloeger A (GFSC/Mishigan).

^{*1}Request to Juan Diego Carrillo Sanchez (juandiego.carrillosanchez@nasa.gov)

4 Merit of Combining Data from Different Sources and Models

In this section, we show some examples of the merit of combining data and knowledge from different sources.

4.1 Moon Contribution to Energetic (> 100 keV) Ions

As summarized in Sect. 2.4, the mass spectrum of the very heavy ions in the Earth's upstream region while downstream of the Moon is consistent with that coming from the Moon. However, this is yet not sufficient to state that the majority are of lunar origin, as discussed in Sect. 2.4.4. We revisit this problem by combining the Geotail/STICS observations with other data such as the Moon location and solar wind plasma measurements.

4.1.1 Statistics of Energetic Ions (Geotail)

Christon et al. (2020) examined the Geotail/STICS counts in relation to the Moon location. To overcome the low count-rate problem (0–1 count per day), they integrated Geotail data over nearly 20 years, and further integrated the data over the location for both the Geotail (four regions which are the same as Fig. 3) and the Moon (six locations: the upstream near the new Moon, four sides, and the downstream near full Moon). Figure 13 shows the results. For example, sector 3 in Fig. 13a shows the result of collecting all cases when the Moon is located sunward of Geotail's nominal orbital X_{GSE} – Y_{GSE} range.

Figures 13b and 13c (Christon et al. 2020, Fig. 7) show the results for high K_p (≥ 3) and low K_p (≤ 2) cases, respectively. For both K_p cases, heavy ion counts (for $m/q \geq 28$, i.e., molecular, metallic ions) in the upstream solar wind (SW/IM in Fig. 13) show a peak at LLT sector 3 (5-day period near the new Moon), with a widening of the peak for higher K_p . This peak at LLT sector 3 is less obvious for the magnetosheath (SHEATH in Fig. 13) and there is nearly no peak at sector 3 in the magnetosphere (SPHERE in Fig. 13) and plasma lobe (LOBE in Fig. 13). Considering that heavy ion flux of $m/q \geq 28$ escaping from the Earth (almost all are molecular ion) is nearly zero for low K_p , all these results indicate that Moon origin metallic ions are the major heavy ($m/q > 20$) ions in the upstream region. Here, the increase of the ion counts for high K_p (which generally means stronger solar wind) agrees with the general increase of both the Earth-origin molecular ion flux (not dependent on the Moon location, and seen in all panels) and the Moon origin heavy ion flux (peak at LLT sector 3).

The results also indicate that unless the Moon is directly upstream of the Earth (i.e., except LLT sector 3), the magnetospheric heavy ($m/q > 20$: metallic) ions are mainly provided from the Earth with minor contribution from the Moon most of the time. Both contributions can be comparable if we limit to a 5-day average near new Moons because the peak values for $m/q > 20$ ions near LLT sector 3 are the same level between in the upstream (SW/IM and SHEATH) and in the magnetosphere (SPHERE).

4.1.2 Case Studies (Combining Geotail and ACE)

To obtain a more concrete view of the Moon-origin ions in the magnetosphere with the existing dataset of very low count rates (0–1 count per day for singly charged metallic ions of mass larger than 33), we need to carefully select the conditions when the solar wind flux significantly increased while the Moon was upstream. Here we show the usefulness of

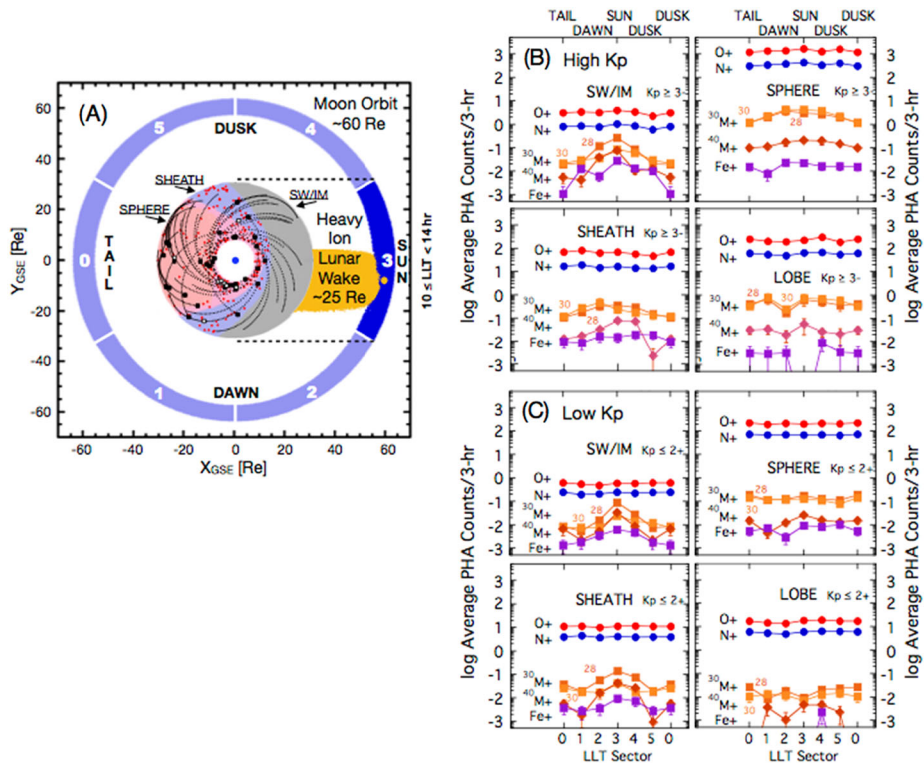


Fig. 13 (A) A sketch of the Earth (blue dot at the center), the Moon’s orbital range ($\sim 60 R_E$), and Geotail orbital range ($\sim 9 < R < 35 R_E$). Two spatial criteria for considering possible lunar pickup ion influence in Geotail/STICS suprathermal ($\sim 87\text{--}212$ keV/e) ion measurements are the lunar local time (LLT) and the “Lunar-ion Wake”. LLT marks the orbital location of the Moon with respect to the Earth-Sun line. For example, 10 hours \leq LLT \leq 14 hours (the sector marked as 3 in the figure) corresponds to the Moon location sunward of Geotail’s nominal orbital $X_{GSE}\text{--}Y_{GSE}$ range. The “Lunar-ion Wake” (different from fluid dynamical “wake”) drawn here ($\sim 25 R_E$ width) is the region where very heavy ions of lunar origin (e.g., CO^{2+} or Fe^+) are expected exist in the nominal IMF at 1 au ($\sim 7\text{--}9$ nT). Selected segments of Geotail orbits (dotted traces near Earth) terminate when an Fe^+ was observed during low to moderate solar and geomagnetic conditions. White (black) squares indicate Fe^+ observations obtained when the Moon was (not) in LLT-sector 3. Red dots show other measured Fe^+ data. Three different regions (magnetosphere: “SPHERE”, magnetosheath: SHEATH”, and upstream of bow shock “SW/IM”) are identified by different colours. The plasma lobe (“LOBE in Fig. 1) overlies the SPHERE and not shown here. (B) Average counts/3-hours of low charge state ions at four different regions during $K_p \geq 3$ and (C) those during $K_p \leq 2$. Image reproduced with permission from Christon et al. (2020), copyright by AGU.

combining different datasets (Geotail, ACE, and SOHO) for such a study. We selected CME-driven interplanetary shock events (from the list of events identified by the SOHO/CELIAS proton monitor) with significant flux increase of iron ion (Fe^{n+}) by three orders of magnitude (to over $100 \text{ cm}^{-2} \text{ s}^{-1} \text{ str}^{-1} \text{ MeV}^{-1}$) in the ACE/ULEIS instrument within two days of a new Moon. Out of these events, half-day resolution QL of Geotail/STICS is available for 10 events: 6 events when Geotail is located within the lunar wake, and 4 events outside the lunar wake.

For these “best” events, we counted all half-day counts when the interplanetary shock arrived and compared them with those when Geotail was in the same region one orbit before (about 5 days before). Here, the region is judged from the orbit, low-energy particle (LEP)

Table 12 Change in the half-day integrated counts of low charge-state metallic ions observed by Geotail/STICS

shock timing	location ^{*3}	triple: $m > 34$	double: $m/q \geq 39$ –46
2000-04-06, 16:01	SH	0 to 1 (0 to 2)	0 to 41
2000-11-26, 07:15	SW	0 to 0 (0 to 0)	0–1 to 3
2002-09-07, 15:54	SW	0 to 1 (0 to 0)	0 to 7
2003-05-29, 11:52	SH	0 to 4 (0 to 0)	2 to 42
2004-01-22, 01:10	SH to SPH	0 to 11 (1 to 8)	201 to 463
2005-09-02 ^{*1} , 13:32	SW	0 to 0 (0 to 0)	0 to 0
2000-10-28, 09:01	SW ^{*4}	0 to 2 (0 to 0)	2–4 to 2–3
2001-01-23, 10:15	SPH ^{*4}	0 to 0 (0 to 0)	243 to 193
2003-10-24 ^{*2} , 14:47	SW ^{*4}	0 to 0 (0 to 0)	0 to 0
2004-09-13, 19:29	SW ^{*4}	0 to 0 (0 to 0)	0–1 to 1–3

^{*1}Peak of Aurigids meteor shower was 2005-08-31

^{*2}Peak of Orionids meteor shower was 2003-10-21

^{*3}SH: magnetosheath, SW: solar wind, SPH magnetosphere

^{*4}Geotail was not in the wake region for this time interval

data and STICS data. Table 12 summarizes the results. The third column lists the change in the half-day triple-coincidence counts for $m > 34$ and $m/q \geq 34$ (inside parenthesis are additional counts that satisfies $m > 20$ and $m/q \geq 34$). For all cases, counts during one orbit before the CME arrival (5 days before, i.e., Geotail was outside the lunar wake) were zero. However, after the arrival of the interplanetary shock, Geotail sometimes detected counts corresponding to the metallic ions apparently heavier than O_2^+ if and only if Geotail was located within the lunar wake.

Since the majority of these cases were observed when Geotail was in the solar wind, the result is consistent with the hypothesis that low charge-state heavy metallic ions in the upstream region seen in Fig. 3 are mostly from the Moon when the solar wind conditions were favorable for releasing particles from the lunar surface, by sputtering or charge exchange. This hypothesis is also supported by the double-coincidence counts for $m/q \geq 39$ during the same half-day periods (fourth column of Table 12). Here, we take $m/q \geq 39$ because its peak (corresponding to potassium ion K^+) is well separated from mass 32 (S^+ or P^+ rather than O_2^+ because it is most likely of lunar origin), as shown in Fig. 14.

Thus, just combining the available summary data from the Geotail/STICS and from the solar wind monitor (SOHO/CELIAS and ACE/ULEIS) can provide more insight into the metallic ions in the upstream region. Thus, it is worthwhile to try further combinations with the other datasets (e.g., geomagnetic activity) to examine, for example, the relative importance of the lunar origin compared to the Earth origin as the source for the magnetospheric metallic ions. Ideally, we need new observations using dedicated instruments with much higher sensitivity for high masses (see Sect. 5). This is particularly important for the magnetospheric metallic ions, because the ionosphere or mesosphere can also supply a significant amount of metallic ions to easily hide the lunar signal unless the external condition is specified to maximize the ratio of lunar origin ions to the Earth origin ions. For example, the total flux of the lunar origin ions might not be negligible when the Moon is upstream of the Earth and the geomagnetic activity is moderate or quiet.

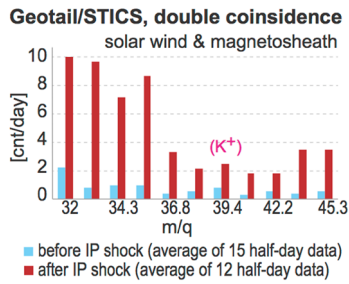


Fig. 14 Mass-per-charge (m/q) distribution of double coincidence counts for $m/q \geq 32$ ions obtained by Geotail/STICS. Half-day data inside the solar wind or magnetosheath before and after the interplanetary (IP) shocks with the highest Fe^{n+} fluxes listed in Table 12 (total 8 events) are averaged. For each event, a maximum of two half-days of data (if Geotail was staying long within the solar wind) are included. A small peak spread of the major peak at around $m/q = 39$ is discernible in addition to the board major peak from $m/q \approx 32$

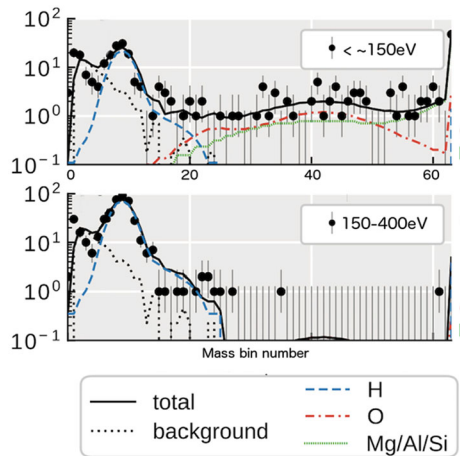
4.1.3 Low-Energy Ions Near the Moon (Kaguya or Change-4, Combining with ACE)

For the source environment near the Moon, it is again useful to compare the lunar ion flux leaving the Moon with the solar wind. With the capability of detecting these ions, Kaguya observed notable increase of the Moon-origin ions around the Moon when CIRs arrived at the Moon, as mentioned in Sect. 2.4.3. Unfortunately, the operation of Kaguya/IMA was only from 2008 to early 2009, i.e., during the lowest solar activity in the space age (deepest solar minimum), and only very few CIRs of minor intensity occurred. This is not easy because such a study requires a good constellation of Kaguya (the orbit plane with respect to the Moon-Earth line changes depending on the Earth's season), a magnetospheric satellite (in the magnetosphere and lunar wake) and the Moon (e.g., at few days before and after new Moons) during the CIR arrival. Probably for these reasons, we could not find a notable correlation between the Kaguya's surface-origin ion counts (time resolution of 1 day) and Cluster/CODIF data.

Other than CMEs or CIRs, the Moon is exposed to high upstream plasma energy in the Earth's plasma lobe and mantle region because of the high flux of terrestrial escaping O^+ (Slapak et al. 2017a, 2017b; Yamauchi 2019) when the Moon is in the magnetotail for about 5 days every month. For the Earth's plasma sheet, the Moon is exposed to hot (high energy) ions including terrestrial O^+ , but the Kaguya observations for such periods are too short for the sensitivity of IMA instrument to examine the expected increase of sputtering inside the plasma sheet.

Finally, the Chang'e-4 lunar rover is equipped with an ion/neutral instrument, the Advanced Small Analyzer for Neutrals: ASAN (Wieser et al. 2020a, 2024). ASAN is capable of separating the heavy species from proton/hydrogen as shown in Fig. 15, and is still operating after 5 years on the Moon surface since 2019. With the FOV directed toward the lunar surface, ASAN detect particles only from the lunar surface. Furthermore, ASAN can distinguish between the sputtering component and reflecting component based on energy analysis of the registered particles (Xie et al. 2021). Since its operation is in many short sessions of 10–20 min, total operation of AXAN is only several hours every month. On the other hand, long duration of the Chang'e-4 mission (> 5 years) allowed AXAN data covering the entire rising phase of solar cycle 25, and has already experienced several strong CMEs starting from the one in December 2020. The count rate is marginally sufficient to separate H^+ and other elements (O^+ and heavier together), but it is still useful to examine the increase of

Fig. 15 Energy-integrated mass spectrum of neutrals coming from the lunar surface observed by Chang'e4/ASAN during January - September 2019 (preliminary overview results). The colored curves are modelled values assuming specific species. Upper: energy < 150 eV is integrated. Lower: energy > 150–400 eV are integrated. Note that signals for high-mass elements (> 20) are contaminated by background noise. Courtesy of M. Wieser, presented at European Geoscience Union General Assembly in 2020 (Wieser et al. 2020b).



sputtering of heavy ions during the CME passage. Analysis is on-going. The proton channel analyses has recently performed in Wieser et al. (2024).

4.2 Ionospheric Origin of Low-Energy Heavy Molecular Ions (in-Situ Observations)

4.2.1 Recent Observations Above the Ionosphere

With the ability to measure low-energy ions up to ~ 100 eV, which is sufficient for measuring most ion upflow and outflow events in the full altitude range of the CASSIOPE (Swarm-E) satellite (perigee 325 km and initial apogee 1500 km), the e-POP/IRM instrument is capable of separating the heavy molecular ions from the N^+ and O^+ (Yau and James 2015; Yau and Howarth 2016) in the topside ionosphere. It covers both the high-latitude outflow region around the dayside cusp and the auroral and sub-auroral outflow region. In a preliminary study (Foss 2019; Foss et al., to be submitted 2024), upflow of the heavy molecular ion above the ionosphere are often detected on the equatorward side of the auroral ion outflow region, especially during geomagnetic active periods, in addition to in the dayside polar cap.

Figure 16 shows one example of the e-POP/IRM observation in the dayside at ~ 1400 km altitude when $K_p = 3$ and $Dst = -37$ nT during the recovery phase of a moderate geomagnetic storm on 29 August 2014 (Dst minimum -63 nT). The vertical axis is the time of arrival (TOA) at the detector which represents the TOF, and molecular ions correspond to TOA ~ 80 –100. Both the count and TOA increased during 08:00:55–08:01:25 UT, at which the spacecraft is in the dayside at around $\sim 72^\circ$ magnetic latitude and ~ 1400 km altitude. This means that the molecular ions appeared in addition to O^+ . Thus, e-POP can separate the heavy molecular ions from the atomic ions.

Figure 17 shows another example of the e-POP/IRM observation in the nightside at the altitude of 1360 km when $K_p = 6+$ and $Dst = -87$ nT during a major geomagnetic storm (Dst minimum -130 nT). Both the count and TOA suddenly increased at around 16:15:30 UT in the evening sub-auroral latitude (20.4 MLT, 53° Mlat) indicating a mixture of molecular ions and atomic ions, with continued high count in the TOA range corresponding to atomic ions. This example shows that, unlike Akebono observations at higher altitude, heavy molecular ions can reach the topside ionosphere in the nightside sub-auroral region, at the equatorward side of the atomic ion outflow region in the auroral region.

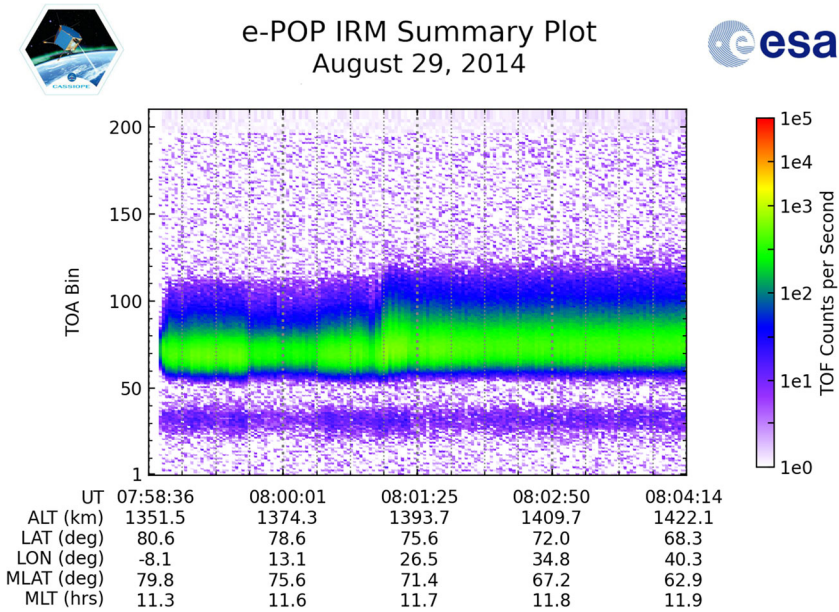


Fig. 16 TOF-time spectrogram of observed ion count rates on e-POP during the recovery phase of a magnetic storm on 29 August 2014. Vertical axis is time of arrival at detector (TOA) which represents the TOF, and molecular ions correspond to TOA \sim 80–100

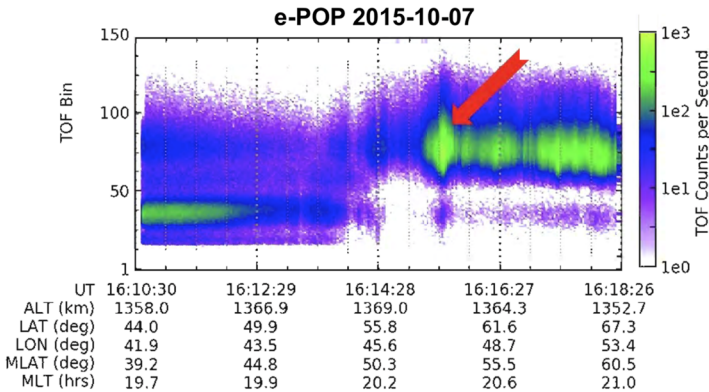


Fig. 17 Same as Fig. 16 but for on 7 October 2015. This traversal took place just before the lidar event mentioned in Sect. 4.3 later

Figure 18 shows the statistics of Statistical distributions of molecular ion detection observed by e-POP. The observed low- and mid-latitude events are predominantly low- or medium-flux events at low altitudes (< 800 km). We here note that the lowest-latitude ($< 10^\circ$ Mlat) events at 16–22 MLT are believed to be mostly associated with the Appleton anomaly and not part of the molecular ion upflow population. Otherwise, the other low-latitude detection of the molecular ions (particularly for < 800 km altitude) suggests that these molecular ions are convected equatorward in the ionosphere after originating at higher (auroral) latitudes. Thus, the ionospheric convection (both equatorward and upward) can

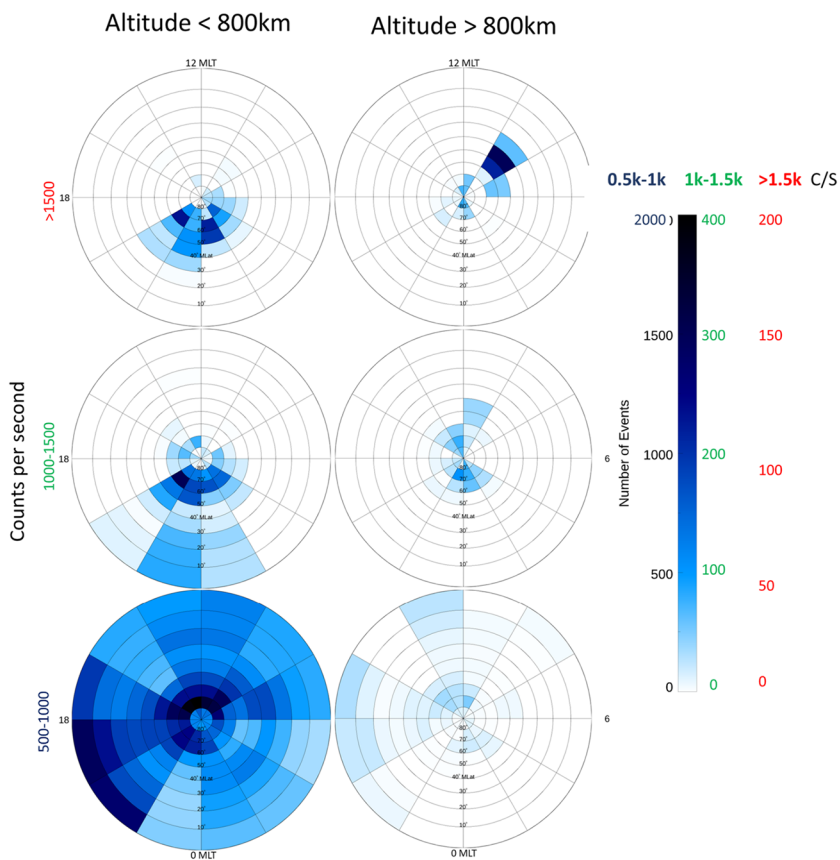


Fig. 18 Statistical distributions of molecular ion detection observed by e-POP as a function of magnetic local time (MLT) and magnetic latitude (Mlat) below (left) and above (right) 800 km altitude, respectively; top to bottom: peak count rate > 1500 , $= 1000\text{--}1500$, and $= 500\text{--}1000$ counts-per-second, respectively. (Courtesy of V. Foss, to be submitted 2024)

be strong enough to transport heavy molecular ions to very low latitudes before they reach the topside ionosphere or before they undergo dissociative recombination to form a pair of neutral atoms (see Sect. 2.2.2).

The detection of molecular ions on the nightside by e-POP at 1400 km answers one of the questions in Sect. 2.2: at which altitude do the molecular ion upflows begin to disappear in the nightside outflow region in which the atomic ion upflows are detected at much higher altitudes by Akebono and Polar? The difference in the observed ion upflows between molecular ions and atomic ions starts at about 1200 km altitude on the nightside. There are two possibilities for the cause of such difference between the molecular ions and atomic ions: insufficient pre-energization to reach the altitude at which the transverse ion energization starts (above 2000 km; Whalen et al. 1990, 1991), and the absence of main energization at the latitude of molecular ion formation and upflow.

For the first scenario, the pre-energization that is required above e-POP altitude for a molecular ion to reach 4000 km (2500 km) altitude must be less than 4 eV (2 eV) in the field-aligned direction, which is double (about the same as) the energy required from 500 km altitude to initial e-POP apogee (1500 km altitude) according to Table 4 in Sect. 2. For

the second scenario, energization of ions between the e-POP altitude and Akebono altitude including energization of all types must be less than 7 eV in the field-aligned direction. Neither of these two possibilities can be examined due to the lack of dedicated instruments for observing molecular ions in the magnetosphere.

4.2.2 Magnetospheric Molecular Ion Measurements by Non-optimized Instruments

There are instruments that are not optimized for separating molecular ions from atomic ions, but still able to identify them under certain conditions, particularly if the ion outflow is very strong. We here show an example from the Cluster/CODIF instrument.

The CODIF ion mass spectrometer onboard Cluster, with a mass resolution of $m/\Delta m \approx 5\text{--}7$ (Rème et al. 2001), was not designed to separate molecular NO-group ions and atomic CNO-group ions. Ions lose energy when going through the thin carbon foil in the instrument at the start of the time-of-flight section. Resultant lower energy (i.e., slower speed) means a longer time-of-flight before hitting the stop detector. This leads to a long tail in the time-of-flight distribution of heavy ions. Therefore, the time-of-flight peak of the heavy molecular ions on CODIF overlaps with the tail of the O^+ peak, making it difficult to separate the molecular ions. Usually, the molecular ion counts are negligible compared to the O^+ tail. Therefore, the molecular ion counts have not been counted.

However, during some strong events (e.g., Schillings et al. 2017), the flux of the molecular ions occasionally becomes high enough to have a separate peak above the oxygen tail in the TOF region where the molecular ion peak should appear (Dandouras et al., in preparation, 2024), as shown in Fig. 19. In such cases, the molecular ions can be distinguished. By fitting multiple peaks to the time-of-flight spectra, the abundance of molecular ions can also be estimated.

Figure 20 shows one Cluster pass through the inner magnetosphere and over the polar cap during the 2003 Halloween storm. The top three panels show the H^+ energy spectrum and the pitch angle distributions for two energy ranges. The next three panels show the same parameters for O^+ . Two clear spatial regions can be distinguished. From the beginning of the plot until $\sim 15:15$ UT, Cluster is in the closed field line region of the inner magnetosphere. After 15:15 UT, it is moving out over the polar cap, and observing a narrow distribution of O^+ ions that is convecting tailward, likely from the cusp region.

For ions flowing over the polar cap where solar wind electric field drives ion convection perpendicular to the magnetic field, the combination of the field-aligned upflow and this perpendicular convection leads to the “velocity filter effect”, in which the ions become spatially separated by their velocity (and hence energy). In Fig. 20, such a narrow energy-banded O^+ is seen after 15:10 UT. The pitch angles of these O^+ are 180° (nearly anti-parallel to the magnetic field), i.e., flowing outward from the Earth’s northern hemisphere. Such a spectrogram with narrow band O^+ is typically seen in the polar cap.

For this time period (after 15:10 UT), the time-of-flight (TOF) spectra of the CODIF data can be used to determine if molecular ions coexist with O^+ . Figure 21 shows a scatter plot of energy versus TOF for three time periods labeled in Fig. 20. During the first two time periods (16:00–16:30 UT and 16:35–16:50 UT) both in the morning sector in the polar cap, the low-energy O^+ ions are evident, with a peak at a TOF channel around 100, and a long tail towards higher TOF. But the O^+ peak is accompanied by a second track at higher energy and longer time-of-flight consistent with molecular ions. Such separation in energy of the outflowing ions is typically seen in the polar cap between H^+ and O^+ (e.g., Nilsson et al. 2006), and hence is attributed to the mass difference for Fig. 21, too. During the last

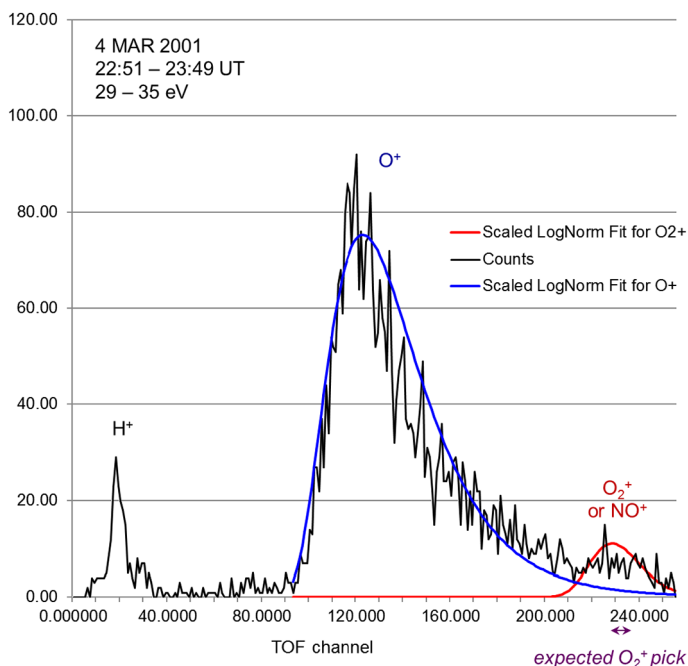


Fig. 19 Time-of-flight (TOF) histogram for the 29–35 eV ions detected by CODIF onboard Cluster on 4 March 2001 between 22:51 and 23:49 UT above the southern polar cap, while observing an upwelling ion beam. The blue and red curves represent the simulation results for atomic O^+ (blue curve) and fragments of molecular O_2^+ (red curve) ions entering the TOF section of the instrument, after their passage through the carbon foil where the molecular ions fragment (SRIM software simulation). The upwelling ion beam is dominated by the O^+ ions, but the instrument TOF data also show the existence of a weak O_2^+ (or NO^+) population

time period (17:15–18:00 UT, the midnight sector near the polar cap boundary), only the O^+ track is observed showing that the molecules from the dayside outflow are not reaching this location.

There are also low energy field-aligned ions observed during the inner magnetosphere perigee pass ($L < 5$). The pitch angles of O^+ at 30–300 eV, shown in the bottom panel of Fig. 20, have peaks close to either at 0 or 180 degrees. The field-aligned dominance indicates that these heavy ions directly come from the ionosphere, including those trapped and bouncing after outflowing from even lower latitude (Quinn and McIlwain 1979). In both cases, the source is at lower latitude than the ions seen in the polar cap (e.g., after 15:10 UT in Fig. 20). To evaluate the existence of molecular ions, we again examine the time-of-flight. Figure 22 shows the result for the ions at 30–200 eV during 13:15–14:10 UT (perigee pass at $L < 5$) where the low-energy field-aligned O^+ is observed. Here we show a histogram instead of a scatter plot. The expected TOF location of the molecular ions is marked with the red arrow in Fig. 22. A clear enhancement is observed there, indicating that molecular ions were outflowing not just in the cusp region, but in the lower latitude closed-field line region at $< 62\text{--}63^\circ$ Inv, as well, for this intense storm.

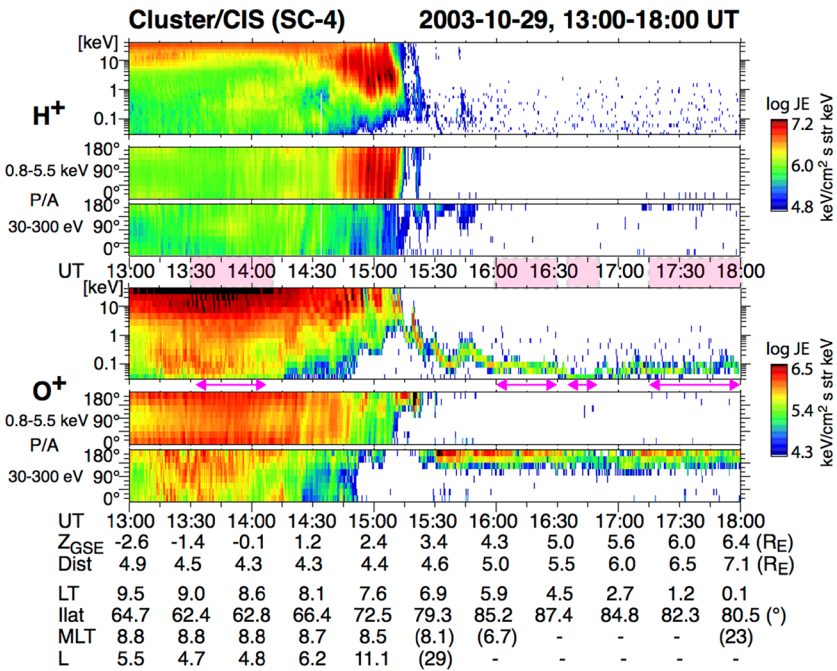


Fig. 20 Cluster CIS/CODIF observation of Halloween storm on 29 October 2003. Energy-time and pitch angle-time spectrograms for H⁺ (upper panels) and for heavy ions (labeled as O⁺) are displayed. The periods indicated by horizontal arrows and hatches correspond to periods when the time-of-flight distributions were obtained, as shown in Fig. 21 (16:00–16:30 UT, 16:35–16:50 UT, and 17:15–18:00 UT) and Fig. 22 (13:30–14:10 UT), respectively

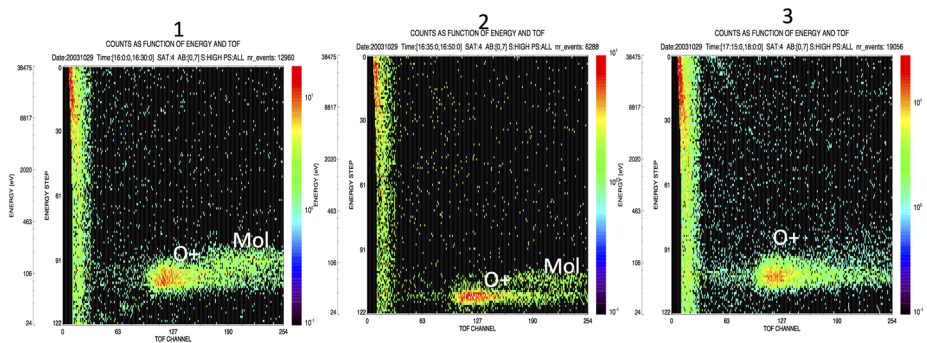


Fig. 21 Energy versus time-of-flight scatter plot of ion events measured by Cluster CIS/CODIF during the Halloween storm on 29 October 2003. (a) 16:00–16:30 UT, (b) 16:35–16:50 UT, and (c) 17:15–18:00 UT. These periods are indicated by horizontal arrows and hatches in Fig. 20. Horizontal axis is time-of-flight (TOF), which is inversely proportional to the velocity in the instrument. The vertical axis is ion energy (channel 80:~ 500 eV; channel 90:~ 200 eV; and channel 105:~ 90 eV)

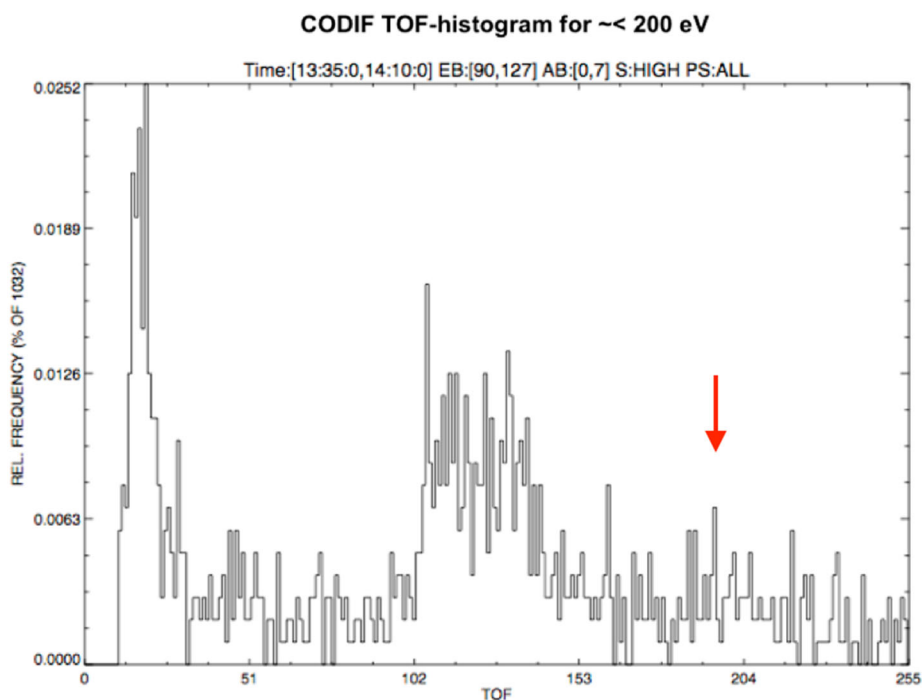


Fig. 22 Time-of-flight Histogram of ion events in the energy range 30–200 eV during 13:15–14:10 UT, where outflowing ions are observed. The vertical red arrow corresponds to the expected location of molecular ions ($m/q \sim 30$)

4.2.3 Ground-Based Data

To investigate the ion upflow, incoherent scatter (IS) radars such as EISCAT VHF and UHF radars have long been used to infer the extraordinary upward convection up to about 500 km altitude (e.g., Wahlund et al. 1992; Ogawa et al. 2019; Takada et al. 2021). However, these IS radar observations cannot separate the ion composition, and hence, one needs to assume certain composition ratios of H^+ , O^+ , and N_2^+ in order to estimate the heavy ion upflow from the IS radar data. Furthermore, for the actual ionospheric observations, the obtained maximum upward ion velocities are a few hundred m/s ($\sim 10^{-3}$ eV), which are negligible compared to the escape velocity (10¹ eV). Therefore, the upflow observation by these IS radars does not necessarily mean an upflow above the exobase, or, more importantly, must not be interpreted simply as the upflow of molecular ions at higher altitudes, as shown in Sect. 4.2.1 (a significant difference between high-altitude and low-altitude is observed by e-POP and Akebono). The heavy ion upflow at sub-auroral latitudes (where e-POP detected molecular ions with sufficient flux) needs sufficient additional energization (via wave-particle interactions, for example) to reach the magnetosphere. Such additional energy is not available normally at sub-auroral latitudes because of the lower electromagnetic activity than at the auroral latitudes.

Thus, using an IS radar to estimate the molecular ion motion is very misleading and is not recommended unless one makes a statistical study with the radar data and e-POP observation using many traversals. On the other hand, the EISCAT radars can monitor the

general upflow condition, allowing us to define the necessary conditions for molecular ions to reach the topside ionosphere, particularly for the dayside polar cap source.

4.3 Upper Atmospheric Source of Metallic Ions (Ground-Based Observation, Model)

4.3.1 Re-Visit of Fe^+

As discussed in Sect. 2.3, there are layers of neutral metal atoms in the atmosphere that appear globally between about 75 and 110 km as well as layers of ionized metal atoms between about 90 and 130 km (Plane 2003; Plane et al. 2015). As discussed in Sect. 2.3.3, these metallic ions in the lower part of the ionosphere can reach the exobase ionosphere where heavy molecular ions are detected because of the similar mass as these molecular ions. The same mass-argument applies to the energization process above the ionosphere; i.e., metallic ions that have arrived at the exobase should reach the magnetosphere. However, with a mass only twice the O_2^+ mass, Fe^+ (mass 56) was detected with only 350 counts by Geotail over 20 years, i.e., about 2 count per month (Christon et al. 2017). This count rates is far below the detection of the heavy molecular ions in the magnetosphere (Sect. 2.2). This low detection rate can set the boundary condition for ionospheric transport models for vertical ion transport, which are still under development (e.g., Shinagawa and Oyama 2006).

4.3.2 Lidar Observation Combining with Magnetospheric Patchy Data

As summarized in Sect. 2.3.2, metallic atoms and ions (Na, K, Fe, Ca, Ca^+ , Li and Ni) in the upper mesosphere and lower thermosphere are observed by lidars, sounding rockets, and satellites. If limited to low altitudes up to the mesosphere, the modern resonance lidar is able to make diurnal observations (Plane 2003). Even the vertical velocity can be measured (e.g., down to 1 cm s^{-1} resolution for Na atoms) between 80 and 105 km by Na lidar (Gardner et al. 2014). The vertical fluxes for other species can also be estimated by the other lidars co-locating on the same site (e.g., Fe lidar).

Although the altitude range for the lidar measurement covers only the lower part of the ionosphere, such monitoring helps qualitatively understanding the dynamics of metallic species during the ionospheric conditions that enhance the molecular ion upflow above the exobase because the required upward convection for such transport is common (“strong”) for both the metallic ions and heavy molecular ions, as mentioned in Sect. 2.3.3. In this sense, monitoring the dynamics of metal layers could be useful when the molecular ion upflow is observed by low-altitude satellites, although the existing technology allows meaningful measurement only for Na, K, Ca, Ca^+ and Fe. Any lidar data can potentially be compared with low-altitude satellite observations that are capable of separating heavy ion (mass > 20 amu) such as e-POP. For example, statistics of conjugate observations for better understanding of the dynamics of the metal species in the condition that molecular ion upflow is enhanced.

Here we take Na atom observations as an example of lidar data. The sodium atom layer usually exists between 80 and 110 km with a peak height between ~ 87 – 92 km. The lower edge of the sodium layer is sharp with a scale height of 2–3 km, reflecting the rapid conversion of Na into molecules such as NaHCO_3 (Plane 2003). The top-side of the layer also has a small scale-height because of the conversion of Na into Na^+ in the lower ionosphere. Figure 23 shows sodium atom density data obtained at Tromsø (67° geomagnetic latitude; $(69.6^\circ\text{N}, 19.2^\circ\text{E})$ in geographic coordinate) (Nozawa et al. 2014) over 11 hours, starting from 15:30 UT on 1 November 2012.

Variation of sodium density on November 1, 2012

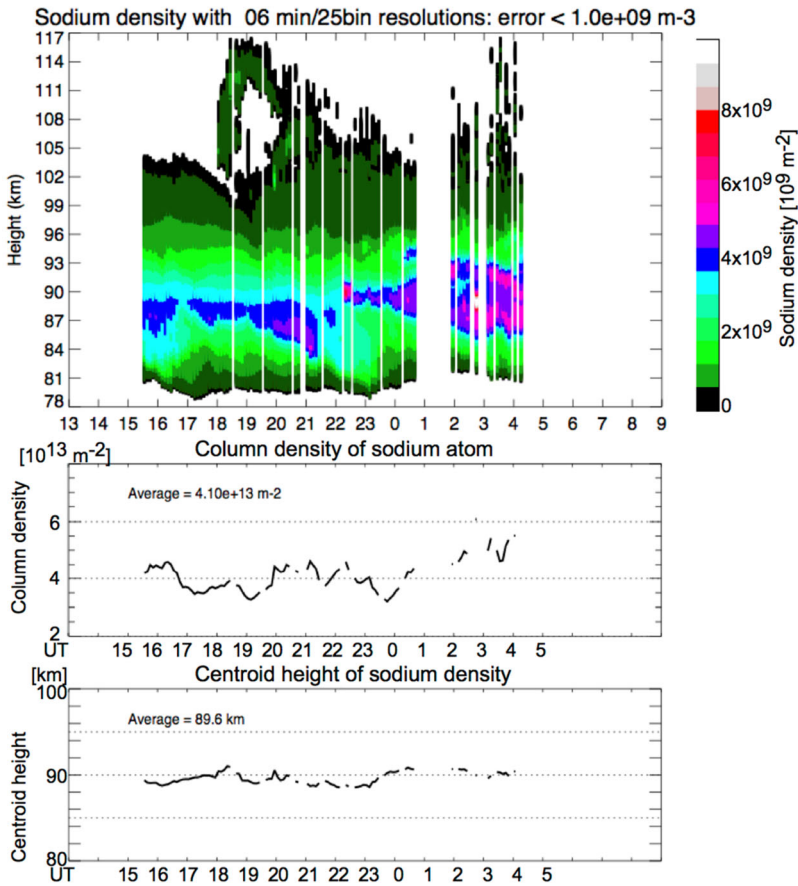


Fig. 23 Sodium (Na) atom density (top), column sodium atom density (middle), and the centroid height (bottom) with 6 min/1 km resolutions obtained with the sodium LIDAR at Tromsø on 1 November 2012. This particular sodium lidar at Tromsø cannot make observations under sunlit conditions (this is why the observation is limited between about 15:20 UT and 04:20 UT for this day)

On this particular night (1 November 2012), the upper part of the sodium layer extended above 110 km from about 18 to 20 UT, beyond daily variations. The column sodium density (middle panel) varies with time, and does not show any particular increase during the time interval. The centroid height of the sodium density (bottom panel) varies with time in height range between 89 and 91 km, and again no special feature is found during 18 and 20 UT. It was rather geomagnetically active interval with 3 hourly local K index (3-hour resolutions) at Tromsø being 6 (15–18 UT) and 6 (18–21 UT). Thus, although the cause of the extension of the sodium density above 110 km is not clear at the moment, auroral activity could be involved.

Figure 24 shows one such example on 7 October 2015 during the major storm as summarized in Sect. 4.2.1. Tromsø Na lidar data (sodium density) started observation from 17 UT, about the one hour after e-POP detected heavy molecular ion upflow at around 20.4 MLT

Variation of sodium density on October 7, 2015

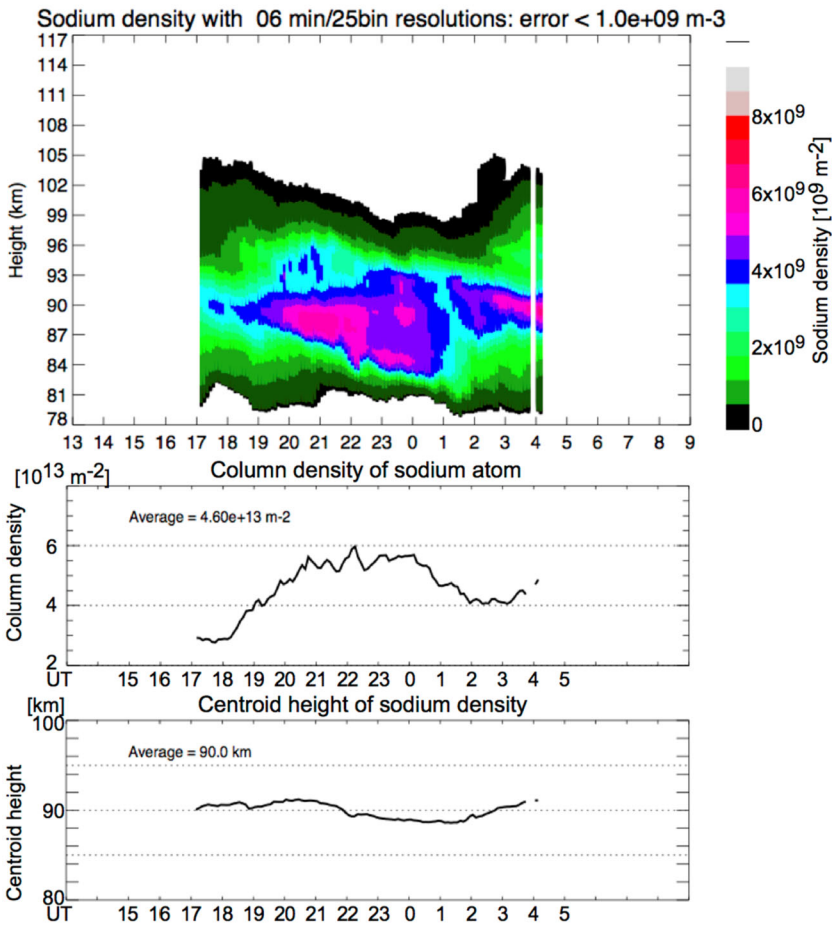


Fig. 24 Same as Fig. 23a but for on 7 October 2015, right after the e-POP event in Fig. 24b

(corresponds to about 19 UT at Tromsø) as shown in Fig. 18. The local K-index (3-hour resolutions) at Tromsø was 5, 7, 6, 4, 5 from 15 UT on 7 October 2015 and AL reached < -1500 nT during 18–19 UT. While the e-POP observation for the traversals at later hours are not optimum, both Dst and AE are developing during the following few hours after the e-POP detection of molecular ions at around 16:15 UT.

During those few hours, the lidar detected significant variation of sodium density and thickness of the layer. The upper edge of the sodium layer (the density of $5 \times 10^7 \text{ m}^{-3}$) was located at 100 km at 17 UT, decreasing with time to reach about 95 km at 23 UT on the same night. The auroral activity was high, implying that the sodium density variation and the altitude variation can be partly due to the auroral effect and gravity waves, superimposed on the diurnal tidal variation. This upward expansion of the Na signal, which is not as clear as shown in Fig. 23 (1 November 2012), can be due to daily variation but may also have some relation with enhanced access of the molecular ions to the topside ionosphere, which is suggested from the e-POP observation.

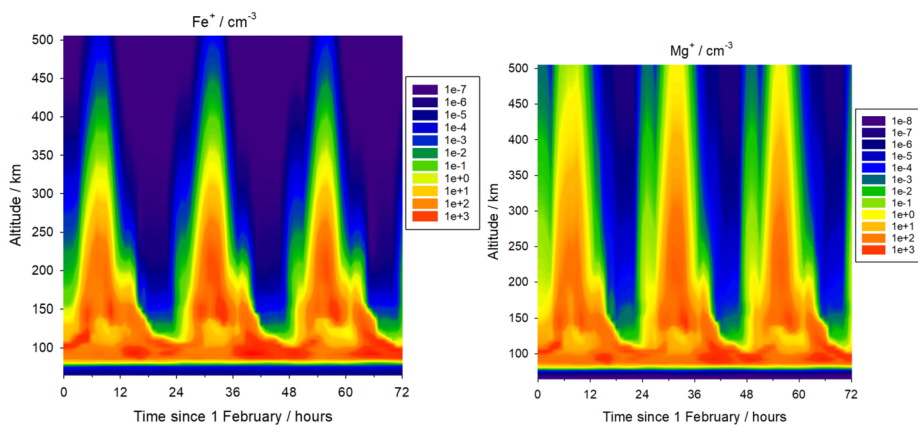


Fig. 25 Modelled Fe^+ (left-hand panel) and Mg^+ (right-hand panel) concentrations (units: ion cm^{-3}) calculated by WACCM-X for 3 days from February 1st, at 80° S and 90° E. The time axis refers to UT. Although the highest Fe^+ and Mg^+ concentrations are in the main layers below 120 km, there is significant uplift of the metal ions to ~ 500 km (the model top) starting around 03:00 UT (09:00 local time)

Finally, very long-time monitoring of the metal layer by lidar potentially has another merit from the space safety monitoring viewpoint. For elements whose relative abundance is much higher in space debris than in meteoroids, we might be able to detect the effect of ablation of space debris (space waste) as an increase in the column density in future mesospheric and thermospheric observations.

4.3.3 Model of Neutral Wind for Heavy Elements

The possibility of metallic ions reaching the exobase and magnetosphere can be explored using models of the upper atmospheric transport of heavy elements to high altitudes potentially beyond the exobase. Recently, two global circulation models, SAMI3 (Huba et al. 2019) and WACCM-X (Wu et al. 2021), have been developed to study the transport of metallic ions in the thermosphere. WACCM-X is a chemistry-climate model that includes the injection of metals from meteoric ablation, and the full neutral and ion-molecule chemistry of Fe ($m = 56$), Mg ($m = 24$) and Na ($m = 23$). This model shows that metal ions are transported to altitudes above 400 km at low geomagnetic latitudes by $\mathbf{E} \times \mathbf{B}$ forcing - the so-called daily “fountain effect” (Wu et al. 2021).

Figure 25 shows an example of WACCM-X model output for the southern polar region during average geomagnetic conditions in February (i.e., slightly after the summer solstice and perihelion, when ionizing solar radiation maximizes). The model predicts that both Fe^+ and Mg^+ daily reach 500 km altitude, which is the top of the model and most likely above the exobase, even during average geomagnetic condition. By reaching the exobase, these metallic ions may access space in the same manner as molecular ions. Figure 25b shows that more Mg^+ than Fe^+ reaches this altitude, reflecting its lower mass. This behavior is only seen in the model for southern polar latitudes during summer. The corresponding uplift in northern polar latitudes during summer is much smaller. Considering the high-latitude location where molecular ions are known to reach high altitudes (Sect. 2.2), those metallic ions that reach the exobase might even access the high altitudes. During geomagnetic disturbed periods when we expect stronger upward convection, these metallic ions may even reach the magnetosphere.

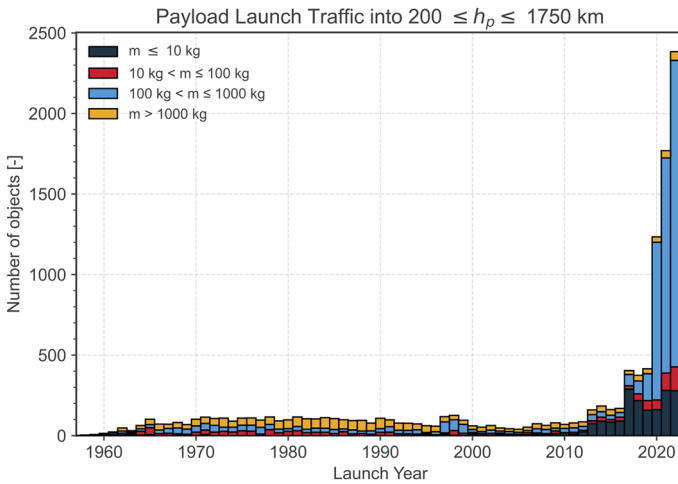


Fig. 26 Image reproduced with permission from ESA (2023)

Table 13 Orbiting artificial objects. Image reproduced with permission from ESA (2024)

	2019-01	2022-12	2024-08
orbiting satellite ^{*1}	~ 5000	~ 9780	~ 13030
debris on catalogue	~ 22300	~ 32400	~ 35790
total mass of orbiting objects	> 8400 t	> 10500 t	> 12900 t
\sum fragmentation events	> 500	> 630	> 650
number of debris(> 10 cm)	~ 40500 (model estimate 2024)		
number of debris(1–10 cm)	~ 1.1 million (model estimate 2024)		
number of debris(0.1–1 cm)	~ 130 million (model estimate 2024)		

^{*1} Both functional and nonfunctional ones

4.4 Re-Entering Space Debris as a Heavy Ion Source: Outlook and Unanswered Questions

Today's society is heavily reliant on the space infrastructure (satellites), and one can safely assume that this dependence will only increase in the near future (ESA 2023). The surge of large satellite constellations (LSC) consisting of several 1000 satellites due to the commercialization of space will increase the number and mass of spacecraft launched into Earth's orbit exponentially. The start of this exponential rise stemming from the installation of LSCs can already be seen today, as depicted in Fig. 26. Table 13 gives this sharp rise in numbers: total number and mass of the orbiting objects increased by 2.5 times and 1.5 times, respectively, during the past five years.

Decommissioning of spacecraft and remnants of launch vehicles lead to the re-entry of space debris/waste into the atmosphere, where it ablates and injects atoms and ions as described in Sect. 2.3.2. However, very few existing studies modelling spacecraft re-entry focus on the atmospheric mass injection as this topic has been mostly disregarded in the past.

Comprehensive atmosphere mass input calculations and observations of particles transported downwards to stratosphere heights show that the injection of metal atoms and ions into the atmosphere is already higher due to the ablation of space debris/waste than the meteoroid input for some element species, currently Al, Cu, Ge, Li and Pb (Schulz and Glassmeier 2021; Murphy et al. 2023). Other rare metallic elements have also been observed (such as Nb, Ag, and Hf) and even traces of a large number of additional metals. In the future, the projected and already occurring strong increase in on-orbit spacecraft mass will lead to other element species injecting more mass compared to the natural input, namely Ti and Ni and a large number of the trace metals. Thus, the possibility of environmental effects and the contamination of the mesospheric heavy ion source should not be underestimated as even the rocket-boosters used to launch payloads into space contribute to the artificial influx as they partially ablate during re-entry (Schulz and Glassmeier 2021). It has even been suggested that the increase of re-entering material due to mega-constellations can begin an uncontrolled experiment of geoengineering by altering the Earth's albedo (Boley and Byers 2021).

Additionally, fragmentation events like explosions, impacts and loss of mass (solid rocket motor dust, paint flakes and other ejecta), or deliberate destructions lead to a continued growth of the number of space objects parallel to the increasing overall mass (Lawrence et al. 2022; Kastinen et al. 2023). Fragmentation is a constant source of sub 100 μm particles in LEO, which are extremely numerous (see Table 13). It is currently unclear how far down the size range of these sources extend. It is also unclear whether these particles undergo further processing and transport to contribute as a heavy ion source before particles are lost from the system due to atmospheric drag or solar radiation. Space missions measuring dust in this size range in LEO, like dust instruments on board *Destiny+* asteroid mission (Krüger et al. 2019), are vital in studying these questions.

Finally, the increase in rocket launches might have an effect on ion transport from mesospheric heights due to gravity and acoustic waves generated by rocket exhaust (e.g. Noble 1990; Mabie et al. 2016), although its effectiveness is unclear.

5 Summary and Future Observation

5.1 Summary of Unanswered Science Questions

For high charge-state heavy ions that obviously originate from the solar wind (including solar energetic particles), there are some statistics for each large-scale region as shown in Fig. 1, but even the basic entry route, the entry mechanism (similarity and differences between the metallic ions and protons, e.g., importance of the finite gyroradius effect for different m/q values such as Fe^{11+} with $m/q=5$), and energization level from the original source are still unanswered. This is mainly due to the severe limitations of the existing instruments for such measurements. So far Geotail/STICS provided the best dataset for high charge-state heavy ions in the magnetosphere and its surroundings, but the instrument capability is limited to high energy ions of > 100 keV, and has very low time resolution for heavy ions. Therefore, we could not even distinguish between the direct effect of the solar wind and the magnetospheric activities that influence the configuration of the magnetospheric boundary.

The same problem applies to the low charge-state metallic and heavy molecular ions, which have several candidates as the source. We stress here that their extremely low flux (no single source is hiding the other sources like H^+ or O^+) in turn makes these ions unique tracers that provide independent information on the source and the supply route from the

four major species (H^+ , He^+ , He^{++} , and O^+) provide. In addition, even the sources are not identified, such as, the contribution from the Moon compared to the Earth's upper atmosphere, and within the upper atmosphere, what fraction of the ions coming from the nightside sub-auroral region compared to the dayside polar region. The only route so far established is dayside high latitude region (through the plasma lobe) for heavy molecular ions, the same route as one of the routes for O^+ circulation. For this source, heavy ions are expected to undergo a similar pathway and energization until they reach the inner magnetosphere (Yamauchi 2019, and references therein). The other routes are difficult to identify, and it is even more difficult to evaluate the effect of the external conditions (e.g., solar wind, magnetospheric activity, Moon phase) under which ions from these sources appear.

Nevertheless, by re-examining the existing data from instruments that were not designed for separating molecular ions (e.g., Cluster/CODIF), and combining them with new data (e.g., from e-POP), we could identify new direct supply routes of the molecular ions (auroral region) to the inner magnetosphere, which is independent from the known high-latitude route.

Re-examination of existing data (e.g., Geotail/STIC and ACE) and combining with other datasets (e.g., Kaguya and Chang'e) is also important in evaluating the Moon source as discussed in Sect. 4.1: We cannot rule out the possibility of a substantial contribution from the Moon during CIR/CME time periods. Thus, we still do not know the relative importance among the Moon, mesosphere, and the solar wind as the source of the low-charge state metallic ions. In this respect, further examination of Kaguya data (the mission terminated in 2009 after about 1.5 years of operation) is important as well as continued analyses of ongoing e-POP and Arase data and new analyses of MMS, all of which are capable of detecting molecular ions and/or metallic ions using full TOF data.

For the other possible clues to investigate the upflow of the metallic ions, new models like WACCM-X and SAMI show that metallic ions might be transported regularly to altitudes above 500 km (above the exobase) at particular locations (mainly high altitudes). These models should ideally be combined with ionosphere-magnetosphere models and with possible observations in the future (see Sect. 5.3 below). Such model-model and model-observation comparisons will further determine the probability that these heavy metallic ions can be lifted into the magnetosphere. Finally, contamination by space debris/waste emerges as a new open question, requiring new work in the future.

5.2 Desired Specification for Observation and Modeling

Since our observational knowledge on the heavy molecular and metallic ions ($m > 20$) in the magnetospheric is very poor, we first need to define what measurements are highest priority for these ions. The lack of dedicated missions in the past is partly because it has been difficult to design ion instruments that can separate heavy species with sufficient geometric factor. To design the optimum set of feasible instrumentation, we need to know the limitation of the ion instruments on board past and current spacecraft. The limitations are:

1. In energy coverage: e.g., the IRM ion mass spectrometer onboard e-POP was limited to ions up to 90 eV/e (Yau and Howarth 2016), and the STICS ion mass spectrometer onboard Geotail had an energy threshold of ~ 10 keV (Williams et al. 1994).

2. Ambiguity of ion trajectory with finite entrance cross-section and small deviation of electric and magnetic field inside the instrument reduce the mass resolution: e.g., the CODIF ion mass spectrometer onboard Cluster had a mass resolution of $m/\Delta m \approx 5-7$ (Rème et al. 2001), and HPCA onboard MMS had $m/\Delta m = 4-8$ (Young et al. 2016).

3. Size of the instrument and upper limit of the field strength inside the instruments limit the mass range.

4. Fragmentation of the molecular ions when going through the thin carbon foil limits the molecular ion measurements for foil-type TOF instruments (e.g., Heredia-Avalos and Garcia-Molina 2000).

5. Insufficient geometric factor, which requires long integration time to accumulate adequate counting statistics for minor species (e.g., Haaland et al. 2020). Currently, obtaining angular (pitch angle) information within a short sampling time and at high mass resolution is not easy.

6. The instrument sensitivity degrades over the years due to the damaging of the detector, e.g., by ion and electron bombardments (e.g., Kistler et al. 2013).

7. Gaussian (as opposed to exponential) line shape of instrument mass response results in non-negligible contributions to the measured minor ion counts from nearby major ion species (see Fig. 19).

As a result, even the separation of the molecular ion measurements (separating $m/q \approx 30$ from $m/q = 16$ without charge state information) has been difficult for medium energy (50 eV–50 keV), for which Arase was the first magnetospheric mission that can separate the molecular ion group at the medium-energy (MMS is probably possible but no analyses are published). The instrument onboard Wind is designed to resolve the medium-energy molecular ions, but the achieved resolution was not sufficient due to technical issues. Therefore, unlike traditional ion mass analyzers for the four major magnetospheric species (the H^+ , He^{++} , He^+ , and O^+ group), we cannot require sufficient resolution for all directions (temporal, energy, angular) when measuring the metallic and heavy molecular ions.

With these limitations in mind, we have to define the direction of instrumentation and measurement improvements to advance our knowledge.

1. Have a mass range up to > 60 amu, to include Fe ions and heavy ionospheric molecular ions (see Fig. 1).

2. Cover most important energy ranges that are different in different magnetospheric regions: from cold ions (eventually few eV by ram flow) up to < 100 eV corresponding to the upwelling ions at low altitudes below the main energization region (Yau et al. 2021), from a few eV up to a few keV corresponding to the outflowing heavy ions at high altitudes above the main energization region or the cusp (Kistler et al. 2010b), up to few 10's of keV corresponding to energetic heavy ions streaming down tail (Christon et al. 1994; Seki et al. 1998), and to a higher energy range for ions in the ring current, where the returning ions experience adiabatic acceleration (Ejiri 1978). The wide energy range is also needed in the magnetospheric boundary region where pickup cold heavy ions and foreshock heavy ions can gain energy (Grünwaldt et al. 1997; Stasiewicz et al. 2013).

3. Obtain modest angular resolution with respect to the magnetic field while providing a mass resolution $m/\Delta m \geq 15$ over a wide energy range. This allows separating minor molecular ions ($m = 25\text{--}35$) from CNO-group atomic ions ($m < 20$), and minor heavier metallic ions ($m > 40$) from molecular ions. Such a mass resolution can be achieved through an isochronous TOF ion mass spectrometer, such as e.g. Mio/MSA (Delcourt et al. 2016) and JDC instrument onboard JUICE (Wittmann 2022), or through a grazing incidence MCP time-of-flight ion mass spectrometer (Devoto et al. 2008). Alternatively, for ions up to keV, a magnetic ion mass spectrometer such as the IMA instrument onboard Mars Express (Barabash et al. 2006) would achieve this requirement by tuning the mass range and size (Nicolaou et al. 2017). The advantage of this design is that the ions do not touch the instrument elements other than the final detector (no fragmentation nor loss of energy).

4. Employ a high geometric factor design, or a new filtering or new starting mechanism of TOF (against the fragmentation of the molecular ions at the start foil/surface for the TOF section) to allow for the separation of molecular ions (peaks in mass-range histogram are

high enough to separate, e.g., NO^+ peak from O_2^+ peak) within 30 minutes for keV ranges and 10 minutes for cold ions.

5. Employ a high mass resolution design of $m/\Delta m \geq 60$, to separate Al^+ ($m = 27$) from Si^+ ($m = 28$) or N_2^+ ($m = 28$) at least above the ionosphere and in the ring current. The CELIAS/MTOF instrument on the SOHO spacecraft provided such a mass resolution for solar wind ions, i.e., for 0.5–30 keV/nucleon ions (Hovestadt et al. 1995). There are designs and prototyping for such instruments that allow even for $m/\Delta m > 100$ (Wurz et al. 1998). Rosetta was equipped with a design for cold (< 10 eV) ions (Balsiger et al. 2007). The technology is also available for hot (0.05–10 keV) ions in Kaguya/IMA (Saito et al. 2010), i.e., $m/\Delta m > 15$, and improved to $m/\Delta m > 40$ for Mio (launched 2018), and $m/\Delta m > 100$ for MMX (to be launched in 2026).

6. Time resolution must be sufficient to separate different possible supply routes (e.g., the direct supply from the ionosphere and detoured supply through the tail) and to complete the traversal over each region. Here, the mass resolution and time resolution are related, and higher energy ranges generally require longer integration time due to the much lower ion flux in the Earth's magnetosphere. If we require as low as $m/\Delta m > 15$, instruments that fulfill this requirement (tens of minutes to hours to move from one region to another for high-altitude mission) are available almost all energy ranges.

The monitoring of the heavy ions is needed both in the magnetospheric region and in the possible source region. While the solar wind is being monitored at L1 for space weather monitoring purposes, a new monitoring spacecraft or base is need for the Moon and the upper atmosphere (ionosphere and upper mesosphere). Here, the ionosphere includes both lower altitudes (thermosphere part) and above the exobase. To correlate any "event" in the source region with the magnetospheric observation, time resolution must be comparable or better than such an "event" duration, which means a time resolution < 10 minutes (e.g., substorms) for ionospheric origin low energy ions and hours for Moon origin ions or magnetospheric high-energy ions. This imposes a severer requirement on the instrument sensitivity because the STICS instruments on board Geotail and Wind (the only instruments that detected metallic ions in the Earth's magnetosphere) detected Fe^+ ions only at the level of one count per half a month on average (see Sect. 4.3.1). We need to improve the detection ability (sensitivity) of the metallic ions of this energy range ($>$ tens of keV) by two-three orders of magnitude.

On the other hand, the duration of heavy ion events in the magnetosphere can be as long as a few days, i.e., the time scale of magnetic storms. Also, CME and CIR last from several hours to a day. The question is then whether the heavy ions are supplied intermittently or continuously, or simply at one time with a slow and long decay. To distinguish between them, we need continuous monitoring (i.e., for the same spacecraft to return to the same region) over several days in raw. These time-scale requirements limit the types of acceptable spacecraft orbits.

5.3 Desired Missions and Observations

For in-situ observations, the best is to have dedicated missions, even as a secondary objective of any mission. Alternatively, placing a set of instruments on non-science missions such as Earth Observation satellites and Space Safety missions (including geostationary ones) or the transfer spacecraft to or from the upcoming Lunar Gateway. The current plan for the Lunar Gateway is to be equipped with HERMES (Heliophysics Environmental and Radiation Measurement Experiment Suite) instrument package, comprising also the SPAN-Ai Ion Mass Spectrometer (0.02–40 keV ions, although $m/\Delta m$ is currently about 10).

In all cases, the key instruments are (1) an ion mass spectrometer with $m/\Delta m > 60$ for a wide mass range of $m/q > 60$, and (2) another ion mass spectrometer of lower mass resolution ($m/\Delta m > 15$) but sufficient angular resolution of at least 22.5° (6° is ideal because, for example, this is needed to detect the position where the ions are generated around the Moon), while keeping the mass range up to $m/q > 60$. (3) In addition, adding a total ion flux instrument without mass resolution but with very good $\Delta E/E$ is a good complement for absolute accuracy in density and velocity. The energy range of the instruments is divided into (a) cold, (b) hot up to few tens of keV, and energetic. For the hot ions, it would be wise to divide the design into two different energy ranges to have better energy and mass resolution. In this case, it is also wise to use different detection methods for different (divided) energies. In addition to the ion instruments, the technology of (4) optical limb observation from satellites has also advanced, e.g., sounding of Mg^+ . If limb observation becomes possible for the other metallic species, this would be a strong satellite tool in the future.

Any of these key instruments are useful to be placed on the other (non-dedicated) missions mentioned above (as a package). As for the dedicated mission, it would be good to have a multi-spacecraft mission with the spacecraft having different orbits, such as low altitude (400–4000 km), mid altitude (2000–30000 km), and high altitude (4–10 R_E), as well as the ionospheric source altitude (200–500 km). Monitoring of the possible source population is also important. For the solar wind source, L1 monitoring spacecraft has been providing and will provide key information, whereas for the Moon source, the coming Lunar Gateway would be a good platform to place key instruments like Kaguya/IMA.

If only one spacecraft is available, then the mission should aim for all escaping ions, and have a highly elliptic orbit because most of the Earth observation satellites are in nearly circular orbits, such as the ESCAPE (European SpaceCraft for the study of Atmospheric Particle Escape) mission, which was proposed to ESA in response to the M5 call (Dandouras et al. 2018). The proposed ESCAPE mission spacecraft was designed as a slowly spinning spacecraft on a high inclination 500 km \times 33 000 km orbit, i.e., with a perigee at the terrestrial exobase, and was equipped with instrumentation responding to the above criteria. With many ion mass instruments with an optical monitor of the exospheric heavy atoms, it was designed to separate even nitrogen and oxygen. With modern technology, several dips into much lower altitudes to cover the middle thermosphere and ionosphere could be considered, similar to what the MAVEN satellite did on Mars with the Neutral Gas and Ion Mass Spectrometer (NGIMS) instrument onboard.

The monitoring of the source region is also essential. Since the Moon monitor is mentioned in the previous subsection, we describe here the Earth (ground-based) part of the observations including the ultimate source of meteorites. Here, the important outputs are how much of the source ions may reach the exobase and topside ionosphere. This requires, in addition to monitoring the geomagnetic activity that is already available, (1) instruments and models that provide upward transport of heavy ions in the mesosphere, ionosphere, and thermosphere with high spatial resolution, and (2) monitoring of possible source population (although it is only “possible” source with current understanding) of the metallic ions and atoms in the lower part of the ionosphere. A candidate for (1) is modern incoherent scatter radar such as EISCAT_3D, and a candidate for (2) is lidars.

For lidars, we need to keep the existing observation sites, and even expand to more observation sites (ideally two latitudes, at $\sim 80^\circ$ and $\sim 60^\circ$, respectively, in both hemispheres corresponding to two major outflow latitudes that e-POP revealed, and three longitudinal locations to separate temporal and diurnal variations) as well as target species. We particularly need to monitor the Ca^+ layer (ionized form) and the Fe layer (originating from mainly meteoroids, but space debris/waste might become detectable the first among all metallic

species), while searching for AIO (the Al species observable by lidar) could be useful for evaluating the contribution from the space debris/waste, although its current AIO density predicted by an atmospheric model is very low (Plane et al. 2021).

Since it is unclear how much transient enhancements of the metal layer influence the total upward transport (such as by meteor showers and large re-entry events of space debris/waste) it is desirable to gain a more complete picture of the current input of mass to the atmosphere. This also includes the observation of the ablation process, by which the material is distributed in the atmosphere. These observations should be performed using many different detection methods (e.g. dust detectors, lidars, radars, optical systems) and missions.

Observations of the actual ablation process are particularly important for evaluating the ablation of space debris/waste in depositing the minor species in the upper ionosphere because modelling and indirect observations suggest that minor species such as Al, Cu, Ge, Li and Pb coming from space debris/waste might already constitute a significant contamination to the naturally occurring particles from meteoroids. To evaluate this effect, a multi-probe experimental flight through a possible ion cloud (measurement by the second probe during its re-entry after re-entry of the first probe that imitates the space debris/waste) would be useful. Such an experiment would gather information about the ablated amount and altitude distribution, as well as the effectiveness of vertical transport of the generated ion cloud. For such an experiment, remote observations from LEO satellites should also be added by aligning the re-entry orbit to the ideal LEO satellite for monitoring. As a similar attempt, the *Deadalus* proposal (Sarris et al. 2020) can make such an attempt although the target is ionosphere but not mesosphere or stratosphere where the ablation of re-entry objects takes place.

5.4 Modelling of Upward Transport of Metallic and Molecular Ions in the Ionosphere and Mesosphere

It would be ideal if one can assimilate the relatively rare observations (e.g., in Sect. 4) into thermospheric and ionospheric transport models. The molecular ion upflow at sub-auroral latitude and sudden expansion of the metal layer (see the example in Sect. 4.3.2 for Na) are examples that need to be reproduced by transport models.

For modelling (particularly for evaluating the ablation of space debris/waste), the source flux for the solar wind and the upper atmospheric molecular ion distribution as the ground state are well understood. Also, in the case of the mesospheric metal layers, the current understanding is quite mature, and we have a long history of measurements and models. As such, for the purpose of transport to the magnetosphere, the mass input to these metal layers by meteoroids is no longer required in modelling except for the increasing input from the ablation of the space debris/waste.

On the other hand, understanding the transport of heavy metals from the mesosphere to higher altitudes needs further understanding because of lack of monitoring satellites for these heavy ions for past 40 years as summarized in Table 7. The last capable satellite was DE-2 in early 1980s and flight much higher altitude than exobase. Alongside such additional observations, model development is also needed to evaluate the transport of metallic ions to beyond the exobase. Currently WACCM-X reaches 500 km altitude but not further. One possible development could be to couple such atmospheric and ionospheric models with magnetospheric models of wave-particle interaction. This would extend the modelling regime into the magnetosphere and would yield predictions that could be compared with measurements.

Although the meteoric mass input to the atmosphere is roughly known and it is possible to estimate the contribution from the re-entry of human-made objects (e.g., satellites and

space debris), the details concerning the ablation needs more modelling and observations, and total influx estimates and its composition need refining. Without these details, one cannot evaluate in what way and how much these influxes contribute to the mesospheric metal layer. Such evaluations are particularly important in prognoses of the future evolution of the metal layer by space debris/waste, and hence ultimately by the increasing launch of rockets to the space. Almost no observational work has been done on examining the deposition altitude distribution and composition from deorbiting debris. Thus, comprehensive modelling of the ablation process of space debris/waste is needed. Due to the complex nature of the ablation and the subsequent chemical and physical processing of the injected material, modelling should be complemented and validated by more detailed and numerous observations of spacecraft re-entries, especially of spacecraft resembling typical orbital and mass characteristics of the already numerous low-Earth orbit communication satellites (LCS). Although there are estimates on the total influx of debris based on the mass of objects contained in regions that will deorbit, the deposition altitudes are key to understanding the impact on our atmosphere. In some areas it might be time-critical to intensify the research before the anthropogenic influence due to the increase in re-entry of space debris/waste reaches a level that causes significant perturbations to natural environment in the atmosphere and the space.

6 Conclusion

Very minor ions in the magnetosphere carry unique information because of their low flux (no single source is hiding the other source like the case for H^+ or O^+), on both the source and the transport route. However, their transport is not well understood because of the lack of observations, which partly results from the instrument capabilities for the terrestrial missions in the past and present. While we need new observations with suitable instrumentation, the technology and design of which are already available and are used in current planetary missions, re-examining the exiting datasets, and combining different datasets can also give new insights on this subject. We have shown several examples for such re-examinations of data, e.g., the importance of considering the Moon and space debris/waste as the detectable sources for the metallic ions in the magnetosphere. Therefore, a related database of measurements taken by old instruments listed in Sect. 3 with designs more than 20-years old are still useful, along with more recent models. This in turn means that we need new observations and missions in the near future with available technology, as summarized in Sect. 5.

Acknowledgements The work was supported by International Space Science Institute (ISSI) in Bern, through ISSI International Team project #518. JMCP was supported by the European Office of Aerospace Research and Development (award no. FA8655-21-1-7031). We thank Victoria Foss for providing Fig. 18, which is from her thesis research and is to be submitted for publication, and thank Wuhu Feng (National Centre for Atmospheric Science, UK) for providing the WACCM-X data shown in Fig. 25. The French participation in the Cluster project (part of the work by ID) has been supported in part by CNES. IM's work is within a project funded by Research Council of Norway, NFR 275503.

Dst and AE (used in Sect. 4.2.1 and Sect. 4.3.2) are provided by the World Data Center for Geomagnetism, Kyoto (<https://wdc.kugi.kyoto-u.ac.jp/wdc/Sec3.html>). Tromsø geomagnetic field (used in Sect. 4.3.2) is provided by Tromsø Geophysical Observatory (<https://flux.phys.uit.no/stackplot/>). Kp (used in Sect. 4.1.1 and 4.2.1) is provided by GFZ German Research Centre for Geosciences (<https://isdc.gfz-potsdam.de/kp-index/>). SOHO proton monitor data (used in Sect. 4.1.2) is provided by the SOHO/CELIAS/MTOF Proton Monitor team (<https://space.umd.edu/pm/>). Geotail STICS, LEP, and orbit data (used in Sect. 4.1.2) are provided by GEOTAIL/EPIC Science Data Center (http://sd-www.jhuapl.edu/Geotail/Years_dir.html), Geotail database (<https://www.stp.isas.jaxa.jp/geotail/>) and ERG Science Center (<https://ergsc.isee.nagoya-u.ac.jp/cef/orbit.cgi>), respectively. ACE level 3 data (used in Sect. 4.1.2) are provided by the ACE team (<https://izw1.caltech.edu/ACE/ASC/DATA/level3/summaries.html>). All Cluster data are available at the Cluster Science Archive (<https://csa.esac.esa.int/csa-web/>).

Author Contribution All contributed discussion and Sects. 1 and 3. MY overviewed all sections. For Sects. 2 and 4, the main contributors are: Solar wind observations (CS, LMK, PW), the Moon observations and models (YS, PW, MY), magnetospheric observations (CS, ID, SH, LMK, YS, MY), ionospheric outflow observation and model (ID, SW, MY, AWY), ionosphere (AWY), meteoroid/debris ablation (DK, JMCP, LS, IM), metal layers (SN, JMCP). Finally, Sect. 5 is contributed by ID, DK, LMK, JMCP, LS, YS, PW, MY, and AWY.

Funding See acknowledgement.

Data Availability See tables in Sect. 3 and acknowledgement.

Code Availability Summarized in tables in Sect. 3.

Declarations

Competing Interests Not applicable.

Open Access This article is licensed under a Creative Commons Attribution 4.0 International License, which permits use, sharing, adaptation, distribution and reproduction in any medium or format, as long as you give appropriate credit to the original author(s) and the source, provide a link to the Creative Commons licence, and indicate if changes were made. The images or other third party material in this article are included in the article's Creative Commons licence, unless indicated otherwise in a credit line to the material. If material is not included in the article's Creative Commons licence and your intended use is not permitted by statutory regulation or exceeds the permitted use, you will need to obtain permission directly from the copyright holder. To view a copy of this licence, visit <http://creativecommons.org/licenses/by/4.0/>.

References

- Allen RC, Livi SA, Vines SK, et al (2017) Storm-time empirical model of O⁺ and O₆⁺ distributions in the magnetosphere. *J Geophys Res* 122:8353–8374. <https://doi.org/10.1002/2017JA024245>
- Anders E, Grevesse N (1989) Abundances of elements: meteoritic and solar. *Geochim Cosmochim Acta* 53:197–214. [https://doi.org/10.1016/0016-7037\(89\)90286-X](https://doi.org/10.1016/0016-7037(89)90286-X)
- Asamura K, Kazama Y, Yokota S, et al (2018) Low-energy particle experiments-ion mass analyzer (LEPi) on-board the ERG (Arase) satellite. *Earth Planets Space* 70:70. <https://doi.org/10.1186/s40623-018-0846-0>
- Asplund M, Grevesse N, Sauval AJ, Scott P (2009) The chemical composition of the sun. *Annu Rev Astron Astrophys* 47:481–522. <https://doi.org/10.1146/annurev.astro.46.060407.145222>
- Balsiger H, Altwegg K, Bochsler P, Eberhardt P, et al (2007) ROSINA - Rosetta orbiter spectrometer for ion and neutral analysis. *Space Sci Rev* 128:745–801. <https://doi.org/10.1007/s11214-006-8335-3>
- Bame SJ, Asbridge JR, Hundhausen AJ, Strong IB (1968a) Solar wind and magnetosheath observations during the January 13-14, 1967, geomagnetic storm. *J Geophys Res* 73(17):5761–5767. <https://doi.org/10.1029/JA073i017p05761>
- Bame SJ, Hundhausen AJ, Asbridge JR, Strong IB (1968b) Solar wind ion composition. *Phys Rev Lett* 20:393–395. <https://doi.org/10.1103/PhysRevLett.20.393>
- Bame SJ, Asbridge JR, Hundhausen AJ, Montgomery MD (1970) Solar wind ions: ⁵⁶Fe⁺⁸ to ⁵⁶Fe⁺¹², ²⁸Si⁺⁷, ²⁸Si⁺⁸, ²⁸Si⁺⁹, and ¹⁶O⁺⁶. *J Geophys Res* 75(31):6360–6365. <https://doi.org/10.1029/JA075i031p06360>
- Bame SJ, Asbridge JR, Feldman WC, et al (1975) Solar wind heavy ion abundances. *Sol Phys* 43:463–473. <https://doi.org/10.1007/BF00152368>
- Barabash S, Lundin R, Andersson H, et al (2006) The Analyzer of Space Plasmas and Energetic Atoms (ASPERA-3) for the Mars Express Mission. *Space Sci Rev* 126:113–164. <https://doi.org/10.1007/s11214-006-9124-8>
- Barabash S, Fedorov A, Lundin R, et al (2007) Measurements from Mars Express show that the solar wind is removing only a small amount of Mars' atmosphere, implying that the formally abundant H₂O and CO₂ remain underground. *Science* 315(5811):501–503. <https://doi.org/10.1126/science.1134358>
- Battie F, Fossati T, Gallucci S (2013) Vega 4th stage direct re-entry survivability analysis and causality risk assessment. In: *Proceedings of 6th European conference on space debris*, vol 723, p 57. <https://conference.sdo.esoc.esa.int/proceedings/sdc6/paper/144/SDC6-paper144.pdf>
- Berner RA (1999) Atmospheric oxygen over Phanerozoic time. *Proc Natl Acad Sci USA* 96:1095510957.

- Berner RA (2006) Geocarbsulf: a combined model for Phanerozoic atmospheric O₂ and CO₂. *Geochim Cosmochim Acta* 70:5653–5664. <https://doi.org/10.1016/j.gca.2005.11.032>
- Bingham ST, Nikoukar R, Cohen IJ, et al (2021) Evidence for nonadiabatic oxygen energization in the near-Earth magnetotail from MMS. *Geophys Res Lett* 48:e2020GL091697. <https://doi.org/10.1029/2020GL091697>
- Boley AC, Byers M (2021) Satellite mega-constellations create risks in Low Earth Orbit, the atmosphere and on Earth. *Sci Rep* 11:10642. <https://doi.org/10.1038/s41598-021-89909-7>
- Bones DL, Carrillo-Sánchez JD, Kulak AN, Plane JMC (2019) Ablation of Ni from micrometeoroids in the upper atmosphere: experimental and computer simulations and implications for Fe ablation. *Planet Space Sci* 179:104725. <https://doi.org/10.1016/j.pss.2019.104725>
- Bones DL, Carrillo-Sánchez JD, Connell SDA, Kulak AN, Mann GW, Plane JMC (2022) Ablation rates of organic compounds in cosmic dust and resulting changes in mechanical properties during atmospheric entry. *Earth Space Sci* 9:e2021EA001884. <https://doi.org/10.1029/2021EA001884>
- Borovička J, Spurný P, Koten P (2007) Atmospheric deceleration and light curves of Draconid meteors and implications for the structure of cometary dust. *A&A* 473:661–672. <https://doi.org/10.1051/0004-6361:20078131>
- Borovička J, Koten P, Shrbený L, et al (2014) Spectral, photometric, and dynamic analysis of eight Draconid meteors. *Earth Moon Planets* 113:15–31. <https://doi.org/10.1007/s11038-014-9442-x>
- Breneman HH (1985) Solar photospheric and coronal abundances from solar energetic particle measurements. PhD thesis, California Institute of Technology. <https://doi.org/10.7907/4mma-e885>
- Brosch N, Häggström I, Pellinen-Wannberg A (2013) EISCAT observations of meteors from the sporadic complex. *Mon Not R Astron Soc* 434:2907–2921. <https://doi.org/10.1093/mnras/stt1199>
- Buttsworth D, Morgan R, Jenniskens P (2013) Near-ultraviolet emission spectroscopy of the Hayabusa reentry. *J Spacecr Rockets* 50:1109–1120. <https://doi.org/10.2514/1.A32500>
- Campbell-Brown MD, Borovička J, Brown PG, Stokan E (2013) High-resolution modelling of meteoroid ablation. *A&A* 557:A41. <https://doi.org/10.1051/0004-6361/201322005>
- Canfield DE (2005) The early history of atmospheric oxygen: homage to Robert M. Garrels. *Annu Rev Earth Planet Sci* 33:1–36. <https://doi.org/10.1146/annurev.earth.33.092203.122711>
- Carrillo-Sánchez JD, Gómez-Martín JC, Bones DL, Nesvorný D, Pokorný P, Benna M, Flynn GF, Plane JMC (2020) Cosmic dust fluxes in the atmospheres of Earth, Mars, and Venus. *Icarus* 335:113395. <https://doi.org/10.1016/j.icarus.2019.113395>
- Ceplecha Z, Borovička J, Elford WG, et al (1998) Meteor phenomena and bodies. *Space Sci Rev* 84:327–471. <https://doi.org/10.1023/A:1005069928850>
- Chappell CR, Fields SA, Baugher CR, et al (1981) The retarding ion mass spectrometer on dynamics Explorer-A. NASA technical report NASA-TM-82418. <https://ntrs.nasa.gov/citations/19810016373>
- Chappell CR, Olsen RC, Green JL, et al (1982) The discovery of nitrogen ions in the Earth's magnetosphere. *Geophys Res Lett* 9:937–940. <https://doi.org/10.1029/GL009i009p00937>
- Christon SP, Gloeckler G, Williams DJ, et al (1994) Energetic atomic and molecular ions of ionospheric origin observed in distant magnetotail flow-reversal events. *Geophys Res Lett* 21:3023–3026. <https://doi.org/10.1029/94GL02095>
- Christon SP, Hamilton DC, Plane JMC, et al (2017) Discovery of suprathermal ionospheric origin Fe⁺ in and near Earth's magnetosphere. *J Geophys Res* 122:11175–11200. <https://doi.org/10.1002/2017JA024414>
- Christon SP, Hamilton DC, Mitchell DG, et al (2020) Suprathermal magnetospheric atomic and molecular heavy ions at and near Earth, Jupiter, and Saturn: observations and identification. *J Geophys Res* 125:e2019JA027271. <https://doi.org/10.1029/2019JA027271>
- Cladis JB (1986) Parallel acceleration and transport of ions from polar ionosphere to plasma sheet. *Geophys Res Lett* 13:893–896. <https://doi.org/10.1029/GL013i009p00893>
- Colaprete A, Sarantos M, Wooden DH, et al (2016) How surface composition and meteoroid impacts mediate sodium and potassium in the lunar exosphere. *Science* 351:249–252. <https://doi.org/10.1126/science.aad2380>
- Craven PD, Olsen RC, Chappell CR, Kakani L (1985) Observations of molecular ions in the Earth's magnetosphere. *J Geophys Res* 90:7599–7605. <https://doi.org/10.1029/JA090iA08p07599>
- Dandouras I (2021) Ion outflow and escape in the terrestrial magnetosphere: Cluster advances. *J Geophys Res* 126:e2021JA029753. <https://doi.org/10.1029/2021JA029753>
- Dandouras I, Yamauchi M, The ESCAPE proposal team (2016) European SpaceCraft for the study of Atmospheric Particle Escape (ESCAPE), Mission proposals to 2016 ESA's call for M5 Mission. http://cluster.irap.omp.eu/public/ESCAPE/ESCAPE_M5_Proposal_V1.1.pdf
- Dandouras I, Yamauchi M, De Keyser J, et al (2018) ESCAPE: a mission proposal for ESA-M5 to systematically study exosphere and atmospheric escape using European, Japanese, and US instruments (Japanese with English abstract/tables/figures). In: Proceedings of the 18th space science symposium, SA6000118033. S10-001, 9-10 Jan, 2018, JAXA/ISAS. <https://repository.exst.jaxa.jp/dspace/handle/ais/876320>

- Dandouras I, Blanc M, Fossati L, et al (2020) Future Missions Related to the Determination of the Elemental and Isotopic Composition of Earth, Moon and the Terrestrial Planets. *Space Sci Rev* 216:121. <https://doi.org/10.1007/s11214-020-00736-0>
- Dawkins EMC, Plane JMC, Chipperfield MP, et al (2014) First global observations of the mesospheric potassium layer. *Geophys Res Lett* 41:5653–5661. <https://doi.org/10.1002/2014GL060801>
- Del Pozo CF, Hargreaves JK, Aylward AD (1997) Ion composition and effective ion recombination rate in the nighttime auroral lower ionosphere. *J Atmos Sol-Terr Phys* 59(15):1919–1943. [https://doi.org/10.1016/S1364-6826\(97\)00033-3](https://doi.org/10.1016/S1364-6826(97)00033-3)
- Delcourt DC, Sauvaud JA, Moore TE (1993) Polar wind ion dynamics in the magnetotail. *J Geophys Res* 98:9155–9169. <https://doi.org/10.1029/93JA00301>
- Delcourt D, et al (2016) The Mass Spectrum Analyzer (MSA) on board the BepiColombo MMO. *J Geophys Res Space Phys* 121:6749–6762. <https://doi.org/10.1002/2016JA022380>
- Devoto P, Médale J-L, Sauvaud J-A (2008) Secondary electron emission from distributed ion scattering off surfaces for space instrumentation. *Rev Sci Instrum*. 79:046111. <https://doi.org/10.1063/1.2912821>
- Dobarco-Otero J, Smith RN, Bledsoe KJ, et al (2005) The Object Reentry Survival Analysis Tool (ORSAT) - version 6.0 and its application to spacecraft entry. In 56th international astronomical congress of the international astronomical federation, the international academy of astronautics, and the international institute of space law, B6–3. <https://doi.org/10.2514/6.IAC-05-B6.3.06>
- Dukes CA, Baragiola RA (2015) The lunar surface-exosphere connection: measurement of secondary-ions from Apollo soils. *Icarus* 255:51–57. <https://doi.org/10.1016/j.icarus.2014.11.032>
- Dymond KF, Wolfram KD, Budzien SA, et al (2003) Middle ultraviolet emission from ionized iron. *Geophys Res Lett* 30:1003. <https://doi.org/10.1029/2002GL015060>
- Ejiri M (1978) Trajectory traces of charged particles in the magnetosphere. *J Geophys Res* 83:4798–4810. <https://doi.org/10.1029/JA083iA10p04798>
- Elphic RC, Funsten HO III, Barraclough BL, et al (1991) Lunar surface composition and solar wind-induced secondary ion mass spectrometry. *Geophys Res Lett* 18(11):2165–2168. <https://doi.org/10.1029/91GL02669>
- ESA (2023) ESA's annual space environment report. ESA Space Debris Office. https://www.sdo.esoc.esa.int/environment_report/Space_Environment_Report_latest.pdf
- ESA (2024) Space debris by the numbers. ESA Space Debris Office. https://www.esa.int/Our_Activities/Operations/Space_Debris/Space_debris_by_the_numbers
- Feldman U, Landi E, Schwadron NA (2005) On the sources of fast and slow solar wind. *J Geophys Res Space Phys* 110:A07109. <https://doi.org/10.1029/2004JA010918>
- Feng W, Marsh DR, Chipperfield MP, et al (2013) A global atmospheric model of meteoric iron. *J Geophys Res*, Atmos 118:9456–9474. <https://doi.org/10.1002/jgrd.50708>
- Flegel SK, Gelhaus J, Möckel M, et al (2009) Multi-layer insulation model for MASTER-2009. *Acta Astronaut* 69:911–922. <https://doi.org/10.1016/j.actaastro.2011.06.015>
- Föhn M, Galli A, Vorburger A, Tulej M, Lasi D, Riedo A, et al (2021) Description of the ion-optical system of a mass spectrometer for Jupiter's ICy moons explorer. In: IEEE Aerospace Conference (50100). Big Sky, MT, USA, pp 1–14. <https://doi.org/10.1109/AERO50100.2021.9438344>
- Foss V (2019) Molecular Ions in Ion Upflows and their Effect on Hot Atomic Oxygen Production. MSc thesis, University of Calgary, Canada <http://hdl.handle.net/1880/109857>
- Friedman JS, Chu X, Brum CGM, Lu X (2013) Observation of a thermospheric descending layer of neutral K over Arecibo. *J Atmos Sol-Terr Phys* 104:253–259. <https://doi.org/10.1016/j.jastp.2013.03.002>
- Fritsche B, Klinkrad H, Kashkovsky A, Grinberg E (2000) Spacecraft disintegration during uncontrolled atmospheric Re-entry. *Acta Astronaut* 47:513–522. [https://doi.org/10.1016/S0094-5765\(00\)00090-4](https://doi.org/10.1016/S0094-5765(00)00090-4)
- Fussen D, Vanhellemont F, Tetard C, et al (2010) A global climatology of the mesospheric sodium layer from GOMOS data during the 2002–2008 period. *Atmos Chem Phys* 10:9225–9236. <https://doi.org/10.5194/acp-10-9225-2010>
- Futaana Y, Barabash S, Holmström M, Bhardwaj A (2006) Low energy neutral atoms imaging of the Moon. *Planet Space Sci* 54(2):132–143. <https://doi.org/10.1016/j.pss.2005.10.010>
- Galvin AB, Kistler LM, Popecki MA, et al (2008) The Plasma and Suprathermal Ion Composition (PLAS-TIC) Investigation on the STEREO Observatories. *Space Sci Rev* 136:437–486. <https://doi.org/10.1007/s11214-007-9296-x>
- Gao B, Mathews JD (2015) High-altitude radar meteors observed at Jicamarca Radio Observatory using a multibaseline interferometric technique. *Mon Not R Astron Soc* 452:4252–4262. <https://doi.org/10.1093/mnras/stv1548>
- Gardner JA, Viereck RA, Murad E, et al (1995) Simultaneous observations of neutral and ionic magnesium in the thermosphere. *Geophys Res Lett* 22:2119–2122. <https://doi.org/10.1029/95GL01769>
- Gardner JA, Murad E, Viereck RA, et al (1998) GLO observations of E- and F-region metal atoms and ions. *Adv Space Res* 21:867–870. [https://doi.org/10.1016/S0273-1177\(97\)00644-3](https://doi.org/10.1016/S0273-1177(97)00644-3)

- Gardner CS, Liu AZ, Marsh DR, Feng W, Plane JMC (2014) Inferring the global cosmic dust influx to the Earth's atmosphere from lidar observations of the vertical flux of mesospheric Na. *J Geophys Res* 119:7870–7879. <https://doi.org/10.1002/2014JA020383>
- Geiss J, Balsiger H, Eberhardt P, et al (1978) Dynamics of magnetospheric ion composition as observed by the GEOS mass spectrometer. *Space Sci Rev* 22:537–566. <https://doi.org/10.1007/BF00223940>
- Geiss J, Gloeckler G, von Steiger R (1995) Origin of the solar wind from composition data. *Space Sci Rev* 72:49–60. <https://doi.org/10.1007/BF00768753>
- Geiss J, Bühler F, Cerutti H, Eberhardt P, Filleux C, Meister J, Signer P (2004) The Apollo SWC experiment: results, conclusions, consequences. *Space Sci Rev* 110:307–335. <https://doi.org/10.1023/B:SPAC.0000023409.54469.40>
- Gerding M, Daly S, Plane JMC (2019) Lidar soundings of the mesospheric nickel layer using Ni(³F) and Ni(³D) transitions. *Geophys Res Lett* 46:408–415. <https://doi.org/10.1029/2018GL080701>
- Gilbert JA, Lepri ST, Landi E, Zurbuchen TH (2012) First measurements of the complete heavy-ion charge state distributions of C, O, and Fe associated with interplanetary coronal mass ejections. *Astrophys J* 751:20. <https://doi.org/10.1088/0004-637x/751/1/20>
- Gloeckler G, Hamilton DC (1987) AMPTE ion composition results. *Phys Scr* 1987:73–84. <https://doi.org/10.1088/0031-8949/1987/T18/009>
- Gloeckler G, Wilken B, Stuedemann W, Ipavich FM, Hovestadt D, et al (1985) First composition measurement of the bulk of the storm-time ring current (1 to 300 keV/e) with AMPTE-CCE. *Geophys Res Lett* 12:325–328. <https://doi.org/10.1029/g1012i005p00325>
- Gloeckler G, Geiss J, Balsiger H, et al (1992) The solar wind ion composition spectrometer. *Astron Astrophys Suppl Ser* 92:267–289.
- Gomez Martín JCG, Bones DL, Carrillo-Sánchez JD, et al (2017) Novel experimental simulations of the atmospheric injection of meteoric metals. *Astrophys J* 836:212. <https://doi.org/10.3847/1538-4357/aa5c8f>
- Gomez RG, Fuselier SA, Mukherjee J, et al (2019) The extra-magnetospheric ion environment as observed by the Magnetospheric Multiscale mission hot plasma composition analyzer (MMS-HPCA). *J Geophys Res* 124:1509–1524. <https://doi.org/10.1029/2018JA025392>
- Gorney DJ, Church SR, Mizera PF (1982) On ion harmonic structure in auroral zone waves: the effect of ion conic damping of auroral hiss. *J Geophys Res* 87:10479–10486. <https://doi.org/10.1029/JA087iA12p10479>
- Grande M, Perry CH, Blake JB, et al (1996) Observations of iron, silicon, and other heavy ions in the geostationary altitude region during late March 1991. *J Geophys Res* 101:24707–24718. <https://doi.org/10.1029/96ja00044>
- Grebowsky JM, Aikin AC (2002) In situ measurements of meteoric ions. In: Murad E, Williams IP (eds) *Meteors in the Earth's atmosphere*. Cambridge University Press, Cambridge, pp 189–214
- Grebowsky JM, Bilitza D (2000) (1978) Sounding Rocket Data Base of E- and D-Region Ion Composition. *Adv Space Res* 25:183–192. [https://doi.org/10.1016/S0273-1177\(99\)00916-3](https://doi.org/10.1016/S0273-1177(99)00916-3)
- Grebowsky JM, Brinton HC (1978) Fe⁺ ions in the high latitude F-region. *Geophys Res Lett* 5:791–794. <https://doi.org/10.1029/g1005i009p00791>
- Grebowsky JM, Benna M, Plane JMC, et al (2017) Unique, non-Earthlike, meteoritic ion behavior in upper atmosphere of Mars. *Geophys Res Lett* 44:3066–3072. <https://doi.org/10.1002/2017GL072635>
- Grevesse N, Sauval AJ (1998) Standard solar composition. *Space Sci Rev* 85:161–174. <https://doi.org/10.1023/A:1005161325181>
- Gritsevich MI (2009) Determination of parameters of meteor bodies based on flight observational data. *Adv Space Res* 44:323–334. <https://doi.org/10.1016/j.asr.2009.03.030>
- Gronoff G, Arras P, Baraka S, et al (2020) Atmospheric escape processes and planetary atmospheric evolution. *J Geophys Res* 125:2019JA027639. <https://doi.org/10.1029/2019JA027639>
- Grünwaldt H, et al (1997) Venus tail ray observation near Earth. *Geophys Res Lett* 24:1163–1166. <https://doi.org/10.1029/97GL01159>
- Haaland S, Daly PW, Vilenius E, et al (2020) Suprathermal Fe in the Earth's plasma environment: cluster RAPID observations. *J Geophys Res* 125:e27596. <https://doi.org/10.1029/2019JA027596>
- Haaland S, Daly PW, Vilenius E (2021) Heavy metal and rock in space: cluster RAPID observations of Fe and Si. *J Geophys Res* 126:e2020JA028852. <https://doi.org/10.1029/2020JA028852>
- Halekas JS, Poppe AR, Delory GT, et al (2012) Lunar pickup ions observed by ARTEMIS: spatial and temporal distribution and constraints on species and source locations. *J Geophys Res* 117:E06006. <https://doi.org/10.1029/2012JE004107>
- Halekas JS, Benna M, Mahaffy PR, et al (2015) Detections of lunar exospheric ions by the LADEE Neutral Mass Spectrometer. *Geophys Res Lett* 42:5162–5169. <https://doi.org/10.1002/2015GL064746>
- Hamilton DC, Gloeckler G, Ipavich FM, et al (1988) Ring current development during the great geomagnetic storm of February 1986. *J Geophys Res* 93:14343–14355. <https://doi.org/10.1029/JA093iA12p14343>

- Hanson WB, Sanatani S (1971) Relationship between Fe⁺ ions and equatorial spread F. *J Geophys Res* 76:7761–7768. <https://doi.org/10.1029/JA076i031p07761>
- Hanson WB, Sterling DL, Woodman RF (1972) Source and identification of heavy ions in the equatorial F layer. *J Geophys Res* 77:5530–5541. <https://doi.org/10.1029/JA077i028p05530>
- Harrison J, Kaiser A, Vanden JM (2010) Atmospheric oxygen level and the evolution of insect body size. *Proc R Soc B* 277:19371946. <https://doi.org/10.1098/rspb.2010.0001>
- Heber VS, McKeegan KD, Steele RCJ, et al (2021) Elemental abundances of major elements in the solar wind as measured in genesis targets and implications on solar wind fractionation. *Astrophys J* 907:15. <https://doi.org/10.3847/1538-4357/abc94a>
- Hedin J (2011) The global mesospheric sodium layer observed by Odin/OSIRIS in 2004–2009. *J Atmos Solar-Terr Phys* 73:2221–2227. <https://doi.org/10.1016/j.jastp.2010.10.008>
- Heredia-Avalos S, Garcia-Molina R (2000) Energy loss of Swift oxygen molecular ions traversing amorphous carbon foils. *Phys Lett A* 275:73–79. [https://doi.org/10.1016/S0375-9601\(00\)00506-5](https://doi.org/10.1016/S0375-9601(00)00506-5)
- Hervig ME, Plane JMC, Siskind DE, Feng WH, Bardeen CG, Bailey SM (2021) New global meteoric smoke observations from SOFIE: insight regarding chemical composition, meteoric influx, and hemispheric asymmetry. *J Geophys Res, Atmos* 126:e2021JD035007. <https://doi.org/10.1029/2021jd035007>
- Hilchenbach M (2004) Remote sensing of the lunar or asteroid surfaces via pick-up ions in the solar wind downward direction. *ESA SP-543:55–58*
- Hilchenbach M, Hovstad D, Klecker B, Möbius E (1993) Observation of energetic lunar pick-up ions near Earth. *Adv Space Res* 13:321–324. [https://doi.org/10.1016/0273-1177\(93\)90086-Q](https://doi.org/10.1016/0273-1177(93)90086-Q)
- Hill S (1976) Influence of atmospheric oxygen concentration on acetylene reduction and efficiency of nitrogen fixation in intact *Klebsiella pneumoniae*. *Microbiology* 93:335–345. <https://doi.org/10.1099/00221287-93-2-335>
- Hirahara M, Horwitz JL, Moore TE, et al (1998) Relationship of topside ionospheric ion outflows to auroral forms and precipitation, plasma waves, and convection observed by Polar. *J Geophys Res* 103:17391–17410. <https://doi.org/10.1029/97JA02668>
- Hoffman JH, Dodson WH, Lippincott CR, Hammack HD (1974) Initial ion composition results from the Isis 2 satellite. *J Geophys Res* 79:4246–4251. <https://doi.org/10.1029/JA079i028p04246>
- Höfner J, Friedman JS (2004) The mesospheric metal layer topside: a possible connection to meteoroids. *Atmos Chem Phys* 4:801–808. <https://doi.org/10.5194/acp-4-801-2004>
- Höfner J, Friedman JS (2005) The mesospheric metal layer topside: Examples of simultaneous metal observations. *J Atmos Solar-Terr Phys* 67:1226–1237. <https://doi.org/10.1016/j.jastp.2005.06.010>
- Hovstad D, Hilchenbach M, Bürgi A, et al (1995) CELIAS - charge, element and isotope analysis system for SOHO. *Sol Phys* 162:41–481. <https://doi.org/10.1007/BF00733436>
- Huba JD, Krall J, Drob D (2019) Global ionospheric metal ion transport with SAMI3. *Geophys Res Lett* 46:7937–7944. <https://doi.org/10.1029/2019GL083583>
- Hulfeld L, Kuchlin S, Jenny P (2021) Three dimensional atmospheric entry simulation of a high altitude cometary dustball meteoroid. *A&A* 650:A101. <https://doi.org/10.1051/0004-6361/202140305>
- Hultqvist B (2002) Downward ion acceleration at auroral latitudes: cause of parallel electric field. *Ann Geophys* 20:1117–1136. <https://doi.org/10.5194/angeo-20-1117-2002>
- Hundhausen AJ, Asbridge JR, Bame SJ, et al (1967) Vela 3 satellite observations of solar wind ions: a preliminary report. *J Geophys Res* 72:87–100. <https://doi.org/10.1029/JZ072i001p00087>
- Hunten DM (1967) Spectroscopic studies of the twilight airglow. *Space Sci Rev* 6:493–573. <https://doi.org/10.1016/j.jastp.2005.06.010>
- James AD, Brooke JSA, Mangan TP, et al (2018) Nucleation of nitric acid hydrates in polar stratospheric clouds by meteoric material. *Atmos Chem Phys* 18:4519–4531. <https://doi.org/10.5194/acp-18-4519-2018>
- Janches D, Swarnalingam N, Carrillo-Sánchez JD, et al (2017) Radar detectability studies of slow and small zodiacal dust cloud particles. III, the role of sodium and the head echo size on the probability of detection. *Astrophys J* 843:1. <https://doi.org/10.3847/1538-4357/aa775c>
- Jenniskens P, Albers J, Koop MW, et al (2016) Airborne observations of an asteroid entry for high fidelity modeling. AIAA 2016-0999, 54th AIAA Aerospace Sciences Meeting. <https://doi.org/10.2514/6.2016-0999>
- Johnson B, Goldblatt C (2015) The nitrogen budget of Earth. *Earth-Sci Rev* 148:150–173. <https://doi.org/10.1016/j.earscirev.2015.05.006>
- Jones AV (1974) Optical emissions from aurora. In: *Aurora. Geophysics and astrophysics monographs*, vol 9. Reidel, Dordrecht. https://doi.org/10.1007/978-94-010-2099-2_4
- Jurewicz AJG, Burnett DS, Woolum DS, et al (2007) SIMS results for solar-wind elemental abundances from genesis collectors. *Meteorit Planet Sci Suppl* 42:5299. <https://authors.library.caltech.edu/records/m95da-2zx17>

- Kameda S, Ikezawa S, Sato M, et al (2017) Ecliptic North-south symmetry of hydrogen geocorona. *Geophys Res Lett* 44:11706–11712. <https://doi.org/10.1002/2017GL075915>
- Kastinen D, Kero J (2022) High-altitude meteors detected by the interferometric MU radar. *Mon Not R Astron Soc* 517:3024–3033. <https://doi.org/10.1093/mnras/stac2791>
- Kastinen D, Vierinen J, Grydeland T, Kero J (2023) Using radar beam-parks to characterize the Kosmos-1408 fragmentation event. *Acta Astronaut* 202:341–359. <https://doi.org/10.1016/j.actaastro.2022.10.021>
- Keika K, Takahashi K, Aleksandir Y, et al (2013). Global characteristics of electromagnetic ion cyclotron waves: Occurrence rate and its storm dependence. *J Geophys Res* 118:4135–4150. <https://doi.org/10.1002/jgra.50385>
- Keller JW, Chornay DJ, Hunsaker FH, Ogilvie KW (1999) Gated time-of-flight plasma composition analyzer for space physics research. *Rev Sci Instrum* 70:3167–3172. <https://doi.org/10.1063/1.1149881>
- Kero J, Fujiwara Y, Abo M, et al (2012) MU radar head echo observations of the 2011 October Draconids: MU observations of the 2011 October Draconids. *Mon Not R Astron Soc* 424:1799–1806. <https://doi.org/10.1111/j.1365-2966.2012.21255.x>
- Kero J, Campbell-Brown MD, Stuber G, et al (2019) Radar observation of meteors. In: Ryabova GO, Asher DJ, Campbell-Brown MD (eds) *Meteoroids: sources of meteors on Earth and beyond*. Cambridge University Press, Cambridge, pp 65–89. <https://doi.org/10.1017/9781108606462.008>
- Kessler DJ, Cour-Palais BG (1978) Collision frequency of artificial satellites: the creation of a debris belt. *J Geophys Res* 83(A6):2637–2646. <https://doi.org/10.1029/JA083iA06p02637>
- Kistler LM, Galvin AB, Popecki MA, Simunac KDC, et al (2010b) Escape of O⁺ through the distant tail plasma sheet. *Geophys Res Lett* 37:L21101. <https://doi.org/10.1029/2010GL045075>
- Kistler LM, Mouikis CG, Klecker B, Dandouras I (2010a) Cusp as a source for oxygen in the plasma sheet during geomagnetic storms. *J Geophys Res* 115:A03209. <https://doi.org/10.1029/2009JA014838>
- Kistler LM, Mouikis CG, Genestreti KJ (2013) In-flight calibration of the Cluster/CODIF sensor. *Geosci Instrum Method Data Syst* 2:225–235. <https://doi.org/10.5194/gi-2-225-2013>
- Klecker B, Möbius E, Hovestadt D, et al (1986) Discovery of energetic molecular ions (NO⁺ and O₂⁺) in the storm time ring current. *Geophys Res Lett* 13:632–635. <https://doi.org/10.1029/GL013i007p00632>
- Klinkrad H (2005) Re-entry prediction and on-ground risk assessment. In: *Proceeding of 6th US/Russian space surveillance workshop*
- Kopp E (1997) On the abundance of metal ions in the lower ionosphere. *J Geophys Res* 102:9667–9674. <https://doi.org/10.1029/97JA00384>
- Koppenwallner G, Fritsche B, Lips T, Klinkrad H (2005) SCARAB - a multi-disciplinary code for destruction analysis of space-craft during re-entry. In: *Proceedings of the fifth European symposium on aerothermodynamics for space vehicles, ESA-SP, vol 563, pp 8–11*
- Koten P, et al (2006) The beginning heights and light curves of high-altitude meteors. *Meteorit Planet Sci* 41:1305–1320. <https://doi.org/10.1111/j.1945-5100.2006.tb00523.x>
- Krauss S, Fichtinger B, Lammer H, et al (2012) Solar flares as proxy for the young Sun: satellite observed thermosphere response to an X17.2 flare of Earth's upper atmosphere. *Ann Geophys* 30:1129–1141. <https://doi.org/10.5194/angeo-30-1129-2012>
- Kronberg EA, Bucik R, Haaland S, et al (2011) On the origin of the energetic ion events measured upstream of the Earth's bow shock by STEREO, cluster, and geotail. *J Geophys Res* 116:A02210. <https://doi.org/10.1029/2010JA015561>
- Krüger H, Strub P, Srama R, et al (2019) Modelling DESTINY+ interplanetary and interstellar dust measurements en route to the active asteroid (3200) Phaethon. *Planet Space Sci* 172:22–42. <https://doi.org/10.1016/j.pss.2019.04.005>
- Ku S-B, Edwards GE, Tanner CB (1977) Effects of light, carbon dioxide, and temperature on photosynthesis, oxygen inhibition of photosynthesis, and transpiration in solanum tuberosum. *Plant Physiol* 59:868–872. <https://doi.org/10.1104/pp.59.5.868>
- Lammer H, Kasting JF, Chassefière E, et al (2008) Atmospheric escape and evolution of terrestrial planets and satellites. *Space Sci Rev* 139:399–436. <https://doi.org/10.1007/s11214-008-9413-5>
- Lammer H, Sproß L, Grenfell JL, et al (2019) The role of N₂ as a geo-biosignature for the detection and characterization of Earth-like habitats. *Astrobiology* 19:927–950. <https://doi.org/10.1089/ast.2018.1914>
- Langowski MP, von Savigny C, Burrows JP, et al (2015) Global investigation of the Mg atom and ion layers using SCIAMACHY/Envisat observations between 70 and 150 km altitude and WACCM-Mg model results. *Atmos Chem Phys* 15:273–295. <https://doi.org/10.5194/acp-15-273-2015>
- Lawrence A, Rawls ML, Jah M, et al (2022) The case for space environmentalism. *Nat Astron* 6:428–435. <https://doi.org/10.1038/s41550-022-01655-6>
- Leblanc F, Schmidt C, Mangano V, et al (2022) Comparative Na and K Mercury and moon exospheres. *Space Sci Rev* 218:2. <https://doi.org/10.1007/s11214-022-00871-w>
- Lee JH, Kim KH, Baek SM, et al (2024) The relationship between the energization of moon-originating ions and terrain type on the lunar surface. *J Geophys Res* 129:e2023JA032076. <https://doi.org/10.1029/2023JA032076>

- Lennartsson OW, Collin HL, Ghielmetti AG, Peterson WK (2000) A statistical comparison of the outflow of N_2^+ , NO^+ and O_2^+ molecular ions with that of atomic O^+ ions using Polar/TIMAS observations. *J Atmos Sol-Terr Phys* 62(6):477–483. [https://doi.org/10.1016/S1364-6826\(00\)00019-5](https://doi.org/10.1016/S1364-6826(00)00019-5)
- Lin M-Y, Ilie R (2022) A review of observations of molecular ions in the Earth's magnetosphere-ionosphere system. *Front Astron Space Sci* 8:745357. <https://doi.org/10.3389/fspas.2021.745357>
- Liou J-C, Hall DT, Krisko PH, Opiela JN (2004) LEGEND - a three-dimensional LEO-to-GEO debris evolutionary model. *Adv Space Res* 34:981–986. <https://doi.org/10.1016/j.asr.2003.02.027>
- Lips T, Wartemann V, Koppenwallner G, Klinkrad H, et al (2005) Comparison of ORSAT and SCARAB reentry survival results. In: Proceedings of 4th European conference on space debris, vol 587, p 533
- Liu AZ, Guo YG, Vargas F, Swenson GR (2016). First measurement of horizontal wind and temperature in the lower thermosphere (105–140 km) with a Na Lidar at Andes Lidar Observatory. *Geophys Res Lett* 43:2374–2380. <https://doi.org/10.1002/2016GL068461>
- Lodders K, Palme H, Gail H-P (2009) Abundances of the elements in the Solar System. Landolt-Börnstein, group VI astronomy and astrophysics 4B (Solar System). Springer, Berlin. materials.springer.com/lb/docs/sm_lbs_978-3-540-88055-4_34
- Loesche WJ (1969) Oxygen sensitivity of various anaerobic bacteria. *Appl Microbiol* 18:723–727. <https://doi.org/10.1128/am.18.5.723-727.1969>
- Loranc M, Hanson WB, Heelis RA, St-Maurice J-P (1991) A morphological study of vertical ionospheric flows in the high-latitude region. *J Geophys Res* 96:3627–3646. <https://doi.org/10.1029/90JA02242>
- Lundin R, Guglielmi A (2006) Ponderomotive forces in cosmos. *Space Sci Rev* 127:1–116. <https://doi.org/10.1007/s11214-006-8314-8>
- Mabie J, Bullett T, Moore P, Vieira G (2016) Identification of rocket-induced acoustic waves in the ionosphere. *Geophys Res Lett* 43:11024–11029. <https://doi.org/10.1002/2016GL070820>
- Mahaffy PR, Hodges RR, Benna M, et al (2015) The Neutral Mass Spectrometer on the lunar atmosphere and Dust Environment Explorer Mission. In: edited by ER, Russell C (eds) The lunar atmosphere and Dust Environment Explorer Mission (LADEE). Springer, Cham. https://doi.org/10.1007/978-3-319-18717-4_3
- Mall U, Kirsch E, Cierpka K, et al (1998) Direct observation of lunar pick-up ions near the Moon. *Geophys Res Lett* 25(20):3799–3802. <https://doi.org/10.1029/1998GL900003>
- Mitchell DG, Roelof EC, Bame SJ (1983) Solar wind iron abundance variations at speeds 600 km s⁻¹, 1972–1976. *J Geophys Res* 88:9059–9068. <https://doi.org/10.1029/JA088iA11p09059>
- Moore TE, Chappell CR, Chandler MO, et al (1995) The thermal ion dynamics experiment and plasma source instrument. *Space Sci Rev* 71:409–458. <https://doi.org/10.1007/BF00751337>
- Moore TE, Lundin R, Alcayde D, et al (1999a) Source processes in the high-latitude ionosphere. *Space Sci Rev* 88:7–84. <https://doi.org/10.1023/A:1005299616446>
- Moore TE, Peterson WK, Russell CT, et al (1999b) Ionospheric mass ejection in response to a CME. *Geophys Res Lett* 26:2339–2342. <https://doi.org/10.1029/1999GL900456>
- Murad E, Williams IP (eds) (2002) *Meteors in the Earth's atmosphere: meteoroids and cosmic dust and their interactions with the Earth's upper atmosphere*. Cambridge University Press, Cambridge
- Murphy DM, Abou-Ghanem M, Cziczo DJ, et al (2023) Metals from spacecraft reentry in stratospheric aerosol particles. *Proc Natl Acad Sci USA* 120:e2313374120. <https://doi.org/10.1073/pnas.2313374120>
- Nahar SN, Bautista MA, Pradhan AK (1997) Electron-ion recombination of neutral iron. *Astrophys J* 479:497–503. <https://doi.org/10.1086/303874>
- Nicolaou G, Yamauchi M, Nilsson H, Wieser M, Fedorov A (2017) Simulations as a tool for higher mass resolution spectrometer: lessons from existing observations. *Geophys Res Abstr* 19:EGU2017–EGU16565. presented at EGU General Assembly, Vienna, April 2017
- Nilsson H, Waara M, Arvelius S, et al (2006) Characteristics of high altitude oxygen ion energization and outflow as observed by Cluster: a statistical study. *Ann Geophys* 24:1099–1112. <https://doi.org/10.5194/angeo-24-1099-2006>
- Nilsson H, Waara M, Marghito O, et al (2008) An assessment of the role of the centrifugal acceleration mechanism in high altitude polar cap oxygen ion outflow. *Ann Geophys* 26:145–157. <https://doi.org/10.5194/angeo-26-145-2008>
- Noble ST (1990) A large-amplitude traveling ionospheric disturbance excited by the space shuttle during launch. *J Geophys Res* 95:19037–19044. <https://doi.org/10.1029/JA095iA11p19037>
- Nozawa S, Kawahara TD, Saito N, et al (2014) Variations of the neutral temperature and sodium density between 80 and 107 km above Tromsø during the winter of 2010–2011 by a new solid state sodium LIDAR. *J Geophys Res* 119:441–451. <https://doi.org/10.1002/2013JA019520>
- Ogawa Y, Seki K, Keika K, Ebihara Y (2019) Characteristics of CME- and CIR-driven ion upflows in the polar ionosphere. *J Geophys Res* 124:3637–3649. <https://doi.org/10.1029/2018JA025870>
- Park S-H, Laboulais JN, Leyland P, Mischler S (2021) Re-entry survival analysis and ground risk assessment of space debris considering by-products generation. *Acta Astronaut* 179:604–618. <https://doi.org/10.1016/j.actaastro.2020.09.034>

- Perry CH, Grande M, Zurbuchen TH, et al (2000) Use of Fe charge state changes as a tracer for solar wind entry to the magnetosphere. *Geophys Res Lett* 27:2441–2444. <https://doi.org/10.1029/2000GL003780>
- Peterson WK, Andersson L, Callahan BC, et al (2008) Solar-minimum quiet time ion energization and outflow in dynamic boundary related coordinates. *J Geophys Res* 113:A07222. <https://doi.org/10.1029/2008JA013059>
- Plane JMC (1991) The chemistry of meteoric metals in the Earth's upper atmosphere. *Int Rev Phys Chem* 10:55–106. <https://doi.org/10.1080/01442359109353254>
- Plane JMC (2003) Atmospheric chemistry of meteoric metals. *Chem Rev* 103:4963–4984. <https://doi.org/10.1021/cr0205309>
- Plane JMC (2012) Cosmic dust in the Earth's atmosphere. *Chem Soc Rev* 41:6507–6518. <https://doi.org/10.1039/c2cs35132c>
- Plane JMC, Feng W, Dawkins ECM (2015a) The mesosphere and metals: chemistry and changes. *Chem Rev* 115:4497–4541. <https://doi.org/10.1021/cr500501m>
- Plane JMC, Flynn GJ, Määttäinen A, Moores JE, Poppe AR, Carrillo-Sanchez JD, Listowski C (2018b) Impacts of cosmic dust on planetary atmospheres and surfaces. *Space Sci Rev* 214:23. <https://doi.org/10.1007/s11214-017-0458-1>
- Plane JMC, Daly SM, Feng W, Gerding M, Gomez Martin JC (2021) Meteor-ablated aluminum in the mesosphere-lower thermosphere. *J Geophys Res* 126:e2020JA028792. <https://doi.org/10.1029/2020JA028792>
- Popova OP, Strelkov AS, Sidneva SN (2007) Sputtering of fast meteoroids' surface. *Adv Space Res* 30:567–573. <https://doi.org/10.1016/j.asr.2006.05.008>
- Poppe AR, Samad R, Halekas JS, et al (2012) ARTEMIS observations of lunar pick-up ions in the terrestrial magnetotail lobes. *Geophys Res Lett* 39:L17104. <https://doi.org/10.1029/2012GL052909>
- Poppe AR, Fillingim MO, Halekas JS, Raeder J, Angelopoulos V (2016a) ARTEMIS observations of terrestrial ionospheric molecular ion outflow at the Moon. *Geophys Res Lett* 43:6749–6758. <https://doi.org/10.1002/2016GL069715>
- Poppe AR, Halekas JS, Szalay JR, Horányi M, Levin Z, Kempf S (2016b) LADEE/LDEX observations of lunar pickup ion distribution and variability. *Geophys Res Lett* 43:3069–3077. <https://doi.org/10.1002/2016GL068393>
- Quinn JM, McIlwain CE (1979) Bouncing ion clusters in the Earth's magnetosphere. *J Geophys Res* 82:7365–7370. <https://doi.org/10.1029/JA084iA12p07365>
- Rafano Carná SF, Bevilacqua R (2019) High fidelity model for the atmospheric re-entry of CubeSats equipped with the Drag De-Orbit Device. *Acta Astronaut* 156:134–156. <https://doi.org/10.1016/j.actaastro.2018.05.049>
- Raizada S, Smith JA, Lautenbach J, Aponte N, Perillat P, Sulzer M, Mathews JD (2020) New lidar observations of Ca+ in the mesosphere and lower thermosphere over Arecibo. *Geophys Res Lett* 47:e2020GL087113. <https://doi.org/10.1029/2020GL087113>
- Reames DV (1995) Coronal abundances determined from energetic particles. *Adv Space Res* 15:41–51. [https://doi.org/10.1016/0273-1177\(94\)00018-V](https://doi.org/10.1016/0273-1177(94)00018-V)
- Reisenfeld DB, Burnett DS, Becker RH, et al (2007) Elemental abundances of the bulk solar wind: analyses from genesis and ACE. *Space Sci Rev* 130:79–86. <https://doi.org/10.1007/s11214-007-9215-1>
- Rème H, Aoustin C, Bosqued JM, et al (2001) First multispacecraft ion measurements in and near the Earth's magnetosphere with the identical Cluster ion spectrometry (CIS) experiment. *Ann Geophys* 19:1303. <https://doi.org/10.5194/angeo-19-1303-2001>
- Reynolds R, Jost J, Rubin G, Vila J (2001) Radar measurements of the reentry of the ariane 504 EPC. *Adv Space Res* 28:1269–1275. [https://doi.org/10.1016/S0273-1177\(01\)00396-9](https://doi.org/10.1016/S0273-1177(01)00396-9)
- Richards PG, Torr DG, Reinisch BW, et al (1994) F2 peak electron density at Millstone Hill and Hobart: comparison of theory and measurement at solar maximum. *J Geophys Res* 99:15005–15016. <https://doi.org/10.1029/94JA00863>
- Rojas J, Duprat J, Engrand C, et al (2021) The micrometeorite flux at Dome C (Antarctica), monitoring the accretion of extraterrestrial dust on Earth. *Earth Planet Sci Lett* 560:116794. <https://doi.org/10.1016/j.epsl.2021.116794>
- Ryabova GO, Asher DJ, Campbell-Brown MD (2019) *Meteoroids: sources of meteors on Earth and beyond*. Cambridge University Press, Cambridge
- Saito Y, Yokota S, Asamura K, et al (2010) In-flight performance and initial results of Plasma Energy Angle and Composition Experiment (PACE) on SELENE (Kaguya). *Space Sci Rev* 154:265–303. <https://doi.org/10.1007/s11214-010-9647-x>
- Sarantos M, Hartle RE, Killen RM, et al (2012) Flux estimates of ions from the lunar exosphere. *Geophys Res Lett* 39:L13101. <https://doi.org/10.1029/2012GL052001>
- Sarris, et al (2020) Earth Explorer 10 candidate mission Daedalus: report for assessment. https://esamultimedia.esa.int/docs/EarthObservation/EE10_Daedalus_Report-for-Assessment-v1.0_13Nov2020.pdf















- Schillings A, Nilsson H, Slapak R, et al (2017) Relative outflow enhancements during major geomagnetic storms - Cluster observations. *Ann Geophys* 35:1341–1352. <https://doi.org/10.5194/angeo-35-1341-2017>
- Schulz L, Glassmeier K-H (2021) On the anthropogenic and natural injection of matter into Earth's atmosphere. *Adv Space Res* 67:1002–1025. <https://doi.org/10.1016/j.asr.2020.10.036>
- Schunk R, Nagy A (2009) *Ionospheres*. Cambridge University Press, Cambridge
- Seki K, Hirahara M, Terasawa T, et al (1998) Statistical properties and possible supply mechanisms of tailward cold O⁺ beams in the lobe/mantle regions. *J Geophys Res* 103:4477–4489. <https://doi.org/10.1029/97JA02137>
- Seki K, Keika K, Kasahara S, et al (2019) Statistical properties of molecular ions in the ring current observed by the Arase (ERG) satellite. *Geophys Res Lett* 46:8643–8651. <https://doi.org/10.1029/2019GL084163>
- Servaites JC (1977) pH dependence of photosynthesis and photorespiration in soybean leaf cells. *Plant Physiol* 60:693–696. <https://doi.org/10.1104/pp.60.5.693>
- Shelley EG, Johnson RG, Sharp RD (1972) Satellite observations of energetic heavy ions during a geomagnetic storm. *J Geophys Res* 77:6104–6110. <https://doi.org/10.1029/JA077i031p06104>
- Shelley EG, Simpson DA, Sanders TC (1981) The energetic ion composition spectrometer (EICS) for the dynamics explorer-A. *Space Sci Instrum* 5:443–454.
- Shelley EG, Ghielmetti AG, Balsiger H, et al (1995) The Toroidal Imaging Mass-Angle Spectrograph (TIMAS) for the polar mission. *Space Sci Rev* 71:497–530. <https://doi.org/10.1007/BF00751339>
- Shinagawa H, Oyama S (2006) A two-dimensional simulation of thermospheric vertical winds in the vicinity of an auroral arc. *Earth Planets Space* 58:1173–1181. <https://doi.org/10.1186/BF03352007>
- Slapak R, Hamrin M, Pitkänen T, et al (2017b) Quantification of the total ion transport in the near-Earth plasma sheet. *Ann Geophys* 35:869–877. <https://doi.org/10.5194/angeo-35-869-2017>
- Slapak R, Schillings A, Nilsson H, et al (2017a) Atmospheric loss from the dayside open polar region and its dependence on geomagnetic activity: implications for atmospheric escape on evolutionary timescales. *Ann Geophys* 35:721–731. <https://doi.org/10.5194/angeo-35-721-2017>
- Stasiewicz K, Markidis S, Eliasson B, et al (2013) Acceleration of solar wind ions to 1 MeV by electromagnetic structures upstream of the Earth's bow shock. *Europhys Lett* 102:49001. <https://doi.org/10.1209/0295-5075/102/49001>
- Stern SA (1999) The lunar atmosphere: history, status, current problems, and context. *Rev Geophys* 37(4):453–491. <https://doi.org/10.1029/1999RG900005>
- Stüeken EE, Som SM, Claire M, et al (2020) Mission to Planet Earth: the First Two Billion Years. *Space Sci Rev* 216:31. <https://doi.org/10.1007/s11214-020-00652-3>
- Sydorenko D, Rankin R, Yau AW (2016) Enhanced N² and O² densities inferred from EISCAT observations of Pc5 waves and associated electron precipitation. *J Geophys Res Space Phys* 121:549–566. <https://doi.org/10.1002/2015JA021508>
- Takada M, Seki K, Ogawa Y, et al (2021) Low-altitude ion upflow observed by EISCAT and its effects on supply of molecular ions in the ring current detected by Arase (ERG). *J Geophys Res* 126:e2020JA028951. <https://doi.org/10.1029/2020JA028951>
- Tanaka T, Saito Y, Yokota S, et al (2009) First in situ observation of the Moon-originating ions in the Earth's Magnetosphere by MAP-PACE on SELENE (KAGUYA). *Geophys Res Lett* 36:L22106. <https://doi.org/10.1029/2009GL040682>
- Terada K, Yokota S, Saito Y, et al (2017) Biogenic oxygen from Earth transported to the Moon by a wind of magnetospheric ions. *Nat Astron* 1:0026. <https://doi.org/10.1038/s41550-016-0026>
- Thomas E, Simolka J, DeLuca M, Horanyi M, Janches D, Marshall RA, Munsat T, Plane JMC, Sternovsky Z (2017) Experimental setup for the laboratory investigation of micrometeoroid ablation using a dust accelerator. *Rev Sci Instrum* 88:034501. <https://doi.org/10.1063/1.4977832>
- Vierinen J, Fentzke J, Miller E (2014) An explanation for observations of apparently high-altitude meteors. *Mon Not R Astron Soc* 438:2406–2412. <https://doi.org/10.1093/mnras/stt2358>
- von Steiger R (1995) Solar wind composition and charge states. In: Winterhalter D, Gosling JT, Habbal SR, Kurth WS, Neugebauer M (eds) *Solar wind eight*, Dana Point, CA, USA. AIP, New York, pp 193–198
- von Steiger R, Zurbuchen TH (2002) Kinetic properties of heavy solar wind ions from Ulysses-SWICS. *Adv Space Res* 30:73–78. [https://doi.org/10.1016/S0273-1177\(02\)00174-6](https://doi.org/10.1016/S0273-1177(02)00174-6)
- von Steiger R, Geiss J, Gloeckler G (1997) Composition of the solar wind. In: *Cosmic winds and the heliosphere*, p 581
- von Steiger R, Schwadron NA, Fisk LA, et al (2000) Composition of quasi-stationary solar wind flows from Ulysses/Solar wind ion composition spectrometer. *J Geophys Res* 105:27217–27238. <https://doi.org/10.1029/1999JA000358>
- von Steiger R, Zurbuchen TH, McComas DJ (2010) Oxygen flux in the solar wind: Ulysses observations. *Geophys Res Lett* 37:L22101. <https://doi.org/10.1029/2010GL045389>

- Vondrak T, Plane JMC, Broadley SL, Janches D (2008) A chemical model of meteoric ablation. *Atmos Chem Phys* 8:7015–7031. <https://doi.org/10.5194/acp-8-7015-2008>
- Vorburger A, Wurz P, Barabash S, et al (2014) First direct observation of sputtered lunar oxygen. *J Geophys Res* 119(2):709–722. <https://doi.org/10.1002/2013JA019207>
- Wahlund J-E, Opgenoorth HJ, Häggström I, et al (1992) EISCAT observations of topside ionospheric ion outflows during auroral activity: revisited. *J Geophys Res* 97(A3):3019–3037. <https://doi.org/10.1029/91JA02438>
- Whalen BA, Burrows JR, Yau AW, et al (1990) The suprathermal ion mass spectrometer (SMS) onboard the Akebono (EXOS-D) satellite. *J Geomagn Geoelectr* 42:511–536. <https://doi.org/10.5636/jgg.42.511>
- Whalen BA, Watanabe S, Yau AW (1991) Observations in the transverse ion energization region. *Geophys Res Lett* 18:725–728. <https://doi.org/10.1029/90GL02788>
- Wiegert P, Vaubaillon J, Campbell-Brown M (2009) A dynamical model of the sporadic meteoroid complex. *Icarus* 201:295–310. <https://doi.org/10.1016/j.icarus.2008.12.030>
- Wieser M, Barabash S, Futaana Y, et al (2010) First observation of a mini-magnetosphere above a lunar magnetic anomaly using energetic neutral atoms. *Geophys Res Lett* 37:L05103. <https://doi.org/10.1029/2009GL041721>
- Wieser M, Barabash S, Wang X-D, Grigoriev A, Zhang A, Wang C, Wang W (2020a) The Advanced Small Analyzer for Neutrals (ASAN) on the Chang'E-4 Rover Yutu-2. *Space Sci Rev* 216:73. <https://doi.org/10.1007/s11214-020-00691-w>
- Wieser M, Barabash S, Wang X-D, Zhang A, Wang C, Wang W (2020b) Solar wind interaction with the lunar surface: Observation of energetic neutral atoms on the lunar surface by the Advanced Small Analyzer for Neutrals (ASAN) instrument on the Yutu-2 rover of Chang'E-4, presentation at EGU General Assembly 2020, May 2020. <https://doi.org/10.5194/egusphere-egu2020-9199>
- Wieser M, Williamson H, Stenberg Wieser G, et al (2024) Energy spectra of energetic neutral hydrogen backscattered and sputtered from the lunar regolith by the solar wind. *Astron Astrophys* 684:A146. <https://doi.org/10.1051/0004-6361/202348876>
- Wilken B, Daly PW, Mall U, et al (2001) First results from the RAPID imaging energetic particle spectrometer on board Cluster. *Ann Geophys* 19:1355–1366. <https://doi.org/10.5194/angeo-19-1355-2001>
- Williams DJ, McEntire RW, Schlemm C, et al (1994) Geotail energetic particles and ion composition instrument. *J Geomagn Geoelectr* 46:39–57. <https://doi.org/10.5636/jgg.46.39>
- Wimmer-Schweingruber RF, Crooker NU, Balogh A, et al (2006) Understanding interplanetary coronal mass ejection signatures. *Space Sci Rev* 123:177–216. <https://doi.org/10.1007/s11214-006-9017-x>
- Wittmann P (2022) The Jovian Plasma Dynamics and Composition Analyzer (JDC) for ESA's JUICE mission. PhD thesis, Kiruna: Umeå University and Swedish Institute of Space Physics. <https://urn.kb.se/resolve?urn=urn:nbn:se:umu:diva-193773>
- Wu JF, Feng W, Liu HL, et al (2021) Self-consistent global transport of metallic ions with WACCM-X. *Atmos Chem Phys* 21:15619–15630. <https://doi.org/10.5194/acp-21-15619-2021>
- Wüest M, Evans DS, von Steiger R (2007) Calibration of particle instruments in space physics, ISSI scientific report, SR-007. International Space Science Institute, Bern. <https://www.issibern.ch/PDF-Files/SR-007.pdf>
- Wurz P (2005) Solar wind composition. In: Danesy D, Poedts S, De Groof A, Andries J (eds) *The Dynamic Sun: challenges for theory and observations*, ESA Special Publication, vol SP-600. ESA, Noordwijk
- Wurz P (2012) Erosion processes affecting interplanetary dust grains. In: *Nano dust in the Solar System: discoveries and interpretations*. Astrophysics and Space Science Library, vol 385. Springer, Berlin, pp 161–178. https://doi.org/10.1007/978-3-642-27543-2_8
- Wurz P, Gubler L, Bochsler P, Möbius E (1998) Isochronous mass spectrometry for space plasma applications. In: Pfaff RF, Borovsky JE, Young DT (eds) *Measurement Techniques for Space Plasmas*. American Geophysical Union, Washington, p 229–235. <https://doi.org/10.1029/GM102p0229>
- Wurz P, Wimmer-Schweingruber RF, Issautier K, Bochsler P, Galvin AB, Ipavich FM (2001) Composition of magnetic cloud plasmas during 1997 and 1998. *Am Inst Phys Sol Galact Compos CP-598*:145–151. <https://doi.org/10.1063/1.1618687>
- Wurz P, Bochsler P, Paquette JA, Ipavich FM (2003) Calcium abundance in the solar wind. *Astrophys J* 583:489–495. <https://doi.org/10.1086/344834>
- Wurz P, Rohner U, Whithy JA, Kolb C, Lammer H, Dobnikar P, Martín-Fernández JA (2007) The lunar exosphere: the sputtering contribution. *Icarus* 191:486–496. <https://doi.org/10.1016/j.icarus.2007.04.034>
- Wurz P, Fatemi S, Galli A, et al (2022) Particles and photons as drivers for particle release from the surfaces of the Moon and Mercury. *Space Sci Rev* 218(3):10. <https://doi.org/10.1007/s11214-022-00875-6>
- Xie L, Li L, Zhang A, et al (2021) Inside a lunar mini-magnetosphere: first energetic neutral atom measurements. *Geophys Res Lett* 48:e2021GL093943. <https://doi.org/10.1029/2021GL093943>
- Yamauchi M (2019) Terrestrial ion escape and relevant circulation in space. *Ann Geophys* 37:1197–1222. <https://doi.org/10.5194/angeo-37-1197-2019>

- Yamauchi M, Eliasson L, Lundin R, Norberg O (2005) Unusual heavy ion injection events observed by Freja. *Ann Geophys* 23:535–543. <https://doi.org/10.5194/angeo-23-535-2005>
- Yamauchi M, Johnsen MG, Enell C-F, et al (2020) High-latitude crochet: solar-flare-induced magnetic disturbance independent from low-latitude crochet. *Ann Geophys* 38:1159–1170. <https://doi.org/10.5194/angeo-38-1159-2020>
- Yau AW, André M (1997) Sources of ion outflow in the high latitude ionosphere. *Space Sci Rev* 80:1–25. <https://doi.org/10.1023/A:1004947203046>
- Yau AW, Howarth A (2016) Imaging thermal plasma mass and velocity analyzer. *J Geophys Res* 121:7326–7333. <https://doi.org/10.1002/2016JA022699>
- Yau AW, James HG (2015) CASSIOPE enhanced polar outflow probe (e-POP) mission overview. *Space Sci Rev* 189:3–14. <https://doi.org/10.1007/s11214-015-0135-1>
- Yau AW, Whalen BA (1992) Auroral ion composition during large magnetic storms. *Can J Phys* 70:500–509. <https://doi.org/10.1139/p92-085>
- Yau AW, Whalen BA, McNamara AG, et al (1983) Particle and wave observations of low-altitude ionospheric ion acceleration events. *J Geophys Res* 88:341–355. <https://doi.org/10.1029/JA088iA01p00341>
- Yau AW, Whalen BA, Goodenough C, et al (1993) EXOS D (Akebono) observations of molecular NO⁺ and N₂⁺ upflowing ions in the high-altitude auroral ionosphere. *J Geophys Res* 98:11205–11224. <https://doi.org/10.1029/92JA02019>
- Yau AW, Greffen E, Knudsen DJ, Sagawa E (1998) Radio-frequency ion mass spectrometer measurements of thermal ion composition, velocity, and temperature: the EXOS-D suprathermal mass spectrometer. In: Pfaff RF, Borovsky JE, Young DT (eds) *Measurement Techniques for Space Plasmas*. American Geophysical Union, Washington, p 307–312. <https://doi.org/10.1029/GM102p0307>
- Yau AW, Abe T, André M, Howarth AD, Peterson WK (2021) Ionospheric ion acceleration and transport. In: Maggiolo R, André N, Hasegawa H, Welling DT, Zhang Y, Paxton LJ (eds) *Magnetospheres in the Solar System*. Geophysical Monograph Series, vol 259. AGU and Wiley. <https://doi.org/10.1002/9781119815624.ch14>
- Yokota S, Saito Y (2005) Estimation of picked-up lunar ions for future compositional remote SIMS analyses of the lunar surface. *Earth Planets Space* 57:281–289. <https://doi.org/10.1186/BF03352564>
- Yokota S, Saito Y, Asamura K, et al (2009) First direct detection of ions originating from the Moon by MAP-PACE IMA onboard SELENE (KAGUYA). *Geophys Res Lett* 36:L11201. <https://doi.org/10.1029/2009GL038185>
- Yokota S, Kasahara S, Mitani T, et al (2017) Medium-energy particle experiments-ion mass analyzer (MEP-i) onboard ERG (Arase). *Earth Planets Space* 69:172. <https://doi.org/10.1186/s40623-017-0754-8>
- Yokota S, Terada K, Saito Y, et al (2020) KAGUYA observation of global emissions of indigenous carbon ions from the Moon. *Sci Adv* 6:eaba1050. <https://doi.org/10.1126/sciadv.aba1050>
- Young DT, Geiss J, Balsiger H, et al (1977) Discovery of He²⁺ and O²⁺ ions of terrestrial origin in the outer magnetosphere. *Geophys Res Lett* 4:561–564. <https://doi.org/10.1029/GL004i012p00561>
- Young DT, Burch JL, Gomez RG, et al (2016) Hot plasma composition analyzer for the magnetospheric multiscale mission. *Space Sci Rev*. <https://doi.org/10.1007/s11214-014-0119-6>
- Zhou X-Z, Angelopoulos V, Poppe AR, Halekas JS (2013) ARTEMIS observations of lunar pickup ions: mass constraints on ion species. *J Geophys Res, Planets* 118:1766–1774. <https://doi.org/10.1002/jgre.20125>
- Zurbuchen TH, Fisk LA, Gloeckler G, von Steiger R (2002) The solar wind composition throughout the solar cycle: a continuum of dynamic states. *Geophys Res Lett* 29:1352. <https://doi.org/10.1029/2001GL013946>
- Zurbuchen TH, Weberg M, von Steiger R, et al (2016) Composition of coronal mass ejections. *Astrophys J* 826:10. <https://doi.org/10.3847/0004-637X/826/1/10>

Publisher's Note Springer Nature remains neutral with regard to jurisdictional claims in published maps and institutional affiliations.

Authors and Affiliations

M. Yamauchi¹  · S. Christon²  · I. Dandouras³  · S. Haaland⁴  · D. Kastinen¹  · L.M. Kistler⁵  · I. Mann⁶  · S. Nozawa⁷  · J.M.C. Plane⁸  · Y. Saito⁹  · L. Schulz¹⁰  · S. Watababe¹¹  · P. Wurz¹²  · A.W. Yau¹³ 

✉ M. Yamauchi
M.Yamauchi@irf.se

- 1 Swedish Institute of Space Physics (IRF), Kiruna, Sweden
- 2 Focused Analysis and Research (FAR), Charleston, SC, USA
- 3 Institut de Recherche en Astrophysique et Planétologie (IRAP), Centre national de la recherche scientifique (CNRS)/Université de Toulouse/Centre national d'études spatiales (CNES), Toulouse, France
- 4 The University Centre in Svalbard, Longyearbyen, Norway
- 5 University New Hampshire, Durham, NH, USA
- 6 Department of Physics and Technology, UiT Arctic University of Norway, Tromsø, Norway
- 7 Institute for Space-Earth Environmental Research (ISEE), Nagoya University, Nagoya, Japan
- 8 School of Chemistry, University of Leeds, Leeds, UK
- 9 Institute of Space and Astronautical Science (ISAS), Japan Aerospace Exploration Agency (JAXA), Sagamihara, Japan
- 10 Institute of Geophysics and Extraterrestrial Physics, Technische Universität Braunschweig, Braunschweig, Germany
- 11 Hokkaido Information University, Ebetsu, Japan
- 12 Physics Institute, University of Bern, Bern, Switzerland
- 13 Department of Physics and Astronomy, University of Calgary, Calgary, Alberta, Canada